ADSORPTION STUDIES OF POLYSACCHARIDES AND PHOSPHOLIPIDS ONTO CELLULOSE

Xiaosong Du

Dissertation submitted to the faculty of the Virginia Polytechnic Institute and State University in partial fulfillment of the requirements for the degree of

Doctor of Philosophy

in

Chemistry

Alan R. Esker, Chair
Hervé Marand
John R. Morris
Louis A. Madsen

December 12, 2011
Blacksburg, VA

Keywords: Polysaccharide, Cellulose Film, Phospholipid Vesicles, Atomic Force Microscopy, Surface Plasmon Resonance Spectroscopy, Quartz Crystal Microbalance with Dissipation Monitoring

ADSORPTION STUDIES OF POLYSACCHARIDES AND PHOSPHOLIPIDS ONTO CELLULOSE

Xiaosong Du

ABSTRACT

Interactions between biomolecules and cellulose films at solid/liquid interfaces was studied by surface plasmon resonance spectroscopy (SPR), quartz crystal microbalance with dissipation monitoring (QCM-D) and *in situ* atomic force microscopy (AFM) measurements. This dissertation shows the porous character of nanocrystalline cellulose films as the key feature for enhanced adsorption of chemically modified polysaccharides and provides quantitative analysis of polymer supported phospholipid structures as a stable platform for studying membrane-related processes.

Smooth cellulose I films were prepared by spincoating cellulose nanocrystal suspensions onto positively charged self-assembled monolayers on gold. The adsorption of pullulan cinnamate (PC) onto cellulose surfaces increased with increasing degree of cinnamate substitution. The interactions between PCs with higher degree of substitution (DS) and porous nanocrystalline cellulose (NC) films presumably generated looped multilayer PC structures that adsorbed more than twice as much onto NC films than onto regenerated cellulose (RC) films. PC chains not only covered the NC surface but also penetrated into the porous film. The porous features of NC film are responsible for the greater adsorption of polymer chains relative to tightly packed RC films.

Adsorption of phospholipid vesicles onto RC and NC films was also studied. Aggregates of intact vesicle were observed on NC surfaces with high water content ~ 84 % by mass.

Phospholipid patches with smooth features were found to assemble onto RC surfaces with a lower degree of hydration ~ 30 % by mass. Vesicle membrane breakage was triggered by a destabilizing agent, LysoPC. The great mass decrease, and changes in dissipation and degree of hydration for phospholipid structures after exposure to LysoPC corresponded to the transformation from vesicles to layered structures. Initial binding of LysoPC micelles to unruptured vesicles was clearly resolved in SPR, whereas the huge mass decrease associated with bound water hides the initial adsorption of LysoPC onto vesicles in QCM-D experiments. The intitial binding of LysoPC micelles onto vesicle membranes lasted for 200 seconds with a maximal increase of 14 % by mass prior to vesicle collapse.

The role of cholesterol in phospholipid interactions with model cellulose surfaces was also considered. Supported vesicle layers over RC surfaces were observed for vesicle membranes containing ≥ 6.3 % by mole cholesterol, whereas phospholipid or phospholipid with lower cholesterol content formed disconnected lipid islands on RC surfaces. Meanwhile, intact vesicles were always observed on NC surfaces for phospholipid/cholesterol blends regardless of the cholesterol content. The intact vesicles on cellulose surfaces were attributed to the ability of cholesterol to accommodate vesicle deformation.

These studies showed the impact of mesoscale structure of cellulose films on adsorbates. It sheds light on the role of the lignin-carbonhydrate-complex in plant cell wall structure and will inform the next generation of biomimetic nanocomposites. The designed polymer supported biomimetic membranes provide a perfect platform to develop intact and ruptured protoplast systems for the study of plant cell wall self-assembly.

ACKNOWLEDGEMENTS

I would like to thank Prof. Alan R. Esker for his guidance during the course of my Ph. D study at Virginia Tech. I appreciate his patience in my research work. I would like to thank my committee members, Profs. John R. Morris, Hervé Marand and Louis A. Madsen for their valuable time with respect to my project and career. Special thanks to Professor Richard D. Gandour for helpful conversations and useful suggestions.

I am also grateful to all of my group members, Jae Hyun Sim, Joshua D. Kittle, Yang Liu, Chuanzi Ouyang, Feng Jiang, Xiao Zhang, Chao Wang, Chen Qian, Christopher S. Estes, Ying Ni, David W. Caldwell, Holly Goodman and Heejun Choi. I would also like to thank several former colleagues, Dr. Ufuk Karabiyik, Dr. Aziz Kaya, Dr. Wen Yin and Dr. Zelin Liu for helping and training me in the lab.

I would like to thank my family for their support and love over the years. Special thanks to my wife, Ying Chen. I would like to thank the Department of Chemistry for trusting me to teach general chemistry and physical chemistry lab courses. I am also grateful to the National Science Foundation (CHE-0724126), the National Research Initiative of the USDA Cooperative State Research, Education and Extension Service, grant number 2005-35504-16088 and the Center for LignoCellulose Structure and Formation, an Energy Frontier Research Center funded by the U.S. Department of Energy, Office of Science, Office of Basic Energy Sciences (DE-SC0001090) for financial support.

Table of Contents

List of Figures

Chapter 2

Chapter 3

Chapter 4

Chapter 5

Chapter 6

Chapter 7

List of Tables

Chapter 4

Chapter 5

Chapter 6

CHAPTER 1

Overview

Research interest in plant cell walls varies from the self-assembly of polysaccharides[1,2] to bioconversion of biomass,[3,4] from cellulose synthesis by cellulose synthase complex[5] to strategies for improving adhesion at polymer/cellulose-fiber interfaces in wood-plastic composites.[6,7] Polysaccharides as a source of energy for metabolic processes in biological organisms are also considered for drug delivery, tissue engineering and separation applications.[8] Lignocellulosic materials are also promising composite materials with excellent mechanical properties and bio-compatibility. One aim of this study is to investigate chemically modified polysaccharides, such as pullulan modified with photo-crosslinkable cinnamoyl groups, which can be used to mimic the lignin-carbohydrate complex in cell wall biogenesis.[9,10] The interaction of polysaccharide derivatives with model cellulose surfaces can be studied by surface plasmon resonance spectroscopy (SPR) and *in situ* atomic force microscopy (AFM) measurements. Various factors influencing adsorption including substrate charge, porosity and crystallinity of cellulose films were considered to better understand interactions between cellulose, hemicellulose and lignin, which are the principal biopolymers in plant cell wall structures. Another aim is to study polymer cushioned phospholipid structures,[11,12] the transformation of floppy vesicle layers to phospholipid multilayer structures[13-16] and the role of cholesterol in phospholipid interactions with substrates.[17-21] The combination of SPR and quartz crystal microbalance with dissipation monitoring (QCM-D) allows for the monitoring of adsorption, the calculation of the hydration degree of adsorbed films, and the quantification of biomolecule uptake by vesicle membranes. Through the study of interactions between plant cell wall polymers, these studies may inform future work aimed at the generation of biomimetic nanocomposites and biosensing.

This dissertation consists of seven chapters. Chapter 2 provides an introduction and review related to this study. It begins with an introduction to structures and components of the plant cell wall followed by polysaccharides and their derivatives. Subsequent discussion includes bioconversion of biomass to biofuels and polymer cushioned phospholipid structures at liquid/solid interfaces. Finally, several techniques including self-assembled monolayers, the Langmuir-Blodgett technique, spincoating, SPR, AFM, QCM-D, critical micelle concentration determinations using fluorescence spectroscopy and a pyrene dye, transmission electron microscopy, ellipsometry and reflection absorption infrared spectroscopy (RAIRS) are presented.

Materials, synthesis of pullulan cinnamate and cellulose samples, substrate preparation, and characterization techniques for this study are provided in Chapter 3. Chapter 3 will be the only chapter describing detailed experimental methods used in this study.

Chapter 4 describes pullulan cinnamate (PC) adsorption onto nanocrystalline cellulose (NC) films by SPR and *in situ* AFM. The cellulose I NC films anchored to gold by an amine terminated alkane thiol self-assembled monolayer (SAM-NH_2) were prepared from cellulose nanocrystal suspensions. RAIRS indicated that the uniform NC films showed greater crystallinity than amorphous cellulose films regenerated from trimethylsilyl cellulose (TMSC) by HCl vapor in the gas phase, termed regenerated cellulose (RC). More than twice as much PC adsorbed onto NC films than onto RC films in initial studies. Several possible causes, including surface charge, the underlying self assembled monolayer and crystalline degrees of cellulose films, were considered. It was found that the porous features of the NC films were responsible for the greater adsorption relative to RC films. This conclusion was drawn from studies of PC adsorption onto

NC films of different thickness (d). Measurements of surface excess (Γ), the mass adsorbed per unit area (active sensor area), showed Γ increased linearly with d before crossing over to a plateau. Experiments revealed that the degree of cinnamate group substitution in highly substituted PCs had a tremendous impact on the features such as the cross-over point, slope of the linear portion of the film, and plateau value in the graphs of Γ vs. d for NC films. The fact that extrapolated intercepts of Γ to d = 0 for NC films coincided with values for nonporous RC was interpreted as an adsorbed layer at the top of the film that was similar for NC and amorphous RC. The rest of Γ for PCs with high DS reflected PC penetration (sorption) into the NC films rather than confinement to the surface.

In Chapter 5, the interactions of phospholipid vesicles with RC and NC films were investigated by QCM-D, SPR and *in-situ* AFM experiments. Partial lipid layers of smooth features formed on RC surfaces with the degree of hydration ~ 30% by mass, whereas large aggregates of intact vesicle assembled onto NC surfaces with higher water content ~ 84% by mass. Micelles of LysoPC, a single-tail phospholipid surfactant known to induce cell membrane rupture, were used to promote the transformation of vesicles to layered structures. The large decrease of the adsorbed mass, dissipation change, and degree of hydration for the lipid structures after exposure to LysoPC corresponded to the conversion of floppy vesicle layers into more rigid multilayer structures. Initial binding of LysoPC micelles to unruptured vesicles can be clearly resolved by SPR signals. The uptake of LysoPC by vesicle membranes lasted for 200 seconds with a maximal increase of 14% by mass prior to membrane collapse with subsequent desorption of lipids or coupled water. The formed multilayer phospholipid structures on the NC surfaces had similar degrees of hydration as disconnected lipid islands on RC surfaces.

Chapter 6 describes the role of cholesterol in phospholipid interactions with model cellulose surfaces by QCM-D, SPR and *in-situ* AFM experiments. Pure phospholipid and phospholipid with low cholesterol content formed disconnected lipid islands on RC surfaces which were observed with strong contrast in AFM height and phase images. Supported vesicular layers on RC surfaces were observed for lipid with high cholesterol content (> 6.3 mole%). The failure of the vesicles to rupture was attributed to the ability of cholesterol to relax the stresses of the intact vesicle and accommodate vesicle deformation. Through the combination of SPR and QCM-D measurements, the degree of hydration for phospholipid patches and vesicle layers on RC surfaces were calculated as ~ 30% and ~ 70% by mass, respectively. Compared to RC surfaces, the formation of vesicle layers on silica surfaces needed higher percentages of cholesterol in the vesicle membrane, as high as 55% by mole. In contrast, intact vesicles were always observed for mixed phospholipid/cholesterol vesicles adsorbed onto NC surfaces despite of the increase of cholesterol content. This further confirmed that cholesterol molecules buried within the vesicle membrane only led to stiffness rather than instability. The highly hydrated vesicle layers that adsorbed onto NC surfaces had even higher degrees of hydration ~ 80% by mass.

Finally, Chapter 7 summarizes the overall conclusions of this study and provides suggestions for future work: (1) bacterial cell adsorption onto cellulose surfaces, (2) phospholipid vesicle adsorption onto pullulan cinnamate surfaces with controlled hydrophobicity, (3) preparation of curdlan derivatives and curdlan films on substrates, and (4) polyelectrolyte adsorption onto cellulose surfaces.

References:

((1) Dupuy, A. D.; Engelman, D. M. *Proc. Natl. Acad. Sci. U. S. A.* **2008**, *105*, 2848–2852.

(2) Alberts, B.; Johnson, A.; Lewis, J.; Raff, M.; Roberts, K.; Walter, P. Molecular Biology of the Cell, 4th Ed., Garland Science, New York, 2002.

(3) Nonhebel, S. *Renew. Sustain. Energy Rev.* **2005**, *9*, 191-201.

(4) Tilman, D.; Hill, J.; Lehman, C. *Science* **2006**, *314*, 1598-600.

(5) Yennawar N. H.; Li L.; Dudzinski D. M.; Tabuchi A. ; Cosgrove D. J. *Proc. Natl. Acad. Sci. U. S. A.* **2006**,*103*, 14664-14671.

(6) Mohanty, A. K.; Misra, M.; Drzal, L. T. *Composite Interfaces* **2001**, *8*, 313-343.

(7) Samir, M. A. S. A.; Alloin, F.; Dufresne, A. *Biomacromolecules* **2005**, *6*, 612-626.

(8) Tsai, C. S. *Biomacromolecules: introduction to structure, function, and informatics*; John Wiley & Sons, Inc.: Hoboken, NJ, 2007.

(9) Gradwell, S. E.; Renneckar, S.; Esker, A. R.; Heinze, T.; Gatenholm, P.; Vaca-Garcia, C.; Glasser, W. *C. R. Biol.* **2004**, *327*, 945-953.

(10) Kaya, A.; Du, X.; Liu, Z.; Lu, J. W.; Morris, J. R.; Glasser, W. G.; Heinze, T.; Esker, A. R. *Biomacromolecules* **2009,** *10*, 2451-2459.

(11) Sackmann, E. *Science*, **1996**, *271*, 43-48.

(12) Tanaka, M.; Sackmann, E. *Nature* **2005**, *437*, 656-663.

(13) Cho, N.; Wang, G.; Edvardsson, M.; Gleen, J. S.; Hook, F.; Frank, C. W. *Anal. Chem.* **2009**, *81*, 4752-4761.

(14) Needham, D.; Stoicheva, N.; Zhelev, D. V. *Biophysical Journal* **1997**, *73*, 2615-2629.

(15) Hamai, C.; Yang, T.; Kataoka, S.; Cremer, P. S.; Musser, S. M. *Biophysical Journal* **2006**, *90*, 1241-1248.

(16) Hamai, C.; Cremer, P. S.; Musser, S. M. *Biophysical Journal* **2007**, *92*, 1988-1999.

(17) Chen, M.; Li, M.; Brosseau, C. L.; Lipkowski, J. *Langmuir* **2009**, *25*, 1028-1037.

(18) Lipowski, R.; Sackmann, E., Eds. *Structure and Dynamics of Membranes*; Elsevier, Amsterdam, 1995.

(19) Yeagle, P. L. *Biology of Cholesterol*; CRC Press: Boca Raton, FL, 1988.

(20) Finegold, L. *Cholesterol and Membrane Models*; CRC Press: Boca Raton, FL, 1993.

(21) Lemmich, J.; Mortensen, K.; Ipsen, J. H.; Honger, T.; Bauer, R.; Mouritsen, O. G. *Eur. Biophys. J.* **1997**, *25*, 293.

CHAPTER 2

Introduction and Review

2.1 Introduction to Plant Cell Walls

Plant cell walls provide 60 to 90% of the volume percentage in the wood structure.[1] The thin layers of middle lamella connect adjacent plant cells. The plant cell wall close to the middle lamella consists of a primary wall and a secondary wall.[2] The highly hydrated primary cell walls can grow both longitudinally and radially to withstand the hydrostatic forces during cell wall growth even though the typical thickness of the wall is less than 100 nm. When the expansion of plant cell terminates, the secondary walls which increase the stiffness and strength of the cell wall form to reduce the flexibility of the plant cell. From the middle lamella to the innermost lumen structures, the layers are the primary cell wall, the first layer of the secondary cell wall (the S_1 layer), the central layer (the S_2 layer which is the thickest of the three layers of the secondary cell wall) and the S_3 layer, respectively.

The composition of cell walls includes cellulose, hemicelluloses, lignin, pectin and some proteins.[3,4] For the primary cell walls (Figure 2.1), the cellulose microfibrils are embedded in a matrix of hemicellulose, like xyloglucan, and pectin to form a composite structure.[5] Cellulose networks are also crosslinked by hemicelluloses in the secondary cell wall. It is widely accepted that the aggregation patterns and hierarchy of cellulose microfibrils and hemicelluloses were determined by self-assembly.[6,7] The phenolic polymer, lignin covers or covalently bonds to cellulose microfibrils and hemicelluloses. The presence of hydrophobic lignin leads to dehydration of the secondary cell wall and is responsible for the recalcitrance to enzyme catalyzed hydrolysis.[8-10]

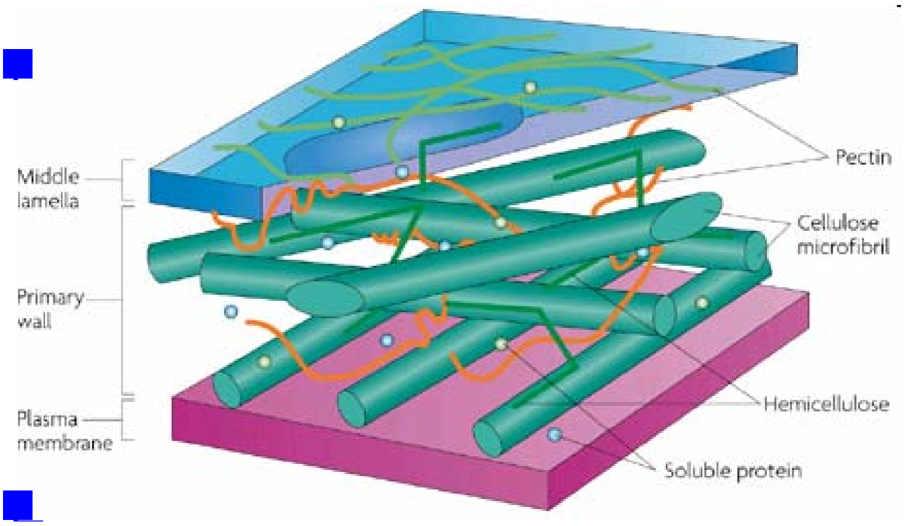

Figure 2.1. The schematic structure of a primary plant cell wall. Reprinted with permission from *Nature Reviews Genetics* **2008**, *9*, 433-443.[5]

2.2 Common Polysaccharides in Nature

Polysaccharides are polymers linked by different monosaccharides through glucosidic bonds. Various conformations such as helices and sheets are observed for polysaccharides in aqueous media.[11] As the main component of plant cell wall, polysaccharides are biodegradable, environmentally friendly materials and renewable resources. It was proposed that cellulosic and lignin-carbohydrate materials can be employed as reinforcing and bonding components at fiber/thermoplastics interfaces.[12,13] Bioconversion of biomass, such as renewable lignocellulose materials to biofuels by cellulolytic enzymes provides alternative energy to decrease our reliance on fossil-based materials.[14] The chemically modified polysaccharides, such as pullulan substituted with cinnamoyl/cinnamyl groups, can be used to mimic the lignin-carbohydrate complex in cell wall biogenesis.[15,16] In this section, several commonly used polysaccharides in nature are described.

2.2.1 Cellulose and Hemicellulose

Cellulose contributes as much as 40% by mass to the cell wall. As shown in Figure 2.2, the linear, unbranched cellulose chain is linked by β-(1-4) glucosidic bonds, whose degree of polymerization (DP) ranges from hundreds to tens of thousands.[17] There are three hydroxyl groups per anhydroglucose unit (AGU) in the cellulose chains.[18] Adjacent AGUs are rotated 180° in the plane of the molecule for thermodynamic preference.[19] Cellulose chains can be laterally linked by hydrogen bonds and van der Waals interactions into aggregates where water is excluded by the hydrophobic portions of the polymer.[20] The association of these aggregates leads to long persistent ribbons or linear strands of closely bound fibers. The flat ribbon of cellulose is also compatible with the helical conformations of hemicellulose which act as structural regulators in the cell wall. Associations between cellulose molecules results in its crystallinity, which has been demonstrated by X-ray diffraction and polarized light optical microscopy.[4] It was shown that crystalline regions are separated by amorphous regions every 600 Å.[2]

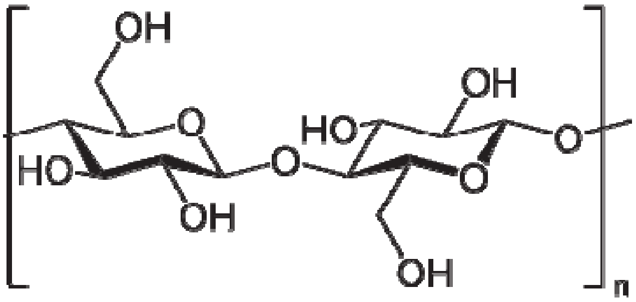

Figure 2.2. The repeating unit of cellulose chains.

In the cell wall, cellulose exists in the form of threadlike structures which are called microfibrils. The cellulose microfibrils play an important role in resistance to tensile forces and as the framework of the plant cell. These microfibrils are arranged in a parallel orientation by hydrogen bonding and are about 10-29 nm in diameter. Cellulose nanocrystals which are 5 nm wide and 100 to 150 nm long can be created by sulfuric acid hydrolysis of softwood pulp. [21,22] The cellulose hydroxyl groups will be substituted by sulfate groups on the surface of the nanocrystals during the hydrolysis process. Those sulfate groups are negatively charged in aqueous suspension at pH > 2.5. To reduce the negative surface charge of nanocrystals, exposing the suspensions to high temperatures reverses the substitution reaction with controlled amounts of sulfuric acid released from the surface of the nanoparticles. The sulfate groups on the surfaces of cellulose nanocrystals can be totally neutralized with pyridine.[23] Anionic cellulose nanocrystals can even be converted into cationic cellulose nanocrystals by reacting an epoxy-activated surface hydroxyl group with ammonium hydroxide.[24]

Cellulose films can be prepared for interfacial studies to supplement bulk studies. Trimethylsilylcellulose (TMSC) can be spin-coated onto silicon wafers, with subsequent exposure to HCl vapor leading to the cleavage of the trimethylsilyl groups.[25,26] However, the regenerated cellulose surfaces are predominantly amorphous. Various crystalline surfaces with different film morphology including cellulose I and II crystal surfaces can be prepared by air-drying or spin-coating of nanocrystalline cellulose suspensions.[21,22] To help stabilize the spin-coated film in aqueous solution, anchoring polymers or charged self-assembled monolayers are widely used.[27] It was shown that heat treatment for short periods of time also improves film stability.

Cellulose microfibrils are coated and crosslinked with hemicelluloses through hydrogen bonds.[28] Even though hemicelluloses are polysaccharides such as cellulose, they are usually branched heteropolysaccharides with different sugar units and a much lower DP (from 80 to 200).

Typical monomers in hemicelluloses are D-glucose, D-mannose, L-arabinose, and D-xylose.[17] Common hemicelluloses in wood are xylans, mannans, β-glucans with mixed linkages, and xyloglucans.[29] The complex structure of hemicellulose makes it difficult to extract the crucial factors such as sugar composition, surface charge, polymer conformation, *etc*. for the formation of cellulose-hemicellulose network. Hence, it is necessary to employ some model polysaccharides, like pullulan, dextran and curdlan to mimic the hemicellulose structure in the plant cell wall.

2.2.2 Pullulan

Pullulan is a biodegradable water-soluble polysaccharide extracellularly produced by the fungus, *Aureobasidium pullulans*. The DP value of the linear pullulan chain is lower than cellulose ranging from 80 to 200. Due to its low polydispersity index ($M_w/M_n \sim 1.4$) and excellent solubility in various solvents, pullulan is frequently used as a model to study the hemicellulose-lignin complex.[30] The repeating unit of pullulan (Figure 2.3) is composed of three glucose molecules which are connected via two α-1,4-linkages and one α-1,6-linkage.[31] The linear structure of pullulan, confirmed by light scattering measurements in aqueous solution, is consistent with a linear coil conformation.[32] The expansion factor is larger than lightly branched dextran leading to a larger radius of gyration. It was proposed that pullulan can be used as a standard sample for studies of hydrophobically modified polysaccharides instead of dextran.[33]

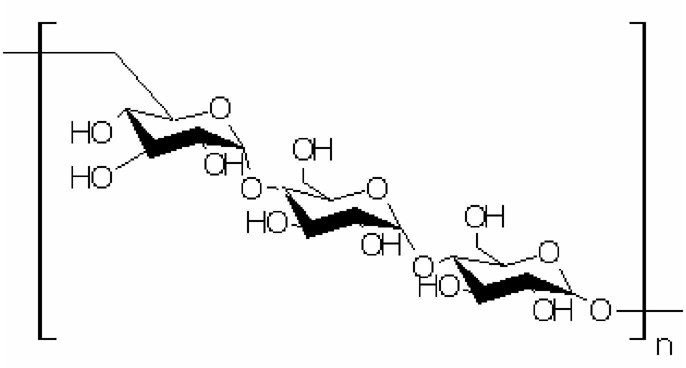

Figure 2.3. The repeating unit of pullulan chains.

Due to greater reactivity and lower steric hindrance than other hydroxyl groups in pullulan, the primary alcohol, which exists on two of the three glucose units has attracted considerable attention for chemical modifications. It was reported that TEMPO and hypochlorite oxidize most of the primary alcohols in pullulan while the residual secondary alcohols are not significantly affected. This method can also be employed to determine the total percentage of primary alcohols in polysaccharides.[34] Substitution reactions, such as acylation reactions of pullulan with polylactone are also consistent with regioselective reactions at primary alcohols.[35]

2.2.3 Dextran

Dextran is a lightly branched glucose polymer mostly composed of α-1,6-linkages whereas the sidechains are connected to the backbone through α-1,2-, α-1,3- or α-1,4 bonds (Figure 2.4). The average lengths of branched units are less than three units with a few long branched chains reported. Branching behavior was found to increase with increasing dextran molecular weight. Those branched sidechains have a tremendous influence on the self-organization of dextran relative to linear pullulan. Smaller radii of gyration relative to comparable molar mass pullulan are observed for dextran by light scattering. This behavior is attributed to the branched side units.[32]

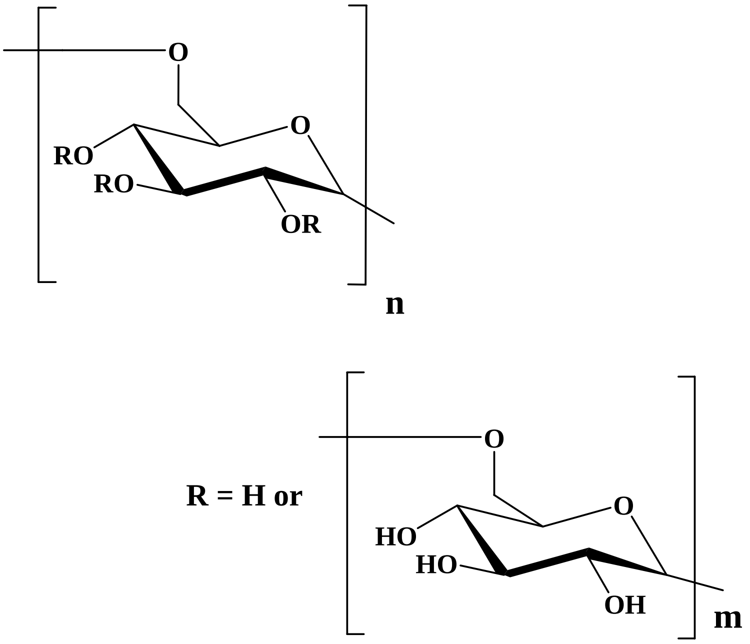

Figure 2.4. The repeating unit of dextran.

In contrast to pullulan, there are no primary alcohols in dextran. All three secondary alcohols exhibit similar reactivity in chemical reactions. Ferreira *et al.* [36] reported that the hydroxyl groups at positions 2 and 3 of dextran have nearly the same regioselectivity for reaction with vinyl acrylate. The isomer ratio for grafted vinyl acrylate at position 2 and 3 was determined to be 47:53 by nuclear magnetic resonance (NMR) spectroscopy. Dextran is usually used as a model system to study the self assembly behavior of modified polysaccharides. Amphiphilic polyester-modified dextran, like polylactide grafted dextran, exhibit lower glass transition temperatures, melting points and crystallinity compared to pure polylactide.[37] Various alkyl chains including octyl, dodecyl, or cetyl have been grafted onto the dextran in a random distribution.[38] The cationic ammonium groups on dextran give relatively low critical aggregation concentrations compared to neutral sidegroups. The degree of substitution (DS) and chain length of alkyl groups have a tremendous impact on the self-organization of dextran derivatives.

2.2.4 Curdlan

Curdlan obtained its name from its ability to curdle upon heat treatment. As seen in Figure 2.5, it is a linear polymer composed of β-1,3-glucosidic units, with DP values that can reach 450.[39] The linear chain structure of curdlan gives rise to a stiff polysaccharide backbone. Curdlan is nearly soluble in DI water, however, it dissolves in sodium salt solution through the break-up of hydrogen bonding within aggregates. There are many conformations for curdlan in aqueous media depending on the ionic strength of the solution from single to triple helices and even random coils.[40] As shown in Figure 2.6, curdlan has a random coil conformation in 0.24 M NaOH. At concentrations lower than 0.19 M NaOH(aq), curdlan exists in a helical conformation due to intramolecular and intermolecular hydrogen bonding. A conformational transition from helical structures to random coils was observed at NaOH concentrations of 0.19 to 0.24 M. Helices of curdlan can aggregate together to give microfibril structures which further organize into doughnut shaped granules. Pendant groups like sulfonylurea grafted onto carboxymethylated curdlan yield hydrogel nanoparticles.[41] Transmission electron microscopy revealed that those nanoparticles had an average diameter ~ 300 nm. Furthermore, the critical aggregation concentrations measured by fluorescence spectroscopy decrease as the DS of hydrophobic pendant groups increases. Two dimensional correlation NMR spectroscopy revealed that the first substitution by a sulfate side group in DMSO solvent occurred at the primary C6 alcohol due to its higher chemical reactivity and lower steric hindrance. With increasing DS, the residual secondary alcohols at the C2 and C4 positions were also substituted by sulfate groups with a slight preference at C2.[42]

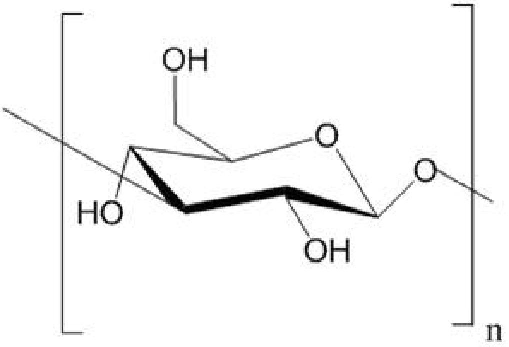

Figure 2.5. The repeating unit of curdlan.

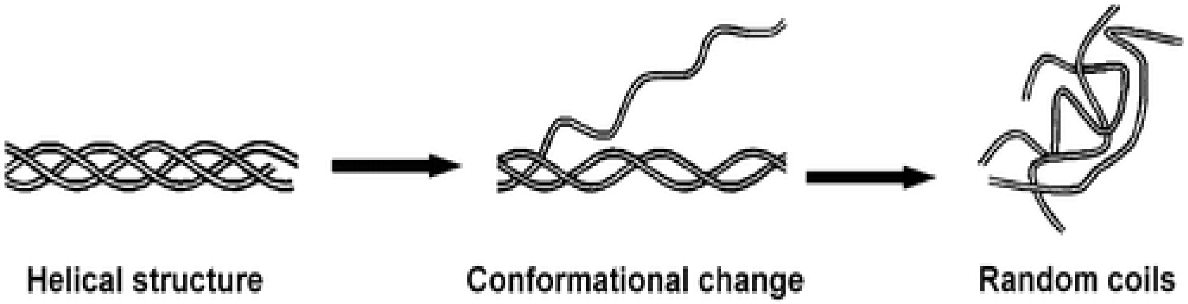

Figure 2.6. Conformational changes of curdlan in different alkaline solutions. Reprinted with permission from *Nano Letters* **2003**, *3*, 1119–1124. Copyright (2003) American Chemical Society.[40]

2.3 Modified Polysaccharide Esters and Ethers

2.3.1 Synthetic Polysaccharide Derivatives

There are many reported studies on the chemical modification of polysaccharides. Khan *et al.*[43] reported that dendritic side groups, namely the first and second generation amidoimide dendrons can be grafted onto ethyl cellulose via an ester linkage. To make the different generations of dendrons, the 2-ethylbutanoic acid was first reacted with diamine which was then coupled with succinic anhydride to give a carboxylic acid group. The dendronized polysaccharides were obtained by the reaction of the carboxylic acid groups in the dendron with the residual hydroxyl group on the ethyl cellulose backbones. Zhang *et al.*[44] reported a new kind of dendrimer modified cellulose derivative by incorporating a trifunctional aminoamide into the polysaccharides (see Figure 2.7). The derivatives show significantly different physical properties with more compact structures, more hydrophobic character, and decreased intrinsic viscosity compared to cellulose structures. The morphology of these dendronized polysaccharides were investigated by atomic force microscopy (AFM) after solution casting onto different surfaces.[45] An extended conformation was observed on a hydrophobic graphite surface while more polar mica sheets favored a compact spherical structure which was consistent with the aqueous state.

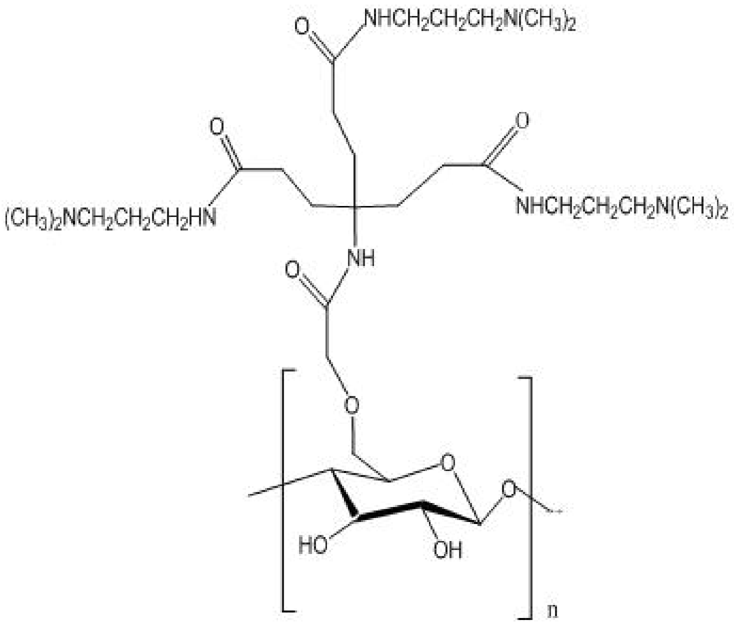

Figure 2.7. Chemical structure of tris(aminoamide) cellulose derivatives.

Two-dimensional correlation NMR spectroscopy has shown direct bonding between pendant polylactide groups and the dextran backbones.[37] The first proton of polylactide correlates with carbon atoms in the glucose units through the four-bond heteronuclear correlation (C-O-CO-C-H). This long range correlation was also reported for acetyl substituted pullulan.[46] The relatively short range correlation, a three bond correlation between acetyl carbon and pullulan protons (H-C-O-CO) can also be detected.

Chemical modification of pullulan with chloroformate and succinic anhydride was reported by Schacht *et al.*[47-49] Activation of the hydroxyl group was found to preferentially take place at the primary C-6 alcohol. The result was inferred from diminished intensity of the NMR signal at the OH-6 position. Side groups grafted onto the pullulan backbone can be covalently coupled to drug macromolecules facilitating usage of the assembly as drug carriers. Cholesterol-bearing pullulan (CHP) was reported to form stable and monodisperse nanoparticles by hydrophobic interactions above certain critical concentrations. Those nanoparticles were expected to adsorb onto various drugs and globular proteins.[50] Pullulan begins to degrade at a temperature of ~ 250 °C. To facilitate the use of pullulan at high temperatures, thermoplastic functional groups can be grafted onto the polysaccharide backbone. Acetylated pullulan prepared by the reaction of pullulan with acetic anhydride shows a glass transition temperature (T_g) around 160 °C.[51] Polycaprolactone and polylactide grafted pullulans synthesized by reactions with ε-caprolactone and L-lactide also show T_g.[35,37] Modification of pullulan by urethane groups to form isocyanate sidechains improved tensile strength.[52] The T_g was observed to decrease with increasing DS value.

2.3.2 Self-Assembly and Adsorption Behavior of Polysaccharide Derivatives

Steady-state fluorescence techniques are commonly employed to investigate self-association of polysaccharide derivatives, such as dextran substituted by cationic alkyl-ammonium groups,[38] in aqueous solution. Since the response of the fluorescent probe is largely determined by the polarity of the microenvironment, the point where fluorescence intensity drops and the point where it stabilizes at a new value as a function of polymer concentration can be used to determine the critical aggregation concentration (CAC). The formation of the hydrophobic microdomains depends upon DS and alkyl chain length. High DS and long alkyl chains contribute to a smaller CAC. Different association regimes were also studied by fluorescence and light scattering techniques.[53] With increasing polymer concentration, polysaccharides in micelle-like states will interact with other "micelles" to form an assembled gel phase. The connectivity of this network will lead to a bridge-to-loop transition under pressure with an attendant decrease in viscosity.

To study the self-organization of polysaccharide derivatives in aqueous solution, transmission and scanning electron microscopy were used. Wei and Cheng [54] found that above a certain critical concentration, the micelle structure would aggregate through hydrophobic associative interactions to form a network structure. Nanoparticles with diameters of 150-180 nm were observed for cholic acid substituted dextran.[55] The hydrophilic dextran backbones tend to internalize the hydrophobic domains to form a core where a fluorescent probe like pyrene can be entrapped inside. However, this core-shell amphiphilic structure is largely influenced by the pH of the solution with acidic environments causing the collapse of the nanoparticle.

The adsorption properties of carboxymethylpullulans (CMP) onto solid/liquid interfaces such as polystyrene latex particles were studied by Picton *et al.*[56] It was believed that hydrophobic interactions played a central role in CMP monolayer formation. This hydrophobic induced adsorption was affected by the ionic strength of the solution where desorption was observed in 0.01 M NaOH. Lee *et al.*[57] found that the self-assembled nanoparticles of CMP formed through hydrophobic interactions unfolded immediately after adsorption onto hydrophobic graphite surfaces. This finding was attributed to the collapse of the nanogel and direct bonding between the pendant hydrophobic groups and the graphite surface. On the other hand, lignin substituted heteroxylan retained a nanoparticle structure upon adsorption onto mica sheets.[58] The soft outer corona mainly composed by xylan was easily deformed in AFM experiments as tip force was applied. The relatively smaller heights of these particles (10-30 nm) compared to their diameters (200-300 nm) also gave evidence to the soft nature of those core-shell structures.

From insights gained through simulations, hydrogen bonding appears to play a significant role in the adsorption of carboxymethyl cellulose (CMC) onto solid surfaces. CMC polymers favor flat helical structures that allow greater exposure of hydroxyl groups to the adsorbed surface.[59] Mathematical modeling of adsorption isotherms supported a hydrogen bonding mechanism.

Even though pullulan is a water-soluble polymer without any surface activity at the air/water interface, its hydrophobically modified derivatives are amphiphilic polymers. The surface tension behavior of cholesterol-pullulan derivatives were investigated by Deme *et al.* at the air/water interface.[60] The hydrophobic cholesterol groups were believed to have a significant impact on the surface activity of modified pullulan derivatives, while the pure pullulan did not display any surface activity. It was also found that the surface potentials and self-organization behavior of cholesterol-pullulan monolayers at the interface were determined by the DS of the cholesterol group.[61] The surface area occupied by one CHP molecule decreased with increasing DS value. Akiyoshi *et al.* reported that hydrophobized pullulan with cholesterol groups was able to form colloidally stable nanoparticles with uniform size distributions.[50] Self-assembly behavior of CHP in solution was largely determined by its concentration. In dilute CHP solution, both light scattering and electron microscopy techniques gave evidence for the formation of hydrogel nanoparticles. A three-dimensional cross-linked gel structure was confirmed by electron microscopy at high concentrations. The mechanical properties such as response to external stimulus or viscosity changed dramatically in semi-dilute solutions.[62]

2.4 Lignin in Plant Cell Wall

In contrast to cellulose or hemicelluloses, lignins whose isolated molar masses can be as large as 15,000 g•mol^{-1} are not carbohydrates.[63] They are complex and three-dimensional polymers formed from phenolic units.[2] The basic units for lignins, also known as monolignols or phenylpropanes, are p-coumaryl alcohol, coniferyl alcohol, and sinapyl alcohol.[64] Monolignols produced in the cytoplasm are transported through the plasma membrane into the cell walls. Lignin is formed through the enzymatic dehydrogenation of monolignols which are further crosslinked by unsaturated double bonds through radical coupling.[65] Lignins with hemicelluloses are distributed between cellulose microfibrils in secondary plant cell walls and middle lamellae.[66] The presence of hydrophobic lignin in the cell walls leads to waterproof channels for water transport. The lignin network provides rigidity and protective coating to the cell walls. The primary disadvantage of lignins in cell wall structures is that they prevent further processing of wood materials and lead to recalcitrance against enzymatic bioconversion of biomass to biofuels.[67] Due to its poor solubility in almost all solvents, lignin is not easy to separate from other plant materials such as carbohydrates, phospholipids or proteins.[68] Through chemical or mechanical degradation treatments, lignins usually degrade into smaller fragments. It is interesting to note that the amorphous lignin polymer is basically optically inactive.[69]

2.5 Bioconversion of Plant Cell Wall Structures to Biofuels

In recent decades, much attention has been paid to bioconversion of biomass into biofuels due to soaring prices of fossil-based materials like petroleum.[70,71] Bioconversion of biomass, such as renewable lignocellulosic materials from plant cell walls, to biofuels by cellulolytic enzymes is a promising path to an alternative energy source. As one major component in plant cell walls, lignin, a complex cross-linked biopolymer, plays an important role in recalcitrance against bioconversion.[67] The strong interactions between phenolic lignin and cellulose or hemicellulose prevent enzyme accessibility and function. Pretreatment of biomass through physical-chemical approaches can break up recalcitrant structures and separate useful polysaccharides from the lignin structure.[72,73] As the mostly expensive part of the entire bioconversion process, the success of pretreatment has a tremendous impact on downstream processes.[74] Separated polysaccharides are transformed into monosaccharides by enzymatic hydrolysis.[75,76] Cellulases can break up β-(1-4)-glucosidic bonds between adjacent anhydroglucose units through an acid catalyzed hydrolysis mechanism. The enzymes are usually subdivided into three types: a) 1,4-β-D-glucan cellobiohydrolases (CBH), b) endoglucanases (EG) and c) β-glucosidases (BGL).[77-79] CBH favors interactions with the reducing and non-reducing ends of crystalline cellulose chains whereas EG randomly attacks the middle of the amorphous cellulose chains. Soluble cellobiose can be converted into glucose in the presence of BGL. Two important subdomains called the binding module (BM) and catalytic module (CM) exist in many cellulolytic enzymes.[80,81] The BMs in the cellulase stick to the cellulose surfaces followed by CMs chewing up the polymer chains (Figure 2.8). The adsorption of BMs to the cellulose chains should be reversible so that the cellulase can further work at other sites.[82] The hydrolytic products, mainly glucose, are converted to ethanol through fermentation by microorganisms in later stages of the bioconversion process.[83]

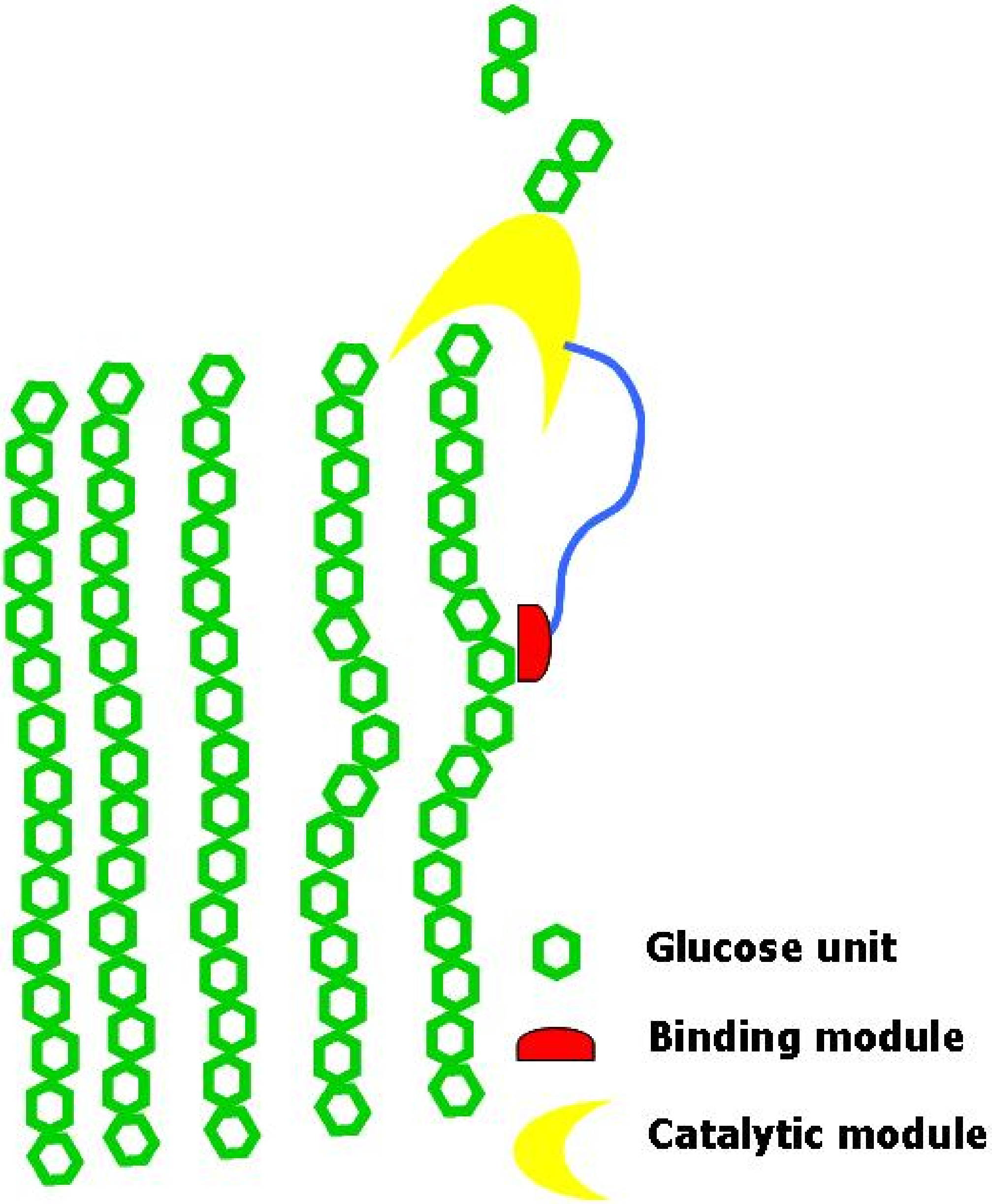

Figure 2.8. Hydrolysis of cellulose chains by enzymatic cellulase structures composed of a binding module and catalytic module.

2.6 Polymer Supported Phospholipid Bilayers

Uniform phospholipid bilayers can be deposited onto some hydrophilic substrates through the fusion of phospholipid vesicles.[84] Vesicles initially adsorb onto the surface, and then slide across the surface to form phospholipid bilayers. Phospholipid layers spontaneously propagate until the substrate is fully covered by bilayers. There exist two main forces in the fusion process depicted in Figure 2.9, *i.e.*, the adhesion force (F_a) and the bending force (F_b): [85,86]

$$F_a = -W \times A \qquad (2.1)$$

$$F_b = \left(\frac{k}{2}\right)\oint C^2 dA \qquad (2.2)$$

where W and A are the contact potential and contact area, respectively, and where k is the bending rigidity of the bilayers, and C is the vesicle curvature parameter. The collapse of the cell membrane by fusion occurs when F_a outweighs F_b. Figure 2.10 shows AFM height images of the solid/liquid interface of silica surfaces prior to and after phospholipid bilayer formation. The homogeneous biomimetic cell membrane on the solid substrate increases the root-mean-square surface roughness of the silica substrate from 0.6 nm to 0.8 nm.

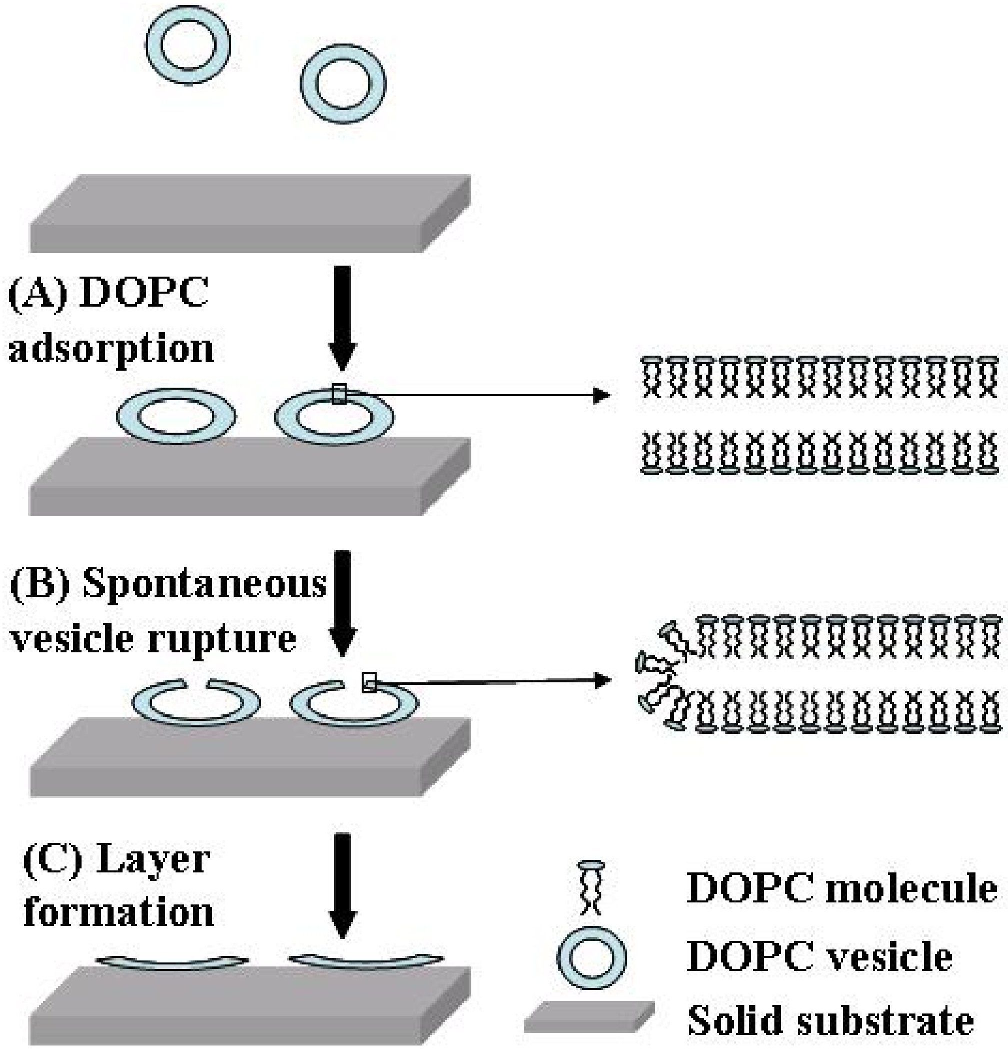

Figure 2.9. Schematic depiction of supported bilayer formation on a solid substrate through the fusion of phospholipid vesicles.

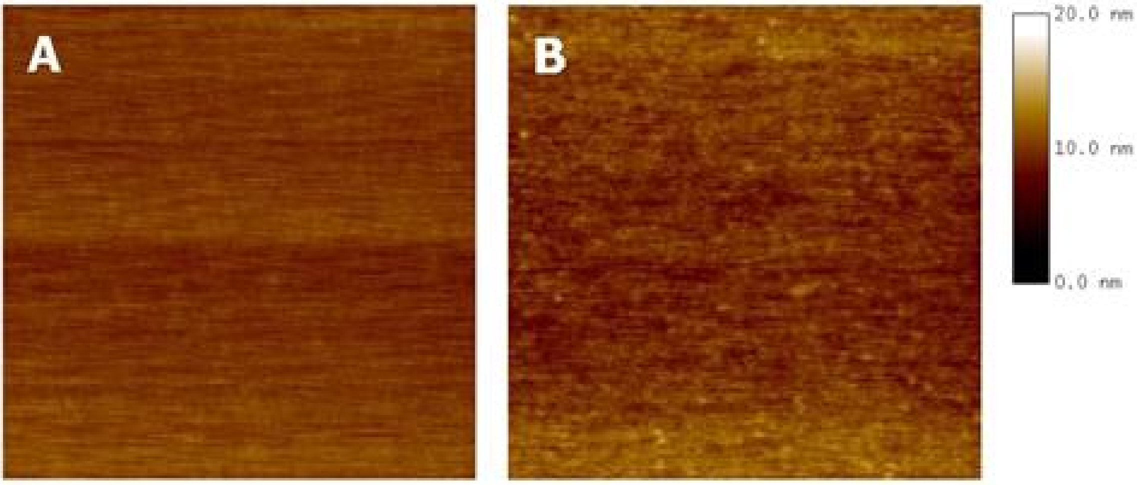

Figure 2.10. Representative AFM height images of the solid/liquid interface of silica surfaces (A) prior to and (B) after DOPC vesicle adsorption from a bulk solution (250 mg·L^{-1}). The AFM images are 2 μm x 2 μm and have Z-axis scales of 0 to 20 nm as indicated by the scale bar.

Reflection interference contrast microscopy experiments suggested two possible mechansims for vesicle fusion.[87] If the water shell between the bilayer and solid substrates is thick enough, the membrane slides to cover the surface. Otherwise, lobes of overlapped juxtaposed bilayers roll across the substrate to form the biomimetic cell membranes. The induced ruptures of intact vesicles by amphiphilic peptide[88,89] or polyethylene glycol[90] on substrates with a weaker F_a were studied to facilitate the transformation from vesicles to layer structures. Single-tail lysolipid micelles were also employed to trigger vesicle breakage in solutions.[91-93] The entire process was monitored by micropipette technique and optical microscopy. It was observed that the collapse of phospholipid vesicles only occurred after long-time exposure to lysolipid micelles above their critical micelle concentration.

Supported lipid membranes on ultrathin polymer films have many advantages relative to rigid solid substrates. Sufficient space between the bilayer and the substrate afforded by the polymer cushion on a substrate can prevent direct contact between trans-membrane proteins and the underlying substrate.[87,94] It also provides a stable and homogeneous model surface for fundamental investigations of membrane-related behaviors, like transmembrane proteins uptake or ion channels in cell membranes. Wiegand *et al.* first studied Langmuir transfer of a lipid bilayer onto cellulose surfaces.[95]

Meanwhile, cellulose fibers as the main component of plant cell walls play an important role in supporting plant cell membranes.[96,97] The growth of cellulose microfibrils by the cellulose synthase complex within the cell membrane may be elucidated through the study of interactions between cellulose and phospholipids.[98] That would inform the next generation of nanocomposites based upon biomimicry of plant cell wall structures.

2.7 Experimental Techniques

2.7.1 Preparation of Different Model Surfaces

2.7.1.1 Self-assembled Monolayers

To uniformly coat a gold surface with a polymer film, a clean gold substrate is often covered by a self-assembled monolayer (SAM). SAMs can form ordered molecular assemblies on surfaces that can be stable against various physical or chemical environments due to the strong interaction between the head group and substrate such as a S-Au bond as depicted in Figure 2.11.[99] The strong affinity of molecules in a SAM with the substrate allows the preparation of SAMs from the gas phase or from the solution. The binding of an alkyl thiol to a gold surface was accompanied by both oxidative addition of S-H bond to the gold surface and a reductive elimination of elemental hydrogen. The cleaned substrate should be immersed in a 1 mM SAM in ethanol solution for a period of time, and the monolayer will assemble spontaneously. The formed SAM structure is usually 1-3 nm thick. Depending on the terminal group (X) in Figure 2.9, the resulting SAM-X where X is a functional group, can make the gold substrates hydrophobic (SAM-CH_3), hydrophilic (SAM-OH), positively charged (SAM-NH_2) or negatively charged (SAM-COOH), and by no means cover all the functional groups that can be introduced.[100] For the specific examples given, comparisons of polysaccharide adsorption onto the SAMs and model regenerated cellulose or nanocrystalline cellulose surfaces give important insight into how different chemical functional groups influence adsorption.[16]

Love *et al.* discussed several parameters including temperature, solvents, SAM concentration and immersion time that might affect the quality of a SAM surface.[99] It was found that SAM surfaces spontaneously form at room temperature when the gold surface was immersed in a SAM solution of at least 1 M for 12 hours or more. Chemical reagents such as piranha solutions (H_2O_2: H_2SO_4) or plasma exposure can remove SAMs effectively. Mixed SAMs containing two different molecules can also be prepared by the co-adsorption of a mixture of thiols whose compositions can be easily controlled.[100]

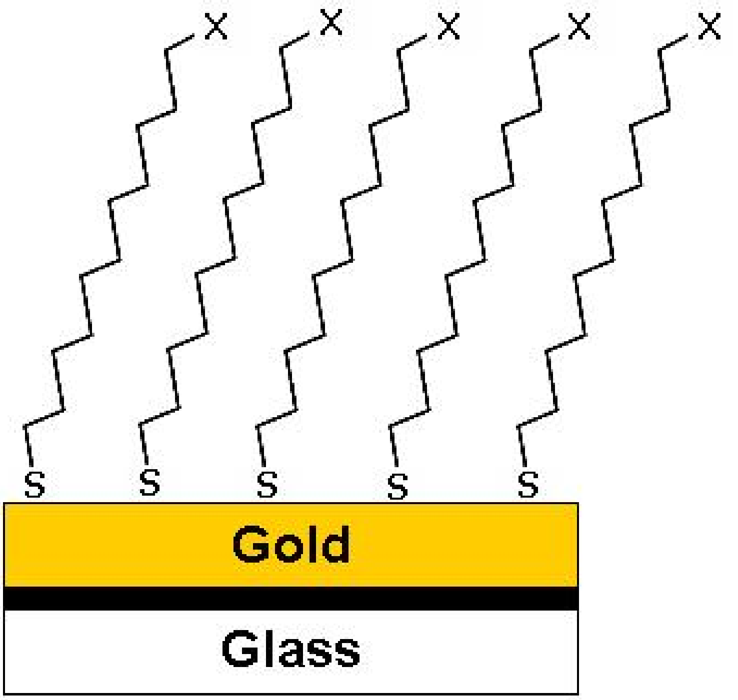

Figure 2.11. Schematic depiction of alkanethiols at the gold coated glass substrates through S-Au bonds. Terminal group could be CH_3, OH, COOH, NH_2, etc.

Ellipsometry and infrared spectroscopy studies indicated that long-chain and short-chain SAMs gave different surface properties upon adsorption onto the gold surface.[101] It was shown that long-chain SAMs can from a densely packed crystalline structure with alkyl chains tilted 20-30° from the surface normal. The thiol molecules occupied every available binding site until the alkyl chains assembled into an energetically favorable conformation. This adopted structure minimized the steric repulsions between the ordered chains. Low packing coverage and less organized structure were reported for short-chain SAMs. Different chain lengths also lead to different energy barriers for electron transfer during electrochemistry experiments. Long chain SAMs sustained by van der Waals interactions show a high dielectric constant and resistance to ion transport.

The surface used for SAM substrates can be prepared by physical vapor deposition methods to generate thin films of various metals. Prior to gold deposition on the glass or silicon wafer, an adhesion layer like chromium (~ 200 Å) should be deposited to improve adhesion between gold and the substrate. Cleaning of the gold substrate with strong oxidizing chemicals such as piranha solution prior to adsorption is necessary to ensure a clean surface. However, gold surfaces prepared by this method are too rough to use in atomic force microscopy. Template stripped gold surfaces can be employed to create a smooth gold surface whose roughness is less than 1 nm.[102] This technique takes advantage of the smooth and clean surface of freshly cleaved mica sheets by first coating the gold onto mica. Cleaned silicon wafers or glass slides are then attached to the gold-deposited mica sheets by Epo-tek 377. The epoxy glue is cured at 150° C for two hours. Prior to use, the gold surface is peeled off from the mica substrate. Immediate use after peeling provides a "clean" surface.

2.7.1.2 Cellulose Films Through The Langmuir-Blodgett Technique

The Langmuir-Blodgett (LB) technique can be used to deposit multilayers of amphiphilic molecules onto a solid substrate from air-liquid interfaces with well-controlled thicknesses.[103-105] Water and glycol have been reported as the liquid or subphase for Langmuir film studies.[106,107] Amphiphilic molecules composed of polar head groups and hydrophobic tail groups can form a layer at air/subphase interface, however, the most common interface is the air/water (A/W) interface.[108] The polar head groups attach to the subphase, whereas hydrophobic tail groups help to form two-dimensional insoluble films at the interface. Apart from small amphiphilic molecules such as fatty acids or phospholipids,[109] many amphiphilic polymeric materials can also form stable Langmuir films including poly(ethylene oxide),[110] polydimethylsiloxane,[111-113] poly(lactic acid)[114,115] and poly(ε-caprolactone).[116,117] Langmuir films can form different thermodynamic phases. A phase diagram is obtained by measuring the surface pressure (Π) versus molecular area (A) isotherm. The surface pressure is defined as:

$$\Pi = \gamma_0 - \gamma \qquad (2.3)$$

where γ is the surface tension of the Langmuir film and γ_0 is the surface tension of the subphase without amphiphilic molecules.

The amphiphilic molecules exist in a gaseous phase when the molecules are spread at sparse concentrations onto the A/W interface. When the monolayer is compressed by moveable barriers to control A, a liquid-expanded phase can appear where polar head groups are in close contact with each other accompanied by unoriented hydrophobic tails. In other cases, molecules can pack even more closely to form condensed phases when higher pressure is exerted on the monolayer. On Π versus A isotherms, steeper slopes are observed for condensed phases relative to liquid-expanded phases because of lower compressibility. The cross-sectional area of the molecules can be estimated from the molecular area at the condensed phase, the same point from which LB-transfer usually occurs.[108]

The transfer of the amphiphilic monolayers to solid substrates occurs on a LB-trough made of Teflon. Two movable barriers are used to control the surface pressure or surface area by compressing or expanding the monolayer. A Wilhelmy plate is most commonly employed to monitor Π with sensitivities ~ 10^{-1} mN/m by:

$$\Pi \cong \frac{F_0 - F}{2w} \qquad (2.4)$$

where F_0 and F are the forces measured by the paper plate for subphase and the amphiphile monolayer with w as the width of the plate.[107] While many molecules form Langmuir films, for condensed phases, the hydrophobic substrate is dipped into the subphase to pick up one layer. For some molecules, another layer can be deposited onto the monolayer covered substrate when the dipper is lifted out of the subphase. Controllable film thickness can be achieved by depositing the desired number of monolayers onto the substrates. LB-transfer of cellulose films onto hydrophobic silicon wafers by Y-type deposition (transfer of a monolayer on each up- and downstroke) was achieved for hundreds of layers.[25] The hydrophobic silicon, glass and gold substrate allow TMSC transfers by Y-type deposition. The silicon wafers, glass and gold slides are made hydrophobic by treating with NH_4F/HF, 1,1,1,3,3,3,-hexamethyldisilazane and immersion into alkanethiol self-assembled monolayer, respectively.[118]

2.7.1.3 Cellulose Films Obtained by Spincoating

The TMSC, a cellulose derivative with hydrophobic trimethylsilyl groups can also be spin coated onto silicon wafers to prepare well-defined TMSC films. Subsequent hydrolysis of TMSC to yield regenerated cellulose was completed by exposure to 10% (by weight) hydrochloric acid vapor for a brief time, (~ 120 seconds) at room temperature (Figure 2.12).[25] The cleavage of trimethylsilyl side groups by acid vapor leads to well-defined regenerated cellulose films with a 60% decrease of the total film thickness.

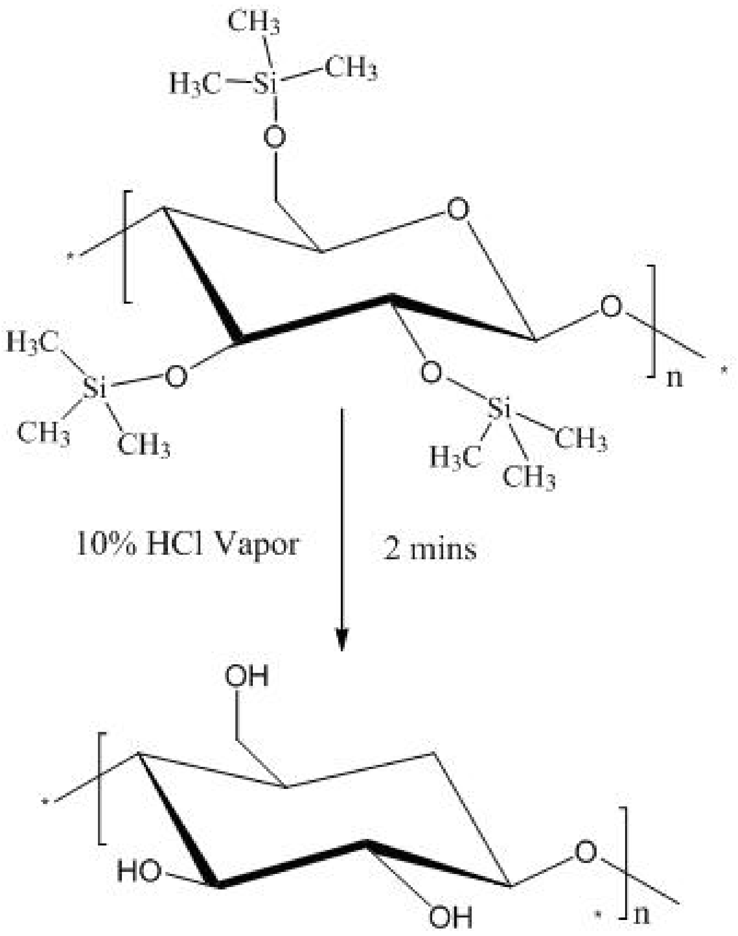

Figure 2.12. Desilylation of TMSC to form regenerated cellulose films. The process is driven by the release of $(CH_3)_3SiOSi(CH_3)_3$ gas.

Spincoating is far simpler than the LB-technique for the preparation of uniform films on flat substrates. The substrate with excess polymer solution is rotated at high speed (ca. 4000 revolutions per minute). Centrifugal force will spread the fluid. The resultant film thickness is a function of solution concentration, molar mass and spinning speed. The film thickness as a function of material and process parameters by spincoating is given by Middleman:[119]

$$\frac{H}{H_0} = \frac{1}{\sqrt{1 + \left(\frac{4\rho\omega^2}{3\mu}\right) H_0^2 t}} \qquad (2.5)$$

where H is the final thickness of the film after spincoating, H_0 is its initial thickness of the solution on the substrate, t is the spinning time, μ is fluid viscosity, ρ is fluid density, and ω is rotation speed. Note that for long spinning times, the initial amount of solution placed on the substrate has little effect on the final thickness of the film. Kontturi *et al.* first systematically studied the spin coating of TMSC onto different substrates in terms of various parameters such as spinning speed and concentration of TMSC in different solutions.[120,121] It was found that after acid vapor exposure, the resulting cellulose thin films were as good as pure cellulose even without the help of an anchoring polymer. It was also revealed that the resulting cellulose films are largely in an amorphous state by infrared spectroscopy.[16,120]

Nanocrystalline cellulose (NC) can be prepared by sulfuric acid hydrolysis of dissolving pulp.[21,22] The reaction was carried out by dissolving milled softwood sulfite pulp in sulfuric acid. The reaction was terminated by dilution of the reaction mixture with water. The sulfuric acid was removed from the cellulose suspension by centrifugation at 4900 rpm for 15 minutes. The product was dialyzed against water in dialysis tubing until the pH was constant. The final suspension was sonicated to separate cellulose aggregates and filtered through poly(vinylidene fluoride) (PVDF) syringe filter. The resulting nanocrystals were 5 nm wide with a length between 100 and 150 nm. To produce maximum surface charge densities, preparation parameters such as the concentration of the hydrolysis acid, temperature, and exposure time must be optimized.

The resulting negative surface charge on NC can be modified by exposing the suspensions to elevated temperatures. The heat treatment will release controlled amounts of sulfate groups from the nanoparticle surface.[22] To completely remove the sulfate groups on the surfaces of cellulose nanocrystals, the H_2SO_4-hydrolyzed cellulose suspension was neutralized with pyridine and lyophilized.[23] The freeze-dried product was dissolved in dimethylsulfoxide and methanol. The reaction continued for 2 h at 80 °C which was terminated by addition of cold water. The suspension was transferred to dialysis tubing and dialyzed against water. The final product was filtered through a 0.45 μm PVDF syringe filter. Cationic NC can be made by reacting the OH group of NC with epichlorohydrin followed by amination of the epoxy-activated cellulose with NH_4OH.[24] These amino groups will be positively charged in aqueous solution at $pH < 9$.

To help stabilize the spin-coated NC film, anchoring polymers are widely used. Ahola *et al.* used polyvinylamine, titanium oxide, 3-aminopropyltrimethoxysilane, polyvinylalcohol and polyethylenimine to stabilize weakly charged cellulose fibrils in aqueous solution.[27] By immersing the wafer in the anchoring polymer for 15 minutes, the polymer anchor will adsorb to the silicon oxide layer spontaneously through electrostatic interactions. After drying the polymer coated substrate in an oven for 1 to 2 hours at 75 °C, the cellulose suspension was spin coated onto the wafer. Quartz crystal microbalance (QCM) and AFM results show that weakly charged spincoated nanofibrils still remained at full coverage with only loosely attached fibrils being removed during processing. Moreover, the highly charged nanofibrils are stable against aqueous rinsing, even without an anchoring polymer layer. This result indicates that the charged fibrils are hydrogen bonded to the silica substrate. Thin layers of cellulose nanocrystal film could also be spincoated onto substrates to give a smooth model cellulose surface with a different surface morphology. [122] A subsequent mild heat treatment was required to stabilize the cellulose layer. It was shown that the root-mean-square roughnesses of desulfated NC films were greater relative to anionic NC films.

2.7.2 Surface Plasmon Resonance Spectroscopy

Surface plasmon resonance (SPR) spectroscopy is widely used to study adsorption behavior in biochemistry and chemistry because of its sensitivity to refractive index changes close to the sensor surface.[123] It is also commonly employed for biosensing applications and thin-film characterization. The Kretschmann prism arrangement depicted in Figure 2.13 is commonly used for the SPR measurements. The propagation vector of the incident light parallel to the surface can be used to excite a surface plasmon on the metal surface when total reflection at the glass/metal interface occurs. At total reflection, no transmission through the interface occurs, thus the light is merely confined within the glass. According to Snell's law:[124]

$$n_1 \sin\theta_1 = n_2 \sin\theta_2 \qquad (2.6)$$

where n_1 is the refractive index of medium 1, and n_2 is the refractive index of medium 2; total internal reflection occurs when the incident angle (θ_1) is equal to or above the critical angle (θ_c).[125] The critical angle is the incident angle where the refracted angle (θ_2) equals 90 degrees. Therefore, the critical angle can be expressed as:

$$\sin\theta_c = \frac{n_2}{n_1} \qquad (2.7)$$

Thin gold films with good optical properties, easily controlled thicknesses, and excellent stability are usually used as the metal surfaces. After deposition onto a glass substrate the gold metal will be optically coupled to a waveguide. The incident light from a p-polarized source first travels through the glass slide toward the ambient medium (aqueous solution in most cases) whose refractive index is lower than the wave guide. Most of the light is reflected back to the waveguide when the incident angle is larger than the critical angle θ_c. However, some of the incident light can escape the waveguide boundary and create an evanescent field which can penetrate through the thin gold film and couple with oscillating electrons on the gold surface to form a surface plasmon.[126]

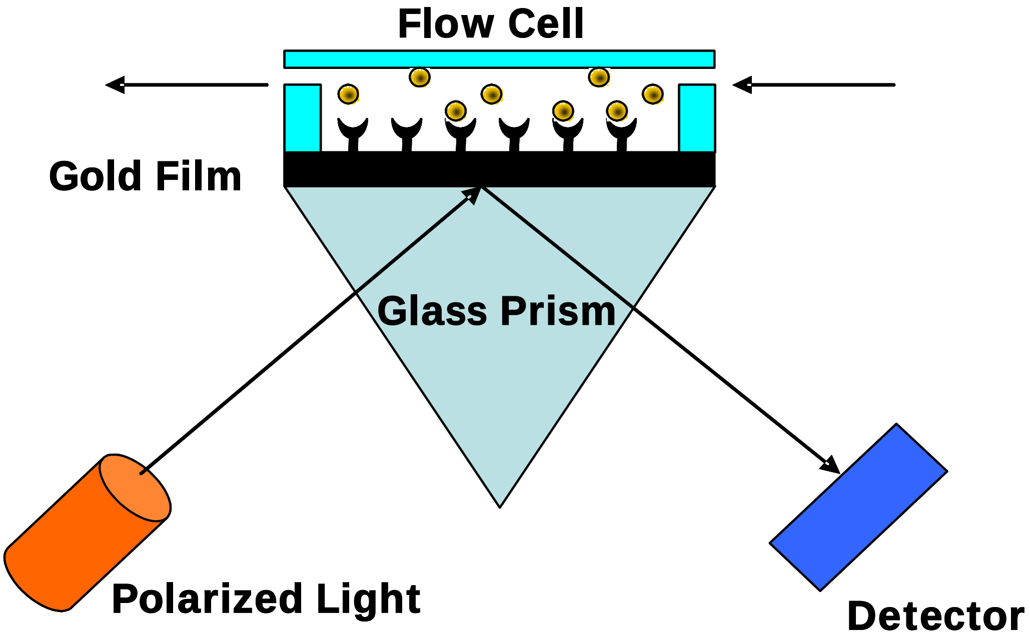

Figure 2.13. Schematic of the Kretschmann prism configuration.

The surface plasmon is confined at the interface of two materials with different dielectric constants, for example, metal/liquid interface. It is usually described by the followed equation,

$$k_{sp} = \frac{2\pi}{\lambda}\sqrt{\frac{\varepsilon_m \varepsilon_a}{\varepsilon_m + \varepsilon_a}} \qquad (2.8)$$

where λ is the light wavelength, ε_m is the dielectric permittivity of the metal, and ε_a is the dielectric permittivity of the ambient medium.[127] On the other hand, the propagation vector of the incident light traveling parallel to the surface can be expressed as,

$$k_x = \frac{2\pi}{\lambda}\sqrt{\varepsilon_g}\sin\theta \qquad (2.9)$$

where ε_g is the dielectric permittivity of the glass prism, θ is the angle of the incident light beam. The evanescent field can be coupled to the oscillating electron of the metal film leading to a resonance phenomenon when k_x is equal to k_{sp}. Given that $\sqrt{\varepsilon}$ = n (refractive index), with the condition $k_x = k_{sp}$, we can obtain the following equation:

$$n_g \sin\theta = \sqrt{\frac{n_m^2 n_a^2}{n_m^2 + n_a^2}} \qquad (2.10)$$

where θ is the incident angle, and n_g, n_m and n_a are the refractive index of the glass prism, metal surface and ambient medium, respectively. As resonance occurs at a critical incident angle, a minimum in the reflected intensity will be observed (Figure 2.14). According to Equation 2.10, the refractive index of the ambient medium is variable compared to other constants, thus the change in the resonance angle is a measure of the refractive index change of the ambient medium.

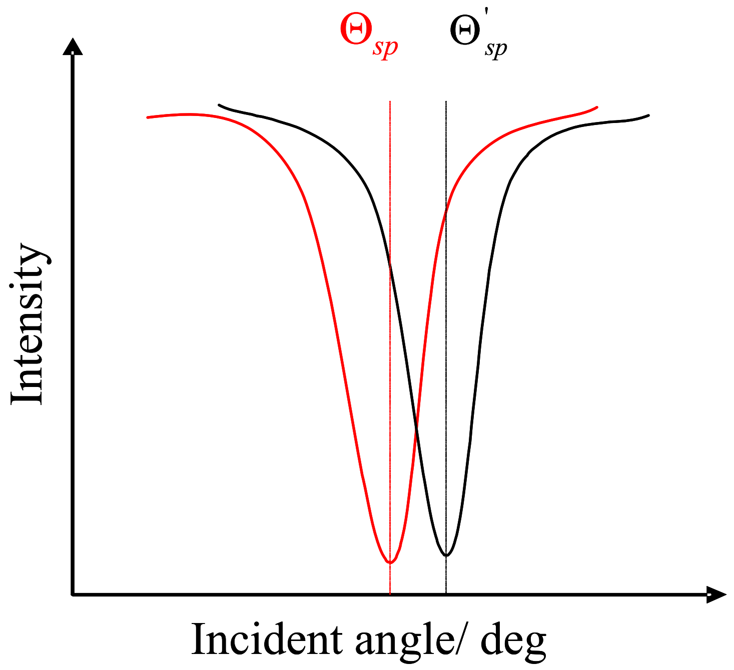

Figure 2.14. Change in SPR output from the red curve (Θ_{sp}) to the black curve in the presence of adsorbed materials (Θ'_{sp}).

On the other hand, the de Feijter equation gives a relationship between the refractive index change of the medium and the surface concentration of adsorbed materials on the metal surface (Γ):[128]

$$\Gamma = \frac{L \bullet \Delta n_a}{dn/dc} = \frac{\Delta\theta_a \bullet \Delta n_a}{(d\theta/dL)(dn/dc)} \qquad (2.11) \qquad (7)$$

where L is the thickness of the adsorbed layer, (dn/dc) is the refractive index increment of the adsorbed material, and Δn_a is the refractive index change of the ambient medium during the adsorption process. (dθ/dL) values for model surfaces can be given by a Matlab simulation code. To remove the bulk effect to the angle change, $\Delta\theta_a$ should be obtained from:

$$\Delta\theta_a = \Delta\theta_{tot} - c\left(\frac{d\theta_{sp}}{dn}\right)\left(\frac{dn}{dc}\right) \qquad (2.12)$$

where ($d\theta_{sp}$/dn) is the instrument parameter of SPR (61.5 °) and (dn/dc) is obtained from refractive index increment measurement. Since the response of SPR data to the adsorption process is a function of time, the de Feijter equation can be used to monitor the time-dependent change of adsorbed mass on the model surfaces.

Our group has done a series of systematic studies on pullulan derivative adsorption onto model surfaces by SPR.[15,16] It was found that with increasing DS, the adsorbed amount increases. The overall adsorption of pullulan cinnamate is relatively small on SAM-OH versus regenerated cellulose surfaces, however, larger adsorption on SAM-CH_3 surfaces is observed indicating the importance of hydrophobic interactions relative to the hydrogen bonding.

2.7.3 Atomic Force Microscopy

AFM is widely used to investigate the morphology of polysaccharides on surfaces.[129] There are a number of AFM studies on isolated cellulose fibers with high resolution, the size of which is consistent with features observed by electron microscopy.[130] As shown in Figure 2.15, the incident light reflected by the top of a micro cantilever onto a photodetector by an embedded mirror. With a sharp probe attached to the cantilever, the sample surface can be measured or manipulated. The probe, with a tip radius of nanometer scale, is usually made of silicon or silicon nitride. The interaction forces between the tip probe and the sample surface will lead to a deflection of the cantilever. By scanning the tip over the surface, the morphology of the surface will be obtained. The sample surface attached to a piezoelectric tube (usually by double-sided tape) can be moved in three dimensions by an applied electric field.[131] The lateral (x-y directions) and horizontal (z direction) resolutions of AFM instrument are usually better than 10 nm and 1 nm, respectively.

Depending on different research requirements, there are many available operation modes for AFM.[132] One primary mode is contact mode. In this mode, the deflection of the cantilever tip is kept constant to make sure the tip is always in close contact with the surface during scanning. However, if the tip is kept too close to the sample surface, strong lateral forces between the tip and the sample might destroy the surface. To minimize this disadvantage, the tapping mode, where the cantilever is externally driven to oscillate around its resonance frequency with a constant amplitude, is widely used. The interactions between the tip probe and the sample surface determines the change of oscillation amplitude with respect to the standard value, from which different types of materials could be discriminated on the sample surface. Additionally, phase imaging is a powerful tool to help identify different components in composite materials which are usually obscured in height imaging because of surface roughness. The phase lag of the cantilever oscillation, relative to the driving signal, is very sensitive to mechanical properties such as adhesion and viscoelasticity. The strong phase contrast between adsorbates and underlying model substrates facilitated unambiguous resolution of phase boundaries or edges. In experiments, height, phase and amplitude imaging were monitored simultaneously with no additional cost in scanning speed. Disadvantages of AFM include failure to identify elemental information of the sample materials. To overcome this, other force microscopy techniques have been developed such as chemical force microscopy, electric force microscopy and magnetic force microscopy to extract as much information as possible from surface studies.

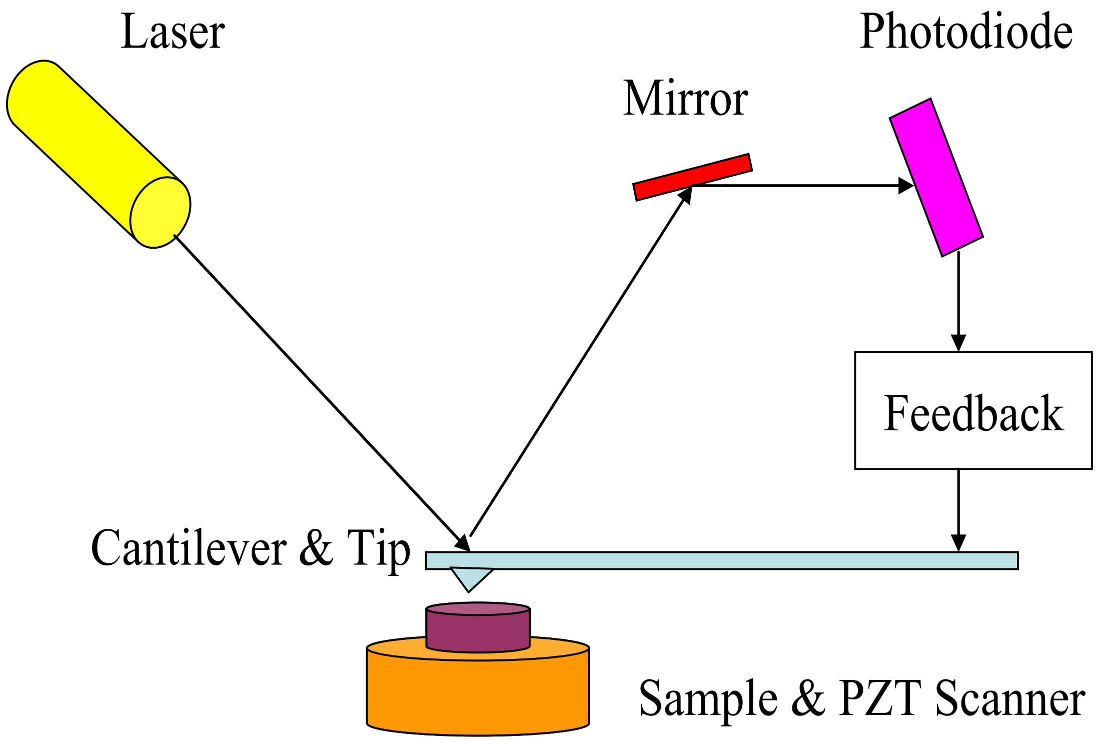

Figure 2.15. Schematic graph of atomic force microscopy

Apart from the surface morphology of a two-dimensional film examined in air, scientists are becoming more and more interested in the real time observation of the adsorption process in aqueous media. The equipment for an in-situ AFM instrument is shown in Figure 2.16 to study the morphology change at a solid/liquid interface. Rodlike micellar aggregates of poly-cetyltrimethylammonium 4-vinylbenzoate (poly-CTVB) at solid-liquid interfaces were observed through *in situ* AFM.[133] Adsorption of poly-CTVB in aqueous solution was observed by the help of a commercially available fluid cell. Prior to use, the fluid cell assembled with silicon nitride tip was attached to the substrate by the O-ring to mimic the real adsorption behavior like SPR or QCM fluid chamber. The solution of interest containing adsorbed materials was injected into the fluid cell by a syringe pump. However, there is no such investigation of polysaccharide derivatives to our knowledge. In-situ AFM could be used to observe the real time adsorption behavior of our system at solid/liquid interfaces.

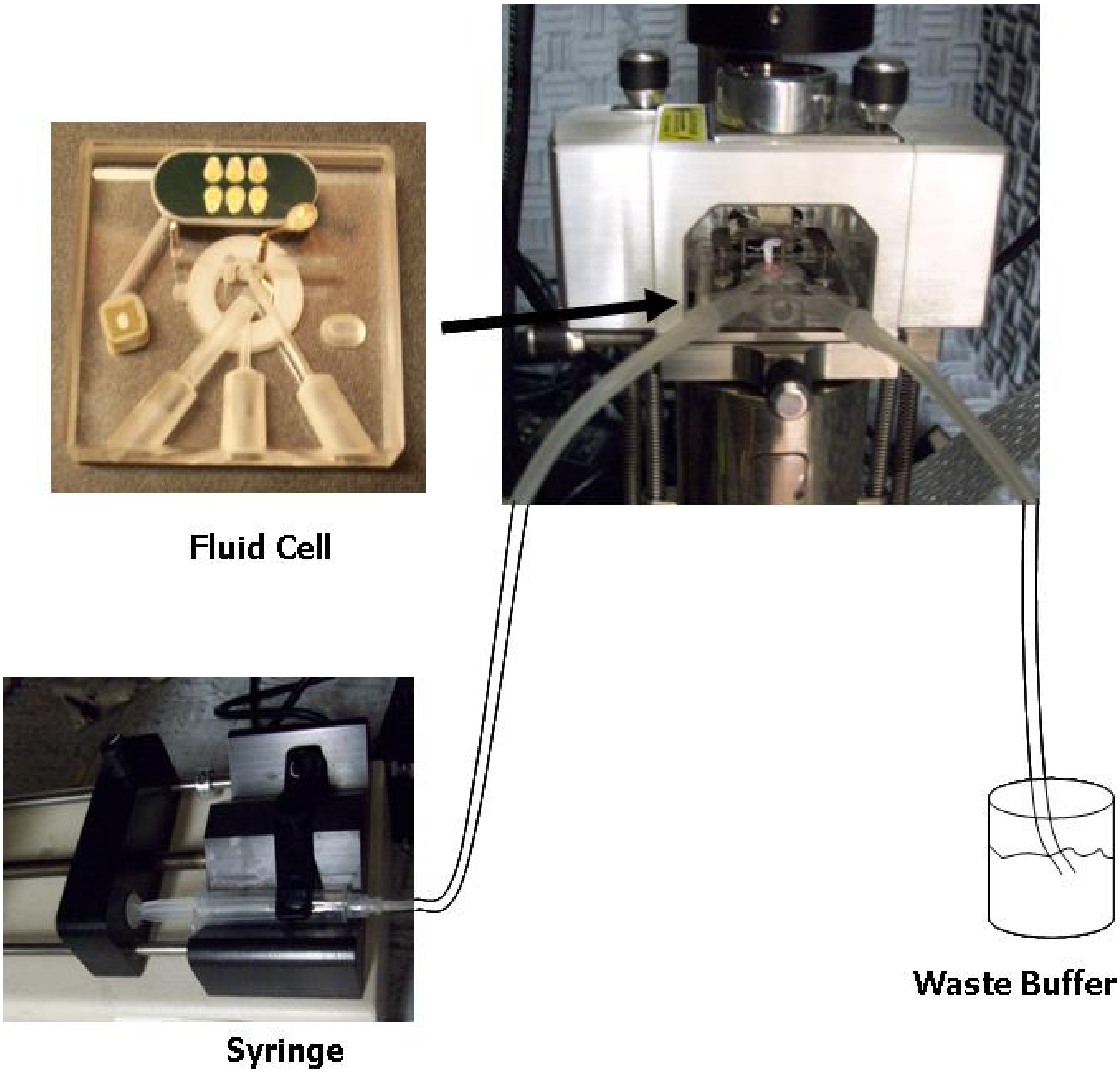

Figure 2.16. Equipment of an *in situ* AFM instrument to study morphology changes at solid/liquid interfaces.

2.7.4 Quartz Crystal Microbalance with Dissipation Monitoring

Because of high sensitivity to mass changes and the viscoelastic character of adsorbed materials at solid-liquid interfaces, quartz crystal microbalance with dissipation monitoring (QCM-D) is a versatile tool to study the interactions between biomolecules and model substrates in aqueous media. The instrument takes advantage of the piezoelectric effect in quartz crystals.[134]

The sensor slide from Q-Sense AB is AT-cut quartz crystal whose fundamental resonant frequency is 5 MHz with a diameter of 14 mm. The gold electrodes on the sensors are connected with an oscillator circuit which drives lateral oscillation of the quartz crystals (Figure 2.17). The adsorbed materials on the quartz crystals will move with the same amplitude and frequency as the quartz. Energy loss can be ignored for elastic films whereas there is always energy loss with oscillation for viscoelastic surfaces.

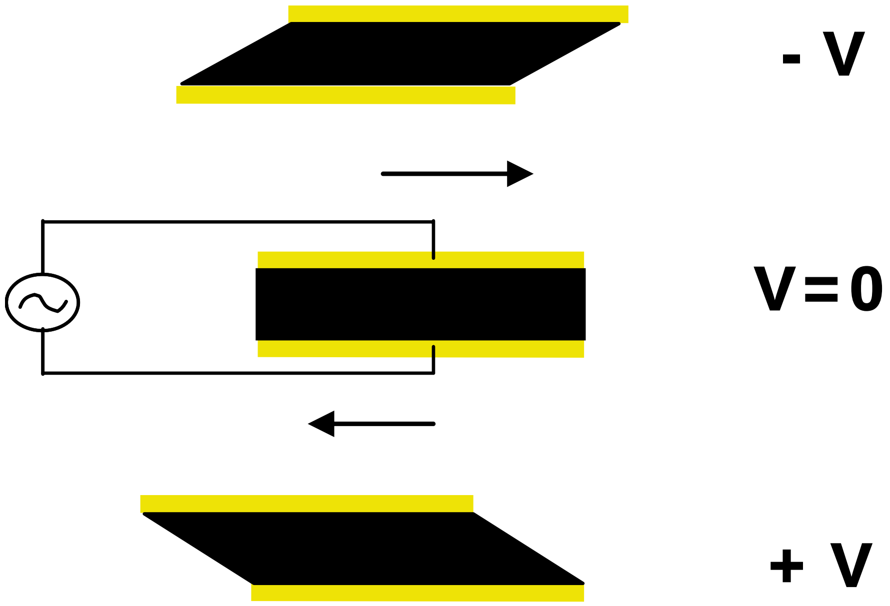

Figure 2.17. Gold-coated QCM quartz crystals in thickness shear mode oscillation.

The Sauerbrey equation is frequently used and predicts an approximately linear relationship between adsorbed mass (Δm) on rigid surfaces and the frequency change (Δf) observed in QCM-D measurements:[135]

$$\Delta m = -C \times \frac{\Delta f}{n} \qquad (2.13)$$

where C is the sensitivity constant (17.7 ng·cm^{-2}·Hz^{-1} for the QCM sensor slides with f = 5 MHz) and n is the overtone number. Recent work by Hook *et al.* and Craig *et al.* established a method to determine the solvent mass of a thin film via QCM-D measurements by deuterium exchange.[136,137] The adsorbed film in water was measured first, followed by deuterium oxide (D_2O) flowing over the film. The frequency shift caused by the increased mass of the solvent containing deuterium relates the frequency change arising from the coupled water within the film

$$\left(\frac{\Delta f_{H20}}{n}\right) = \frac{\left(\frac{\Delta f_{H20}}{n}\right)}{\left(\frac{\rho_{D2O}}{\rho_{H2O}}\right) - 1} \qquad (2.14)$$

where Δf_{H20} and Δf_{D20} are the frequency differences between the bare surface in water and the adsorbed film in media for H_2O and D_2O, respectively, and ρ_{H20} and ρ_{D20} are the densities of H_2O and D_2O, respectively. The Sauerbrey equation can be used to convert ($\Delta f_{H20}/n$) to a surface excess (Γ).

Dissipation measurements are facilitated by turning off the driving voltage while the decay of the crystal oscillation amplitude is simultaneously monitored.[138] The dissipation factor depends on multiple conditions including the viscoelasticity of the films, the surrounding aqueous media, *etc.*, and is defined as

$$D = \frac{E_{dissipated}}{2\pi E_{stored}} \qquad (2.15)$$

where $E_{\text{dissipated}}$ is the energy dissipated and E_{stored} is the energy stored during single oscillation cycle. As seen in Figure 2.18, energy dissipates very slowly on rigid films corresponding to small dissipation change (ΔD) whereas large ΔD is observed for floppy films with rapid decay rates.

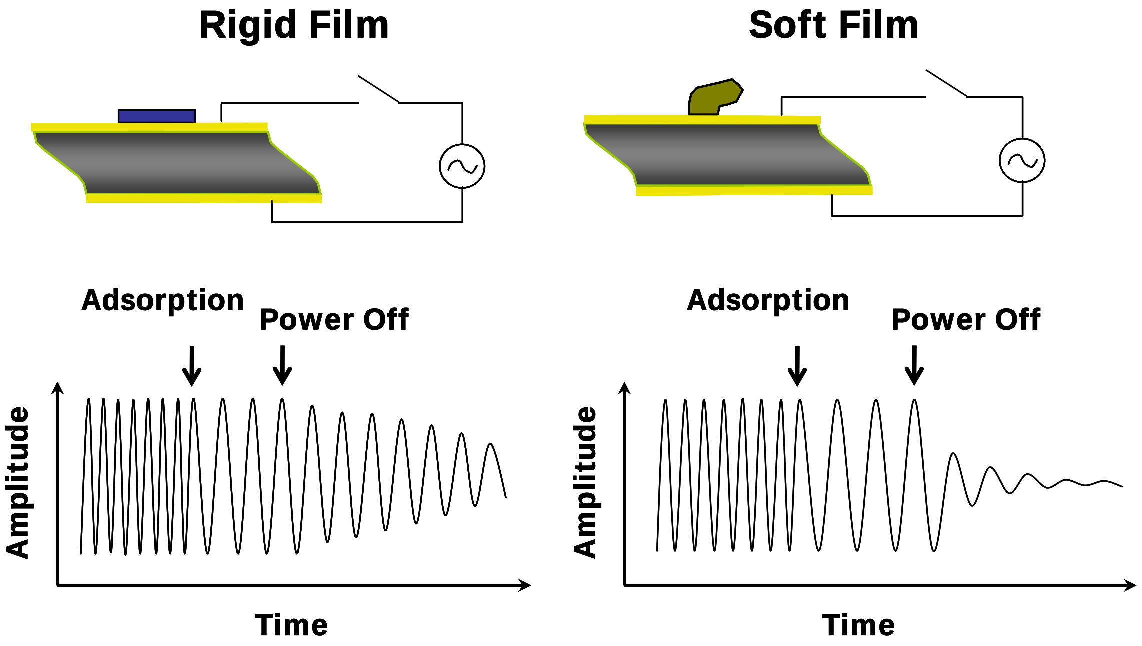

Figure 2.18. Schematic depiction of dissipation measurements for rigid and soft films after turning off the driving alternate current voltage.

Theoretical fitting based on a Voigt-based viscoelastic model is commonly employed to study the physical properties of soft layers with high viscosity and dissipation values at solid/liquid interfaces.[139] The Voigt-based model takes into account both elastic (storage) and viscous (damping) properties of the adsorbed materials. The shear modulus of the adsorbed layer can be described as :

$$G = \mu_f + i2\pi f\eta_f \qquad (2.16)$$

where μ_f is the elastic shear modulus (storage), η_f is the shear viscosity (loss), and f is the oscillation frequency. Assuming that the adsorbed layer is a homogeneous viscoelastic layer on elastic quartz crystals surrounded by a semi-infinite Newtonian fluid, there are four critical parameters to represent the adsorbed layer, including film thickness h_f, film density ρ_f, shear viscosity η_f, and elastic shear modulus μ_f. Δf and ΔD can be given by a Taylor expansion as follows:

$$\Delta f = \mathrm{Im}(\beta)/2\pi\rho_q h_q \qquad (2.17)$$

$$\Delta D = -\mathrm{Re}(\beta)/\pi\rho_q h_q f \qquad (2.18)$$

where

$$\beta = \xi_1 \frac{2\pi f\eta_f - i\mu_{\mathrm{f}}}{2\pi f}\frac{1-\alpha\exp(2\xi_1 h_f)}{1+\alpha\exp(2\xi_1 h_f)}$$

$$\alpha = \frac{\dfrac{\xi_1}{\xi_2}\dfrac{2\pi f\eta_f - i\mu_f}{2\pi f\eta_l}+1}{\dfrac{\xi_1}{\xi_2}\dfrac{2\pi f\eta_f - i\mu_f}{2\pi f\eta_l}-1}, \; \xi_1 = \sqrt{-\frac{(2\pi f)^2\rho_f}{\mu_f + i2\pi\eta_f}}, \; \xi_2 = \sqrt{i\frac{2\pi f\rho_l}{\eta_l}}$$

and ρ_q, h_q, ρ_l, and μ_l are the quartz density, quartz thickness, liquid density and liquid viscosity, respectively. The fitting was completed with Q-tools software from Q-Sense AB. The high overtone orders (n=5, 7 and 9) were used for estimation while low overtones such as n=1 and 3 were neglected because of insufficient energy trapping.[140] Since the acoustic mass from QCM-D measurements corresponds to the total mass including water content and adsorbed materials and the optical mass from SPR signals is only the dry mass of adsorbates (without coupled water), the combination of QCM-D and SPR results allows for the calculation of the degree of hydration of the adsorbed layers and affords a better understanding of interactions between adsorbates and model substrates.[136]

2.7.5 Fluorescence Spectroscopy

Fluorescence spectroscopy is widely used to study solution properties of surfactants or polymeric systems in the aqueous state. For example, the critical micelle concentration[38] and the association number of pedant groups are usually obtained by this method. Generally, fluorescent probe molecules are used to characterize the microenvironment of the polymer chains in solution. For the fluorescent probe pyrene, the intensity ratio between the first peak (λ = 373 nm) and the third one (λ = 384 nm) in the emission spectrum, I_1/I_3, strongly depends on the polarity of the pyrene microenvironment. I_1/I_3 is ~ 1.90 in water and ~ 0.70 in hexane, an apolar organic solvent (see Figure 2.19). An important advantage of pyrene is that it is preferentially soluble in micelles and hydrophobic aggregates relative to aqueous media. The variation of I_1/I_3 with surfactant concentrations was used to determine the critical aggregation concentration of amphiphilic polymer systems. Nichifor *et al.* investigated the self-association of alky-chain modified dextran.[38] The decrease and subsequent plateau of the fluorescent response with polymer concentration was significantly affected by both DS and alkyl chain length. It was believed that higher DS and longer alkyl pendant groups facilitate aggregation into hydrophobic microdomains. Fluorescence spectroscopy was also used to study aggregated phase regimes of hydrophobically modified chitosan.[53] The flowerlike micelles intermolecularly bridge to yield an aggregated gel phase above a critical concentration. Four regimes were reported from dilute polymer solution to phase separation.

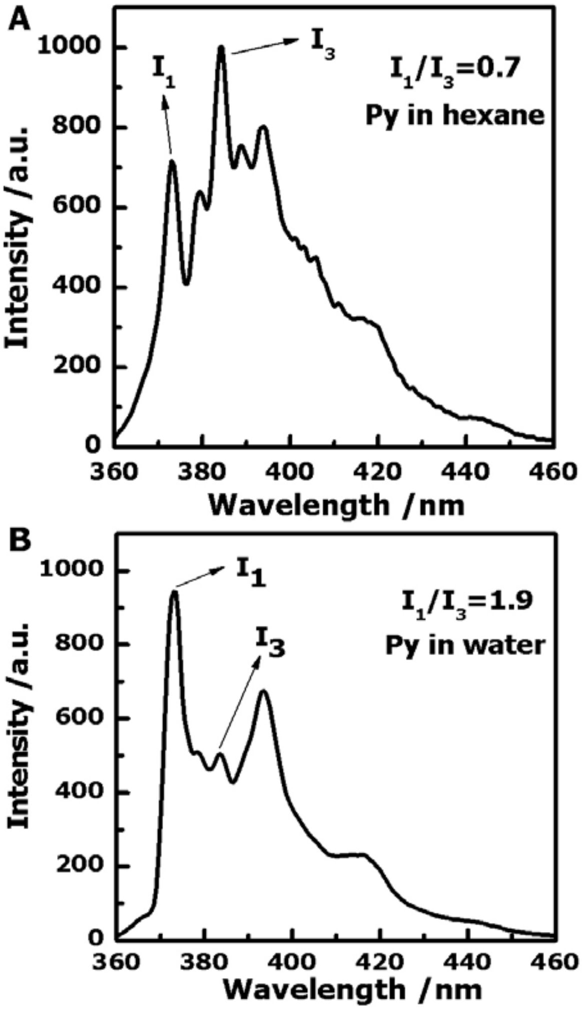

Figure 2.19 Emission spectra of pyrene dye in (A) hexane and (B) aqueous media.

To determine the aggregation number of pendant groups inside an aggregated microdomain, fluorescence quenching experiments are widely used.[141] The intensity of the first peak in emission spectra (I_1) of pyrene was probed as the quencher molecule concentration increased. The following equation is used:

$$\ln\frac{I_0}{I}=\frac{Q}{M} \qquad (2.19)$$

where M is the concentration of microdomain pendant groups, Q is the quencher concentration, and I and I_0 are the intensity of the first peak with and without quenching agents, respectively. From the slope of $\ln(I_0/I)$ with Q, the concentration of hydrophobic microdomains is obtained. Therefore, the aggregation number can be calculated as: $N=C_{sub}/M$, where C_{sub} is the concentration of pendant groups. The measurement is conducted at a polymer concentration where I_1/I_3 is kept constant. The aggregation number of pendant alkyl chains was found to be independent of DS and alkyl chain length over a wide range. Higher aggregation numbers relative to lower DS indicate several polymeric chains are required to interact with each other, and intermolecularly form one hydrophobic microdomain.

2.7.6 Transmission Electron Microscopy

To overcome the resolution limit of a light microscope, electron microscopy takes advantage of the short wavelength of electrons to observe nanostructures.[142,143] After emission from a filament, electrons are accelerated and focused by electric and magnetic fields in a vacuum chamber before reaching samples. Information about the tested samples, like electron density or phase behavior can be obtained from the transmitted electrons. For example, regions with high electron density appear dark, while bright areas mean low electron density or no sample is present. Selected area electron diffraction can be used to study the crystalline/amorphous domains of samples. The electron beam was first focused on interesting areas of sample film followed by switching from real space observation to phase space diffraction.

There have been numerous morphological studies of polysaccharide derivatives in aqueous solution by electron microscopy.[54,55] Core-shell amphiphilic structures have been reported where hydrophobic pendant groups are trapped inside the hydrophilic polysaccharide backbones to minimize the energy of the system. High DS for hydrophobic substituents is believed to promote nanoparticle formation. To prevent self-aggregation effects in polysaccharides, freeze-drying by a lyophilizer should be used before observations. Rouzes *et al.*[144] showed that freeze-drying largely decreased the extent of self-aggregation of dextran coated polylactide nanospheres while irregular aggregates were observed for samples dried in air.

2.7.7 Ellipsometry

Ellipsometry is an optical tool widely used to determine refractive index and thickness of thin films by analyzing reflected light at interfaces.[145-150] For a system composed of an ambient medium, film and substrate, the reflected light from the medium/film interface can interfere with the light reflected from the film/substrate interface. The wave amplitude of the combined light can either be increased or decreased if the two reflected beams are in phase or out of phase.[151,152] Therefore, the reflected light becomes elliptically polarized relative to the incident light. The elliptically polarized light can be divided into s and p polarized light where the ellipticity (ρ) can be expressed as the ratio of the amplitude reflection coefficients for s and p polarized light:

$$\rho = \frac{r_p}{r_s} = \tan\Psi \exp(i\Delta) \qquad (2.20)$$

where Δ is the phase difference between the s and p polarized light and Ψ is the attenuation of the light amplitude. In experimental measurements, we can either scan multiple wavelengths of an spectroscopic light source in the ultraviolet/visible regime or multiple incidence angles with a single wavelength light source (i.e. He:Ne laser, λ= 632.8 nm). By comparing the experimental data to the multilayer model set up in the fitting software like TFCompanion, the refractive index and film thickness can be resolved in a self-consistent simulation. For example, an initial guess will be used to construct the optical dispersion functions followed by comparison with the experimental data. Then the unknown parameter will be adjusted for a better fitting until the data matches the model. Our group has previously done much work on measuring optical properties of cellulose films by ellipsometry.[122,153] The thickness and refractive index of the film can be determined simultaneously by using multiple incident media without any mathematical modeling. The cellulose film thickness by spin coating is found to depend more strongly on the initial concentrations of cellulose solution rather than the spinning time.

2.7.8 Reflection Absorption Infrared Spectroscopy

The reflection absorption infrared spectroscopy (RAIRS) has been widely used to characterize physical properties and structural information of surfaces.[154-156] Compared to transmission IR experiments, RAIRS has great sensitivity to vibrations of molecules along the normal of the surface. The infrared radiation from a laser source is focused on and reflected at the sample/vacuum interface. The liquid-nitrogen cooled mercury−cadmium−telluride detector is employed to give a resolution of 2 cm^{-1}. The sample molecules can adsorb light at selected wavelengths corresponding to absorption peaks if the molecules have active dipole moments perpendicular to the surface. Since the focused light can only detect a small area of surface sample (~ 1 cm^2 or 1 nanomole), a Fourier transform IR spectrometer needs to be used to record spectra with a high resolution ~ 1 cm^{-1}**.** The incident light contains both s- and p-polarized components, however, only the p-polarized radiation perpendicular to the surface can excite the dipole moment because of the surface selection rules.[157,158]

2.8 References:

(1) Goldstein, I. S.; Gould, R. F. Eds.; American Chemical Society: Washington, D. C.: Washington, D. C., 1977; Vol. ACS Symposium Series, p 2-34.

(2) Thomas, R. J. *ACS Symposium Series* **1977**, *43*, 1-23.

(3) Reiter, W. D. *Current Opinion in Plant Biology* **2002**, *5*, 536-542.

(4) Hon, D. N.-S.; Shiraishi, N. Eds.; Marcel Dekker, Inc.: New York, N. Y., 2001, p 51-81

(5) Sticklen, M. B. *Nature Reviews Genetics* **2008**, *9*, 433-443.

(6) Dupuy, A. D.; Engelman, D. M. *Proc. Natl. Acad. Sci. U. S. A.* **2008**, *105*, 2848–2852.

(7) Alberts, B.; Johnson, A.; Lewis, J.; Raff, M.; Roberts, K.; Walter, P. Molecular Biology of the Cell, 4th Ed., Garland Science, New York, 2002.

(8) Lora, J. H.; Glasser, W. G. *Journal of Polymers and the Environment* **2002**, *10*, 39-48.

(9) Higuchi, T. *Journal of Wood Science* **2006**, *52*, 2-8.

(10) Suhas, P. J. M. C.; Carrott, M. M. L. R. *Bioresource Technology* **2007**, *98*, 2301-2312.

(11) Tsai, C. S. *Biomacromolecules: introduction to structure, function, and informatics*; John Wiley & Sons, Inc.: Hoboken, NJ, 2007.

(12) Mohanty, A. K.; Misra, M.; Drzal, L. T. *Composite Interfaces* **2001**, *8*, 313-343.

(13) Samir, M. A. S. A.; Alloin, F.; Dufresne, A. *Biomacromolecules* **2005**, *6*, 612-626.

(14) Berlin, A.; Balakshin, M.; Gilkes, N.; Kadla, J.; Maximenko, V.; Kubo, S.; Saddler, J. *J. Biotechnol.* **2006**, *125*, 198-209.

(15) Gradwell, S. E.; Renneckar, S.; Esker, A. R.; Heinze, T.; Gatenholm, P.; Vaca-Garcia, C.; Glasser, W. *C. R. Biol.* **2004**, *327*, 945-953.

(16) Kaya, A.; Du, X.; Liu, Z.; Lu, J. W.; Morris, J. R.; Glasser, W. G.; Heinze, T.; Esker, A. R. *Biomacromolecules* **2009,** *10*, 2451-2459.

(17) Singh, S. K.; Gross, R. A. *ACS Symposium Series* **2001**, *786*, 2-40.

(18) O'Sullivan, A. C. *Cellulose* **1997**, *4*, 173-207.

(19) Klemm, D.; Heublein, B.; Fink, H.-P.; Bohn, A. *Angewandte Chemie* **2005**, *44*, 3358-3393.

(20) Williamson, R. E.; Burn, J. E.; Hocart, C. H. *Cellular and Molecular Life Sciences* **2001**, *58*, 1475-1490.

(21) Edgar, C. D.; Gray, D. G. *Cellulose* **2003**, *10*, 299-306.

(22) Beck-Candanedo, S.; Roman, M.; Gray, D. G. *Biomacromolecules* **2005**, *6*, 1048-1054.

(23) Jiang, F.; Esker, A. R.; Roman, M. *Langmuir* **2010**, *26*, 17919–17925.

(24) Sines, B. J. “Evaluation of phenomena that determine the performance of immunoaffinity, peptide-based and ion exchange affinity sorbents” Dissertation, Virginia Polytechnic Institute and State University, Blacksburg, VA, 2000.

(25) Schaub, M.; Wenz, G.; Wegner, G.; Stein, A.; Klemm, D. *Adv. Mater.* **1993**, *5*, 919-922.

(26) Buchholz, V.; Wegner, G.; Stemme, S.; Ödberg, L. *Adv. Mater.* **1996**, *8*, 399-402.

(27) Ahola, S.; Salmi, J.; Johansson, L. S.; Laine, J.; Österberg, M. *Biomacromolecules* **2008**, *9*, 1273-1282.

(28) Sun, R.; Sun, X. F.; Tomkinson, J. *ACS Symposium* Series **2004**, *864*, 2-34.

(29) Ebringerova, A.; Hromadkova, Z.; Heinze, T. *Advances in Polymer Science* **2005**, *186*, 1-67.

(30) Shingel, K. I. *Carbohydr. Res.* **2004**, *339*, 447-460.

(31) Singh, S. K.; Gross, R. A. “Overview: Introduction to Polysaccharides, Agroprotein, and Poly (amino acids)” *Biopolymers from Polysaccharides and Agroproteins* Gross, R. A.;

Scholz, C.; Eds.; American Chemical Society: Washington, D. C., **2001**; Vol. ACS Symposium Series No. 786, 2-40.

(32) Nordmeier, E. *J. Phys. Chem.*, **1993**, *97*, 5770-5785.

(33) Henni, W.; Deyme, M.; Stchakovsky, M.; LeCerf, D.; Picton, L.; Rosilio, V. *Journal of Colloid and Interface Science* **2005**, *281*, 316-324.

(34) de Nooy, A. E. J.; Besemera, A. C.; Bekkum, H. *Carbohydrate Research,* **1995**, *269*, 89-98.

(35) Donabedian, D.; McCarthy, S. *Macromolecules* **1998**, *31*, 1032-1039.

(36) Ferreira, L.; Gil, M. H.; Dordick J. S. *Biomaterials* **2002,** *23*, 3957–3967.

(37) Nouvel, C.; Dubois, P.; Dellacherie, E.; SIX J. *Journal of Polymer Science: Part A: Polymer Chemistry* **2004**, *42*, 2577–2588.

(38) Nichifor, M.; Lopes, S.; Bastos, M.; Lopes, A. *J. Phys. Chem. B* **2004**, *108*, 16463-16472.

(39) Phillips, G. O.; Williams, P. A."Handbook of Hydrocolloids", *CRC Press*, **2000**, 269-286.

(40) Zhang, L.; Wang, C.; Cui, S.; Wang, Z.; Zhang, X. *Nano Letters* **2003**, *3*, 1119–1124.

(41) Na, K.; Park, K. H.; Kim, S. W.; Bae, Y. H. *Journal of Controlled Release* **2000**, *69*, 225-236.

(42) Yoshida, T.; Hatanaka, K.; Uryu, T.; Kaneko, Y.; Suzuki, E.; Miyano, H.; Mimura, T.; Yoshida, O.; Yamamoto N. *Macromolecules*, **1990**, *23*, 3717-3722.

(43) Khan, F. Z.; Shiotsuki, M.; Nishio, Y.; Masuda, T. *Macromolecules* **2007,** *40*, 9293-9303.

(44) Zhang, C.; Price, L. M.; Daly W. H. *Biomacromolecules* **2006,** *7*, 139-145.

(45) Östmark, E.; Lindqvist, J.; Nyström, D.; Malmström, E. *Biomacromolecules* **2007,** *8*, 3815–3822.

(46) Tezuka Y. *Carbohydrate Research* **1998,** *305*, 155-161.

(47) Bruneel, D.; Schacht, E. *Polymer* **1993**, *34*, 2628-32.

(48) Bruneel, D.; Schacht, E. *Polymer* **1993**, *34*, 2633-7.

(49) Bruneel, D.; Schacht, E. *Polymer* **1994**, *35*, 2656-8.

(50) Akiyoshi, K.; Deguchi, S.; Moriguchi, N.; Yamaguchi, S.; Sunamoto, J. *Macromolecules* **1993**, *26*, 3062-3068.

(51) Donabedian, D.; Gross, R.; McCarthy, S. *Polym Prepr* (Am Chem Soc, Mater Sci Engng) **1992**, *67*, 301-305.

(52) Shibata, M.; Asahina, M.; Teramoto, N.; Yosomiya, R. *Polymer* **2000**, *42*, 59-64.

(53) Esquenet, C.; Terech, P.; Boué, F.; Buhler, E. *Langmuir* **2004**, *20*, 3583-3592.

(54) Wei, Y.; Cheng F. *Carbohydrate Polymers* **2007** , *68*, 734–739.

(55) Yuan, X. B.; Li, H.; Zhu X. X.; Woo H. G. *J Chem Technol Biotechnol* **2006**, *81*, 746–754.

(56) Simon, S.; Picton, L.; Le Cerf, D.; Muller, G. *Polymer* **2005**, *46*, 3700-3707.

(57) Lee, I.; Akiyoshi, K. *Biomaterials* **2004**, *25*, 2911–2918.

(58) Barakat, A.; Gaillard, C.; Lairez, D.; Saulnier, L.; Chabbert, B.; Cathala, B. *Biomacromolecules* **2008,** *9,* 487–493.

(59) Wang, J.; Somasundaran, P. *Journal of Colloid and Interface Science* **2005**, *291*, 75–83.

(60) Deme, B.; Rosilio, V.; Baszkin, A. *Colloids and Surfaces, B: Biointerfaces* **1995**, *4*, 357-365.

(61) Deme, B.; Rosilio, V.; Baszkin, A. *Colloids and Surfaces, B: Biointerfaces* **1995**, *4*, 367-73.

(62) Kuroda, K.; Fujimoto, K.; Sunamoto, J.; Akiyoshi, K. *Langmuir* **2002**, *18*, 3780-3786.

(63) Lin, S. Y.; Dence, C. W. In *Methods in Lignin Chemistry*; Lin, S. Y., Dence, C. W., Eds.; Springer-Verlag: Berlin: Berlin, 1992.

(64) Suhas; Carrott, P. J. M.; Carrott, M. M. L. R. *Bioresource Technology* **2007**, *98*, 2301-2312.

(65) Alen, R. In *Forest Products Chemistry*; Stenius, P., Ed.; Fabet Oy: Jyvaskyla, Finland, 2000, p 11-57

(66) Higuchi, T. *Journal of Wood Science* **2006**, *52*, 2-8.

(67) Cosgrove, D. J. *Nat. Rev. Mol. Cell Biol.* **2005**, *6*, 850-861.

(68) Goring, D. A. I. *ACS Symposium Series* **1989**, *397*, 2-10.

(69) Sakakibara, A.; Sano, Y. In *Wood and Cellulosic Chemistry*; 2nd ed.; Hon, D. N.-S. and Shiraishi, N., Eds.; Marcel Dekker, Inc.: New York, NY, 2001, p 109-173

(70) Nonhebel, S. *Renew. Sustain. Energy Rev.* **2005**, *9*, 191-201.

(71) Tilman, D.; Hill, J.; Lehman, C. *Science* **2006**, *314*, 1598-600.

(72) Dale, B. E.; Leong, C. K.; Pham, T. K.; Esquivel, V. M.; Rios, I.; Latimer, V. M. *Bioresource Technology* **1996**, *56*, 111-116.

(73) Kim, K. H.; Hong, J. *Bioresource Technology* **2001**, *77*, 139-144.

(74) Lynd, L. R. *Annual Review of Energy and the Environment* **1996**, *21*, 403-465.

(75) Joergensen, H.; Kristensen, J. B.; Felby, C. *Biofuels, Bioprod. Biorefin.* **2007**, *1*, 119-134.

(76) Schubert, C. *Nat. Biotechnol.* **2006**, *24*, 777-784.

(77) Lynd, L. R.; Weimer, P. J.; van Zyl, W. H.; Pretorius, I. S. *Microbiol. Mol. Biol. Rev.* **2002**, *66*, 506-577.

(78) Henrissat, B.; Teeri, T. T.; Warren, R. A. J. *FEBS Lett.* **1998**, *425*, 352-354.

(79) Terri, T. T. *Trends Biotechnol.* **1997**, *15*, 160-167.

(80) Teeri, T. T.; Koivula, A.; Linder, M.; Wohlfahrt, G.; Divne, C.; Jones, T. A. *Biochem. Soc. Trans.* **1998**, *26*, 173-178.

(81) Carrard, G.; Koivula, A.; Soderlund, H.; Beguin, P. *Proc. Natl. Acad. Sci.* **2000**, *97*, 10342-10347.

(82) Palonen, H.; Tjerneld, F.; Zacchi, G.; Tenkanen, M. *J. Biotechnol.* **2004**, *107*, 65-72.

(83) Berlin, A.; Balakshin, M.; Gilkes, N.; Kadla, J.; Maximenko, V.; Kubo, S.; Saddler, J. *J. Biotechnol.* **2006**, *125*, 198-209.

(84) Keller, C. A.; Glasmastar, K.; Zhdanov, V. P.; Kasemo, B. *Phys. Rev. Lett.* **2000**, *84*, 5443-5446.

(85) Seifert, U.; Lipowsky, R. *Phys. Rev. A* **1990** *42*, 4768.

(86) Reviakine, I.; Brisson, A. *Langmuir* **2000**, *16*, 1806.

(87) Sackmann, E. *Science* **1996**, *271*, 43-48

(88) Cho, N.; Wang, G.; Edvardsson, M.; Gleen, J. S.; Hook, F.; Frank, C. W. *Anal. Chem.* **2009**, *81*, 4752-4761.

(89) Cho, N. J.; Cho, S. J.; Cheong, K. H.; Glenn, J. S.; Frank, C. W. *J. Am. Chem. Soc.* **2007**, *129*, 10050-10051.

(90) Proux-Delrouyre, V.; Elie, C.; Laval, J.; Moiroux, J.; Bourdillon, C. *Langmuir* **2002**, *18*, 3263-3272

(91) Needham, D.; Stoicheva, N.; Zhelev, D. V. *Biophysical Journal* **1997**, *73*, 2615-2629.

(92) Hamai, C.; Yang, T.; Kataoka, S.; Cremer, P. S.; Musser, S. M. *Biophysical Journal* **2006**, *90*, 1241-1248.

(93) Hamai, C.; Cremer, P. S.; Musser, S. M. *Biophysical Journal* **2007**, *92*, 1988-1999.

(94) Tanaka, M.; Sackmann, E. *Nature* **2005**, *437*, 656-663.

(95) Wiegand, G.; Jaworek, T.; Wegner, G.; Sackmann, E. *Langmuir* **1997**, *13*, 3563-3569.

(96) Dupuy, A. D.; Engelman, D. M. *Proc. Natl. Acad. Sci. U. S. A.* **2008**, *105*, 2848–2852.

(97) Alberts, B.; Johnson, A.; Lewis, J.; Raff, M.; Roberts, K.; Walter, P. Molecular Biology of the Cell, 4th Ed., Garland Science, New York, 2002.

(98) Yennawar, N. H.; Li, L.; Dudzinski, D. M.; Tabuchi, A. ; Cosgrove, D. J. *Proc. Natl. Acad. Sci. U. S. A.* **2006**, *103*, 14664-14671.

(99) Love, J. C.; Estroff, L. A.; Kriebel, J. K.; Nuzzo, R. G.; Whitesides G. M. *Chem. Rev.* **2005**, *105*, 1103-1169.

(100) Nuzzo, R. G.; Allara, D. L. *Journal of the American Chemical Society* **1983**, *105*, 4481-4483.

(101) Porter, M. D.; Bright, T. B.; Allara, D. L.; Chidsey, C. E. D. *Journal of the American Chemical Society* **1987**, *109*, 3559-3568.

(102) Wagner, P.; Hegner, M.; Guentherodt, H. J.; Semenz, G. *Langmuir*, **1995**, *11*, 3867-3875.

(103) Langmuir, I. *Trans. Faraday Soc.* **1920**, *15*, 62-74.

(104) Blodgett, K. B. *J. Am. Chem. Soc.* **1935**, *57,* 1007-1022.

(105) Blodgett, K. B.; Langmuir, I. *Phys. Rev.* **1937**, *51*, 964-982.

(106) Barraud, A.; Leloup, J.; Lesieur, P. *Thin Solid Films* **1985**, *133*, 113-116.

(107) Gaines, G. L. Insoluble monolayers at liquid-gas interface, Interscience, New York, 1966.

(108) Petty, M. C. Langmuir-Blodgett films: an introduction, Cambridge University Press, Cambridge, 1996.

(109) Kaganer, V. M.; Mohwald, H.; Dutta, P. *Rev. Mod. Phys.* **1999,** *71,* 779-819.

(110) Cheyne, R. B.; Moffitt, M. G. Langmuir, **2006**, *22*, 8387-8396.

(111) Buzin, A. I.; Godovsky, Y. K.; Makarova, N. N.; Fang, J.; Wang, X.; Knobler, C. M. *J. Phys. Chem. B* **1999,** *103,* 11372-11381.

(112) Granick, S.; Clarson, S. J.; Formoy, T. R.; Semlyen, J. A. *Polymer* **1985,** *26,* 925- 929.

(113) Hottle, J. R., Deng, J. J.; Kim, H. J.; Esker, A. R. *Langmuir* **2005**, *21*, 2250-2259.

(114) Ni, S.; Lee, W.; Li, B.; Esker, A. R. *Langmuir* **2006,** *22,* 3672-3677.

(115) Pelletier, I.; Pezolet, M. *Macromolecules* **2004,** *37,* 4967-4973.

(116) Li, B.; Wu, Y.; Liu, M.-H.; Esker, A. R. *Langmuir* **2006,** *22,* 4902-4905.

(117) Lee, W. K.; Gardella, J. A. *Langmuir* **2000,** *16*, 3401-3406.

(118) Gunnars, S.; Wågberg L.; Cohen Stuart M.A. *Cellulose* **2002**, *9*, 239–249.

(119) Middleman, S. *J. Appl. Phys.* **1987**, 62, 2530-2532.

(120) Kontturi, E.; Thune, P. C.; Niemantsverdriert, J. W. *Langmuir* **2003**, *19*, 5735-5741.

(121) Kontturi, E.; Thune, P. C.; Niemantsverdriet, J. W. *Polymer* **2003**, *44*, 3621-3625.

(122) Kittle, J. D.; Du, X.; Jiang, F.; Qian, C.; Roman, M.; Heinze, T.; Esker, A. R. *Biomacromolecules,* **2011**, *12*, 2881-2887.

(123) Earp, R. L.; Dessy, R. E. *Commercial Biosensors: Applications to Clinical, Bioprocess, and Environmental Samples*; Ramsay, G., Ed.; John Wiley & Sons, Inc.: New York, **1996**, 99-164.

(124) Liedberg, B.; Johansen, K. In *Affinity Biosensors*; Rogers, K. R., Mulchandani, A., Eds.; Humana Press: Totowa, N.J., **1998**.

(125) Hecht, E.; Zajac, A. *Optics* Addison-Wesley Publishing Company, Inc. USA, **1975**.

(126) Green, R. J.; Frazier, R. A.; Shakesheff, K. M.; Davies, M. C.; Roberts, C. J.; Tendler, S. J. B.; *Biomaterials* **2000**, *21*, 1823-1835.

(127) Van Krevelen, D. W. *Properties of Polymers: Their Correlation with Chemical Structure; Their Numerical Estimation and Prediction from Additive Group Contributions*; third, completely revised ed.; Elsevier: Amsterdam, **1997**.

(128) de Feijter, J. A.; Benjamins, J.; Veer, F. A. *Biopolymers* **1978**, *17*, 1759-1772.

(129) Morris, V. J.; Kirbt, A. R.; Gunning, A. P. "Atomic Force Microscopy for Biologist." Imperial College Press, **1999**.

(130) Hanley, S. J.; Revol, J-F.; Gray, D. G. *Cellulose* **1997**, *4*, 209-220.

(131) Amato, I. *Science* **1997**, *276*, 1982-1985.

(132) Wang, Z. L.; Liu, Y.; Zhang Z. "Handbook of Nanophase and Nanostructured Materials: Materials Systems and Applications I" *Springer*, **2003**.

(133) Biggs, S.; Kline, S. R.; Walker L. M. *Langmuir* **2004**, *20*, 1085-1094.

(134) Curie, J.; Curie, P. *Comput. Rend. Acad. Sci. Paris* **1880**, *91*, 294-297.

(135) Sauerbrey, G. *Z. Phys.* **1959**, *155*, 206-22.

(136) Höök, F.; Kasemo, B.; Nylander, T.; Fant, C.; Sott, K.; Elwing, H. *Analytical chemistry* **2001**, *73*, 5796-5804.

(137) Craig, V. S.; Plunkett, M. *Journal of Colloid and Interface Science* **2003**, *262*, 126-129.

(138) Rodahl, M.; Hook, F.; Krozer, A.; Brzezinski, P.; Kasemo, B. *Rev. Sci. Instrum.* **1995**, *66*, 3924-30.

(139) Voinova, M. V.; Rodahl, M.; Jonson, M.; Kasemo, B. *Phys. Scr.* **1999**, *59*, 391-396.

(140) Bottom, V. E. *Introduction to Quartz Crystal Unit Design*; Van Nostrand Reinhold Co.: New York, 1982.

(141) Petit-Agnely, F.; Iliopoulos, I.; Zana R. *Langmuir* **2000**, *16*, 9921-9927.

(142) Browning, N. D.; Chisholm, M. F.; Pennycook, S. J. *Nature* **1993**, *366*, 143- 146.

(143) Wang, Z. L. *J. Phys. Chem. B* **2000,** *104*, 1153–1175.

(144) Rouzes, C.; Gref, R.; Leonard, M.; De Sousa Delgado, A.; Dellacherie, E. *Journal of Biomedical Materials Research Part A* **2000**, *50*, 557-565.

(145) Tompkins, H. G.; McGahan, W. A. *Spectroscopic ellipsometry and reflectometry: A user's guide,* John Wiley & Sons, Inc., New York, 1999.

(146) Tompkins, H. G.; Irene, E. A. Eds, *Handbook of ellipsometry,* William Andrew, New York, 2005.

(147) Tsankov, D.; Hinrichs, K.; Korte, E. H.; Dietel, R.; Roseler, A. *Langmuir* **2002,** *18,* 6559-6564.

(148) Cresswell J. P. *Langmuir* **1994**, *10,* 3727-3729.

(149) Nagy, N.; Deak, A.; Horvolgyi, Z.; Fried, M.; Agod, A.; Barsony, I. *Langmuir* **2006**, *22,* 8416-8423.

(150) Paudler, M.; Ruths, J.; Riegler, H. *Langmuir* **1992**, *8*, 184-189.

(151) Hecht, E. *Optics,* Addison Wesley, San Francisco, 2002.

(152) Born, M.; Wolf, E. *Principles of optics,* Cambridge University Press, Cambridge, 1999.

(153) Karabiyik, U.; Mao, M.; Roman, M.; Jaworek, T.; Wegner, G.; Esker A. R. *ACS Symposium Series* **2009**, *1019*, 137-155.

(154) Ni, S.; Yin, W.; Ferguson-McPherson, M. K.; Satija, S. K.; Morris, J. R.; Esker, A. R. *Langmuir* **2006**, *22*, 5969-5973.

(155) Fiegland L. R.; Saint Fleur, M. M.; Morris, J. R. *Langmuir* **2005**, *21*, 2660–2661.

(156) Panayotov D. A.; Morris, J. R. *J. Phys. Chem. C* **2009**, *113*, 15684–15691.

(157) Greenler, R. G. *J. Chem. Phys.* **1969**, *50*, 1963-1968.

(158) Greenler, R. G. *J. Chem. Phys.* **1966**, *44*, 310-315.

CHAPTER 3

Materials and Experimental Techniques

3.1 Materials

11-amino-1-undecanethiol for an amine-terminated self-assembled monolayer (SAM-NH_2) on gold surface was purchased from Asemblon. Cinnamic acid, 98% and N, N'-carbonyl diimidazole, 98% (CDI) were purchased from Alfa Aesar. Pullulan was purchased from Sigma. 1,2-Dioleoyl-sn-glycero-3-phosphocholine (DOPC), cholesterol and 1-oleoyl-2-hydroxy-sn-glycero-3-phosphocholine (LysoPC) in chloroform were purchased from Avanti Polar Lipids (Alabaster, AL). Their chemical structures are provided in Figure 3.1. Ultrapure water (Millipore, Milli-Q Gradient A-10, 18.2 MΩ, < 5 ppb organic impurities) was used in all experiments. Dimethyl sulfoxide, spectrophotometric grade, 99.9+% (DMSO) was purchased from Alfa Aesar. N, N-dimethylacetamide, 99% (DMAc), pyrene, 99% and tetrahydrofuran, 99% (THF) were purchased from Sigma. N, N-Dimethyl formamide, 99.9% (DMF) was purchased from Fischer Scientific and distilled under reduced pressure with anhydrous magnesium sulfate as a drying agent. Ethanol and methanol 99% were purchased from Decon Lab, Inc. Dry formamide was purchased from Riedel-de Haën. Acetic anhydride, 99% was purchased from Fluka. H_2O_2 (30% by volume), HCl, H_2SO_4, and NH_4OH (28% by volume) were purchased from EM Science, VWR International, and Fisher Scientific, respectively. Chromium, gold and a deposition crucible were obtained from International Advanced Materials. Physical vapor deposition onto float glass was achieved by an electron beam evaporator system (Thermionic Vacuum Products, Inc.). Quartz crystals with a 50 nm thick SiO_2 layer on top of a gold electrode (fundamental resonant frequency of 5 MHz and a diameter of 14 mm) were purchased from Q-Sense AB.

Silicon wafers (100) were obtained from Waferworld, Inc. Mica substrates and carbon-coated copper grids for transmission electron microscopy were purchased from SPI Supplies. Epo-tek 377 was from Epoxy Technology Inc. Syringes were obtained from Henke-Sass, Wolf.

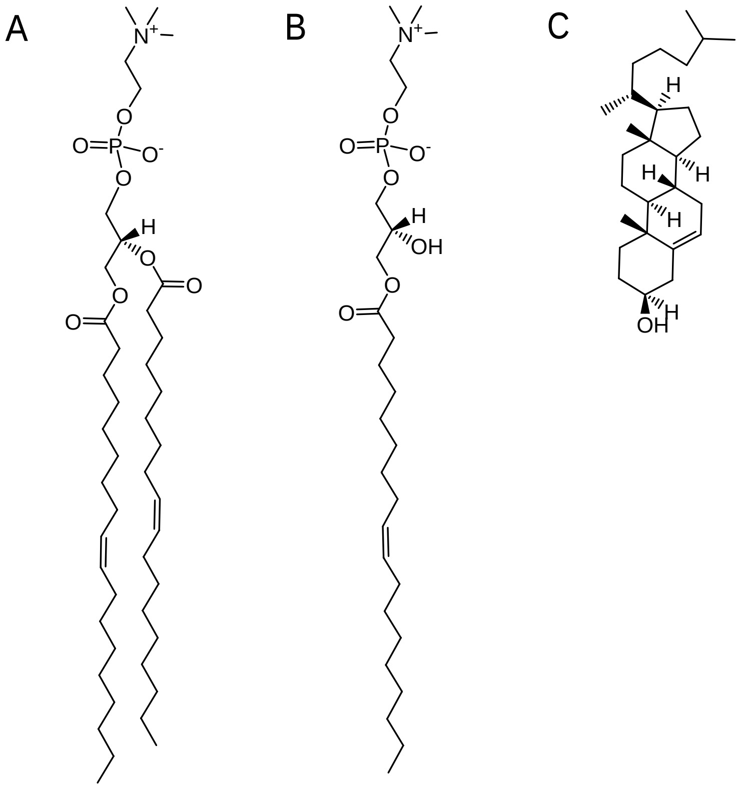

Figure 3.1 Structures of (A) DOPC, (B) LysoPC and (C) cholesterol. DOPC forms bilayer vesicles with an aqueous cavity in aqueous media, whereas single-tailed LysoPC aggregate into micelles in water.

3.1.1 Synthesis of Pullulan Cinnamates (PC). Pullulan cinnamates were prepared by grafting cinnamic acid onto the backbones of pullulan (Figure 3.2). The carbonyl group of cinnamic acid was first activated by CDI in anhydrous DMF at room temperature for 24 hours. The intermediate product imidazole carbamate was transferred to the reaction flask containing pullulan dissolved in DMAc. The reaction continued for 24 hours at 70 °C. The final product was precipitated in 99% ethanol and dried under vacuum at 40 °C for 24 hours. The degree of substitution value (DS) was defined as the number of cinnamate groups per anhydroglucose unit (AGU). Three DS levels, 0.03, 0.06 and 0.08, were prepared. More details about the synthesis and characterization by NMR or UV-Vis spectroscopy were reported previously.[1]

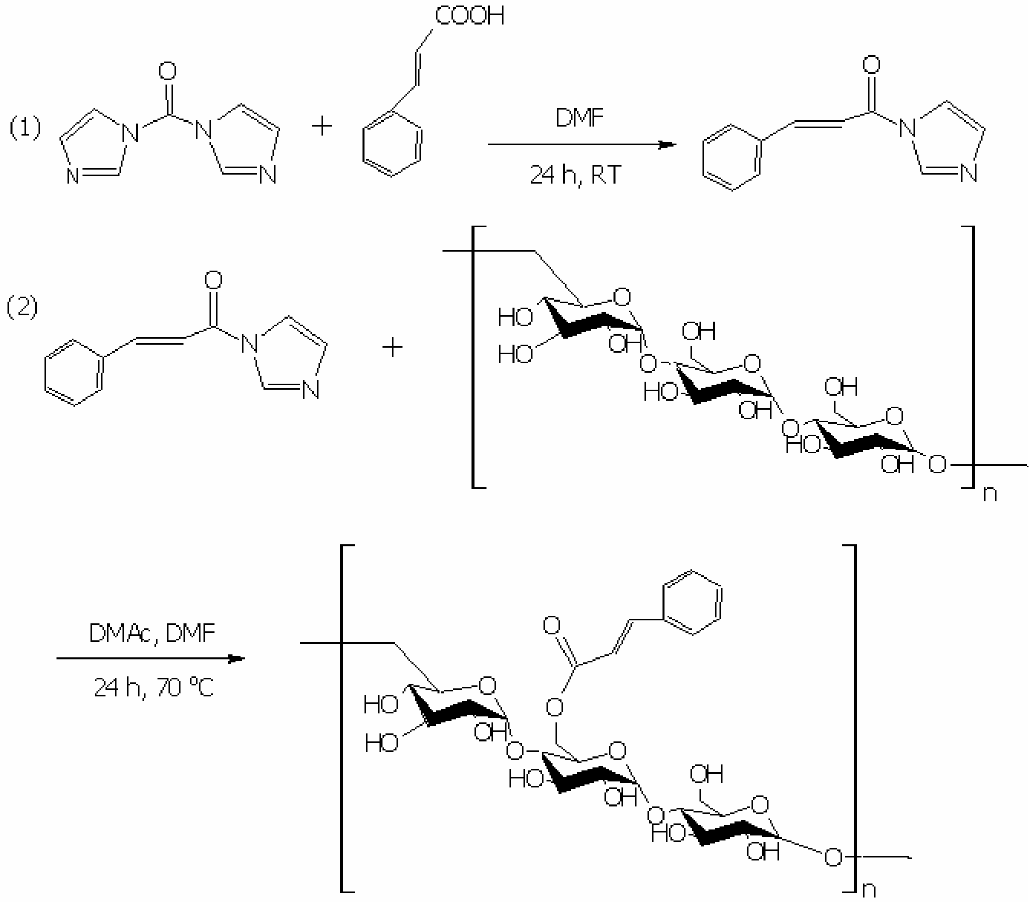

Figure 3.2 Synthetic route for pullulan cinnamates.

3.1.2 Aggregation of PC by Pyrene Dye Fluorescence Spectroscopy. Since the pyrene molecule was preferentially soluble in hydrophobic aggregates relative to hydrophilic environments, the aggregation of pullulan derivatives could be investigated by fluorescence spectroscopy (Perkin-Elmer LS 50 Spectrometer) with the fluorescent pyrene probe.[2] Aliquots of pyrene in methanol were initially transferred into empty vials until the methanol evaporated. Next, test solutions of known concentration were added to the vials. All of the mixtures were shaken mildly on an Orbit Shaker for at least 24 h. The resulting solutions contained 10^{-6} M pyrene. Emission fluorescence spectra of pyrene were recorded with an excitation wavelength of 334 nm, an excitation bandpass of 5 nm, and an emission bandpass of 2.5 nm. Since the ratios of the emission intensities of the first (I_1 = 373 nm) and third (I_3 = 384 nm) vibronic peaks in the emission spectra were sensitive to the polarity of the pyrene microenvironment, they were employed to detect the aggregation behavior of pullulan and PCs in aqueous media. As seen in Figure 3.3, the fact that variation in the intensity ratio stretches over 2 orders of magnitude in concentration indicates that the aggregation was less cooperative than typical surfactant micelles. The beginning and end points of the variation shifts toward lower concentrations for higher DS (more hydrophobic) PC.

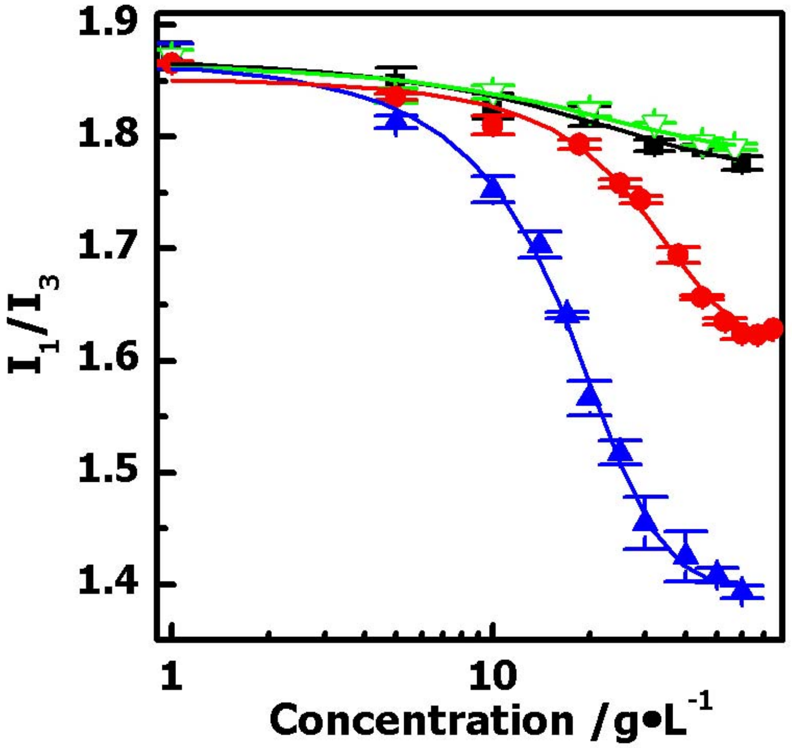

Figure 3.3 Variation of I_1/I_3 in response to concentration for pullulan and PCs in aqueous media. Symbols correspond to (▽) pullulan, (■) PC DS=0.03, (●) PC DS=0.06, and (▲) PC DS=0.08 with one standard deviation error bars. The solid lines represent fits with a sigmoidal function.

3.1.3 Synthesis of Cellulose Samples. Cellulose nanocrystals were prepared according to the previous method.[3,4] The reaction was carried out by dissolving milled softwood sulfite pulp (Temalfa 93A-A from Tembec, Inc.) in sulfuric acid (500 mL, 64 wt%) at 45 °C for 60 min. It was terminated by dilution of the reaction mixture with cold water. The sulfuric acid was removed from the cellulose suspension by three-round centrifugation (Thermo IEC Centra-GP8R refrigerated centrifuge, Thermo Fisher Scientific Inc.) at 4900 rpm for 15 minutes. The product was transferred to Spectra/Por 4 dialysis tubing (Spectrum Lab, Inc.) and dialyzed against water until the pH was constant. The final suspension, was sonicated (VC 505 500 W ultrasonic processor, Sonics & Materials, Inc.) to separate cellulose aggregates and filtered through a 0.45 µm poly(vinylidene fluoride) (PVDF) syringe filter (Whatman, Ltd.). To remove the sulfate groups on the surfaces of cellulose nanocrystals, the H_2SO_4-hydrolyzed cellulose suspension (1.14 wt%) was neutralized with pyridine and lyophilized (Freezone 4.5L freeze dry system, Labconco Corp.).[5] The freeze-dried product was dissolved in DMSO and methanol. The reaction continued for 2 h at 80 °C which was terminated by addition of cold water. The suspension was transferred to dialysis tubing and dialyzed against water. The final product was filtered through a 0.45 µm PVDF syringe filter.

Trimethylsilyl cellulose (TMSC, DS = 2.71) was synthesized by Prof. Thomas Heinze's group at the University of Jena (Jena, Germany).[6,7] Cellulose was first dissolved in DMAc at 70 °C. The TMS groups were grafted onto the cellulose chains by reaction with hexamethyldisilazane for 24 h at 100 °C with TMS-Cl as the catalyst. THF was added to dissolve the product. Methanol was used to precipitate and purify the final product. The final TMSC isolated as a powder was dried in a vacuum oven at 60 °C prior to use.

3.2 Preparation of Substrates. The 1 × 1 cm^2 sensor slides for surface plasmon resonance were prepared by the deposition of 20 Å chromium and 480 Å gold onto float glass at 3×10^{-6} Torr with an electron beam evaporator system (Thermionic Vacuum Products, Inc.). The gold-coated glass sensor slides were first cleaned by immersion in a piranha solution (H_2O_2:H_2SO_4 = 3:7 by volume) for 1 hour, rinsed exhaustively with ultrapure water and dried with nitrogen gas. To prepare model cellulose films for QCM-D measurements, the quartz crystals were first cleaned by piranha solution, rinsed with ultrapure water and dried with nitrogen gas. Then the quartz crystals were exposed to UV/Ozone ProCleaner™ (Bioforce Nanoscience, Inc.) for 20 minutes. A second cleaning by piranha solution followed. Template stripped gold surfaces were prepared for AFM imaging.[8] Gold films, 100 nm thick were first evaporated onto freshly cleaved mica surfaces at a rate of 1 $Å·s^{-1}$. The 1 × 1 cm^2 silica substrates were cleaned by boiling in a 1:1:5 (by volume) solution of $NH_4OH:H_2O_2:H_2O$ for 1.5 h. After the substrates were rinsed with ultrapure water and dried with nitrogen, they were immersed in piranha solution for 3 h, rinsed with ultrapure water, and dried with nitrogen. Silicon wafers were then glued to the gold-deposited mica sheets by Epo-tek 377. The epoxy glue was cured at 150° C for two hours. Prior to use, the gold surface was detached from the mica substrate.

3.3 Preparation of Cellulose Films on Substrates. Uniform regenerated cellulose (RC) films were prepared by spincoating TMSC onto the cleaned sensor slides with a spinning speed of 4000 revolutions per minute (rpm) from 10 $g·L^{-1}$ TMSC solutions in toluene. Trimethylsilyl groups of TMSC were cleaved by exposure of the sensor slides to 10 wt% hydrochloric acid vapor for 2 minutes. For the preparation of fully covered nanocrystalline cellulose (NC) films on gold surfaces, a well-ordered SAM-NH_2 layer was formed on the slide by placing a cleaned sensor slide into a 1 mM ethanol solution for at least 24 hours. The SAM slide was removed from the 11-amino-1-undecanethiol solution, rinsed with absolute ethanol and dried with nitrogen. Finally, the SAM sensor slide was washed with ultrapure water and dried with nitrogen. NC films were spincoated onto SAM-NH_2 surfaces with a spinning speed of 4000 rpm from 10 $g·L^{-1}$ cellulose nanocrystal suspensions. The same spincoating parameters used for the SPR sensors were used to prepare model cellulose surfaces on QCM-D quartz slides and gold substrates for AFM imaging. Figure 3.4 shows representative AFM images of cellulose surfaces in aqueous media where smooth features and rod-like nanocrystals were observed for RC and NC surfaces, respectively.

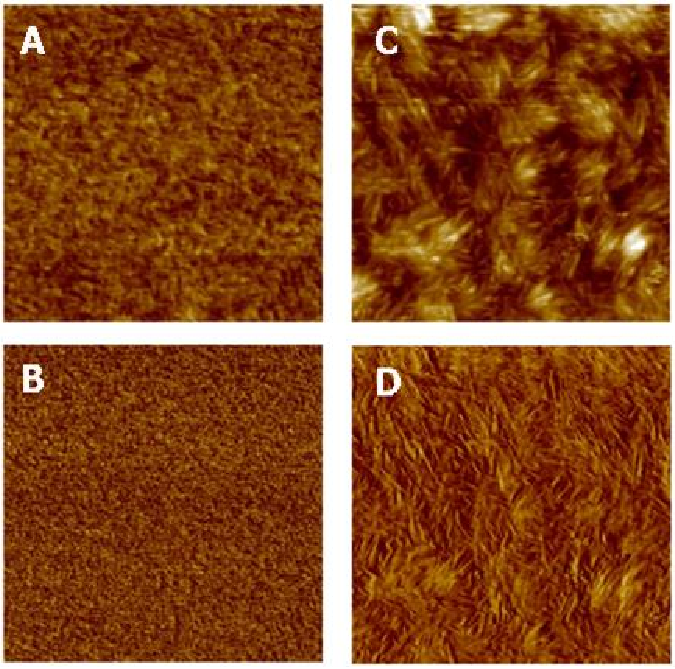

Figure 3.4 Representative AFM images of cellulose surfaces. (A) Height and (B) phase images of RC surfaces, height and phase scales are 0 to 20 nm and 0 to 5 degree, respectively. (C) Height and (D) phase images of NC surfaces, height and phase scales are 0 to 40 nm and 0 to 10 degree, respectively. The AFM images are 2 × 2 μm^2.

3.4 Characterization Techniques

3.4.1 Wide Angle X-ray Diffraction. X-ray diffraction patterns were obtained on a Bruker D8 Discover diffractometer (Bruker AXS, Inc.). Cu Kα radiation (λ = 1.54 Å) generated at 30 mA and 40 kV was used as the radiation source. The angular scanning range was $2\Theta = 7°$ to 50° with 0.01° steps. Free-standing NC films were generated by air drying 10 mL aliquots of a 10 $g \cdot L^{-1}$ cellulose suspension in Petri dishes at 50 °C. The crystalline index was obtained from: $CI_{XR}=1-$

(I_{am}/I_{cr}), where I_{cr} was the intensity from the (002) plane at $2\Theta = 22.4°$, and I_{am} was the background intensity at $2\Theta = 18.5°$ which represented amorphous material.[9]

3.4.2 Transmission Electron Microscopy (TEM). A Philips EM 420 electron microscope equipped with a CCD camera operating at 100 kV was used to obtain the morphology of pullulan in aqueous midea. 0.5 ml polysaccharide solution with a carbon-coated copper grid was placed inside a microcentrifuge tube. The top of the tube was sealed by parafilm pierced with holes. The microcentrifuge tube was partially submerged in liquid nitrogen and quickly freezed. The frozen tube was then moved to a round-bottom flask connecting to the lyophilizer. The freeze drying process continues for at least 24 h. Figure 3.5 shows TEM images of pullulan in water where the polysaccharides formed spherical aggregates.

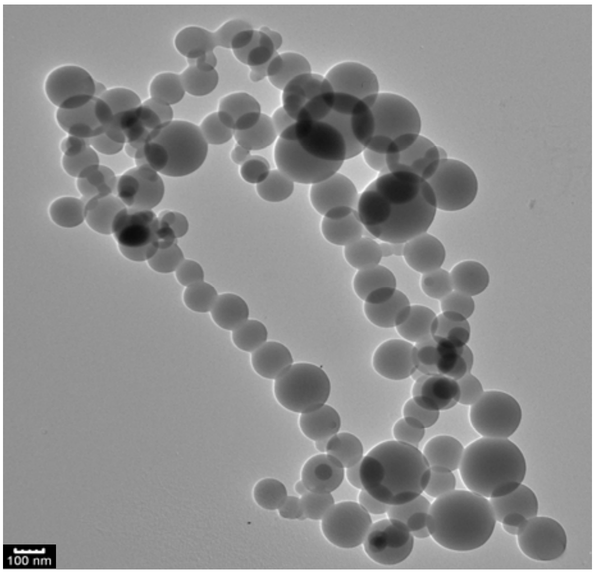

Figure 3.5 Pullulan aggregates prepared from aqueous media by TEM. The scale bar corresponds to 100 nm.

The amorphous structures of RC films were investigated by electron diffraction in the TEM. TMSC was first deposited onto the TEM grid from an 1 g·L^{-1} TMSC solution in toluene. Cellulose was regenerated by exposure of the grid to the vapor of an aqueous 10 wt% HCl solution for 2 minutes. After the film was dried with nitrogen, the sample on the grid was transferred to the vacuum chamber of the electron microscope. The electron beam was first focused on interesting areas of sample film. The electron diffraction pattern was obtained by switching the real space observation to phase space diffraction.

3.4.3 X-ray Photoelectron Spectroscopy (XPS). X-ray photoelectron spectra were measured with a Perkin-Elmer system (PHI 5400, Perkin-Elmer, Mg-Kα radiation) using a magnesium anode operated at 250 W with a background pressure of 5×10^{-7} Torr. The spectra were recorded with an 89.45 eV pass energy, 0.1 eV step and 25 ms dwelling time. The angle between the X-ray beam and surface normal was 15°. Each surface was examined from 0 to 1100 eV where the relative elemental compositions were estimated from a multiplex spectrum of carbon, oxygen, silicon, and gold.

3.4.4 Reflection Absorption Infrared Spectroscopy (RAIRS). RAIRS spectra of cellulose films were obtained by a Nicolet Nexus 670 FTIR Spectrometer under vacuum. The liquid-nitrogen cooled mercury−cadmium−telluride detector was employed to avoid the icing effect from water vapor ~ 3300 cm^{-1}.[10] 100 scans with a resolution of 2 cm^{-1} were collected and averaged using *p*-polarized light at an incident angle of 86°. Freshly cleaned gold substrates were taken as background references.

3.4.5 Film Thickness Measurements by Ellipsometry. Multiple angle of incidence ellipsometry measurements were carried out with a phase modulated ellipsometer (Picometer Ellipsometer, Beaglehole Instruments, Wellington, New Zealand) at a wavelength of 632.8 nm (He-Ne laser). Since the sensitivity for layer thickness was the greatest around the Brewster angle (~74°),[11] the datapoints were collected from 65 to 80° with 1.0° steps. If not noted, measurements were made at 3 spots and reported results represented the average with one standard deviation error bars. The film thickness was calculated in TFCompanion software where multilayer modeling of experimental data is possible.

3.4.6 Surface Plasmon Resonance (SPR) Spectroscopy. The sensor slides were refractive index matched to the prism (n = 1.51) of a SPR refractometer (Reichert SR 700, Inc.) by an immersion oil. The SPR system used a laser diode with an emission wavelength of 780 nm. The flow cell with a gasket was mounted on top of the exposed surfaces (NC or RC). Degassed solutions were pumped into the flow cell at a flow rate of 0.25 $mL\cdot min^{-1}$ by a cartridge pump (Masterflex). Water was flowed over the exposed surfaces until a stable baseline was established. Sample solutions were pumped into the flow cell until adsorption plateaued, followed by another cycle of water flushing. Each experiment was carried out at least three times to obtain average values with one standard deviation error bars.

The surface plasmon resonance occurred at a critical incident angle where a minimum in the reflected intensity can be observed.[12] Therefore, the change in the resonance angle ($\Delta\theta_{sp}$) was a measure of the refractive index change of the ambient medium (Δn_a). Figure 3.6 shows how $\Delta\theta_{sp}$ varied from pure solvent, to adsorbed polymer, to irreversibly adsorbed polymer flushing. The surface excess of adsorbed materials on the exposed surfaces (Γ) was calculated through the equation of de Feijter, *et al.*: [13]

$$\Gamma = \frac{L \bullet \Delta n_a}{dn / dc} = \frac{\Delta\theta_a \bullet \Delta n_a}{(d\theta / dL)(dn / dc)} \qquad (3.1)$$

where L is the thickness of the adsorbed layer, dn/dc is the refractive index increment of the adsorbed material, and Δn_a is the refractive index change of the ambient medium during the adsorption process. ($d\theta/dL$) values for RC, NC and SAM-NH_2 surfaces were $(4.2 \pm 0.2) \times 10^{-3}$, $(4.3 \pm 0.2) \times 10^{-3}$ and $(4.0 \pm 0.2) \times 10^{-3}$ deg•$Å^{-1}$, respectively. The $\Delta\theta_a$ can be expressed as:

$$\Delta\theta_a = \Delta\theta_{tot} - c\left(\frac{d\theta_{sp}}{dn}\right)\left(\frac{dn}{dc}\right) \qquad (3.2)$$

where ($d\theta_{sp}/dn$) is the instrument parameter of the SPR instrument (61.5 °) and (dn/dc) is the refractive index increment of the adsorbate in solution.

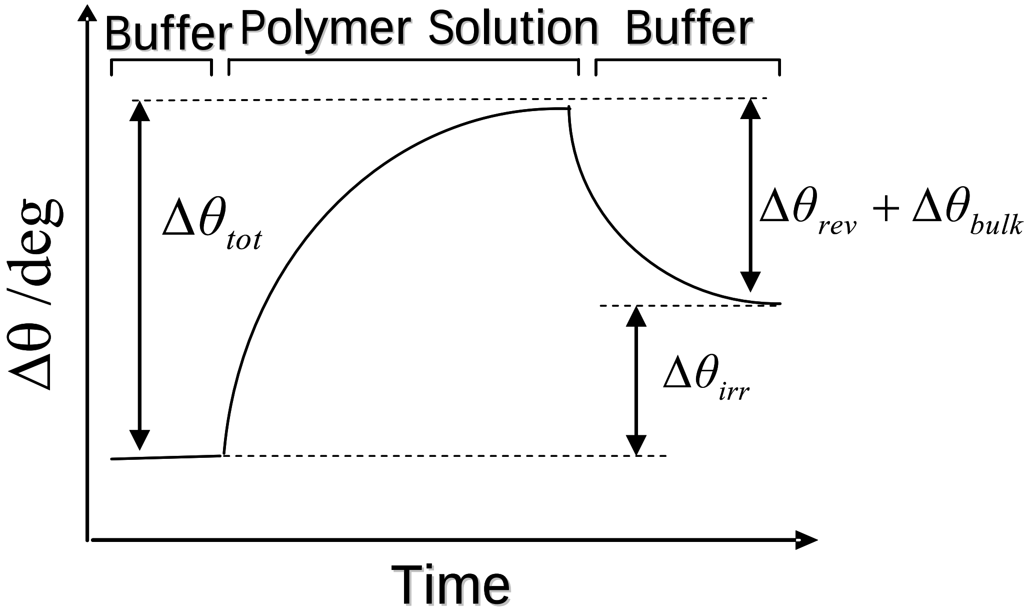

Figure 3.6 Schematic description of the change in SPR resonance angle during the adsorption process where pure buffer was used to establish a baseline value. The polymer solution led to a total change in resonance angle ($\Delta\theta_{tot}$). After flushing with buffer to remove the bulk contribution ($\Delta\theta_{bulk}$) and reversibly adsorbed materials ($\Delta\theta_{rev}$), $\Delta\theta_{irr}$ corresponded to the contribution of irreversibly bound material.

3.4.7 Quartz Crystal Microbalance with Dissipation (QCM-D) Monitoring Measurements.

The acoustic mass, comprised of water and adsorbed material, for modified cellulose films were measured by QCM-D (Q-Sense E4). The quartz crystals were mounted in a fluid cell with the cellulose-coated side exposed to the solution. Solvent was pumped over the quartz crystal at the same rate as SPR experiments (0.25 $mL\cdot min^{-1}$) by a cartridge pump (ISMTE-ISM935). Frequency and dissipation changes for the fundamental frequency and six odd overtones (n = 3 to 13) were monitored simultaneously. Once the baseline was stabilized, sample solutions containing adsorbates were flowed onto the exposed surfaces. Then pure solvent was pumped into the module again to wash away reversibly bound materials. Each experiment was carried out at least three times to obtain average values with one standard deviation. For the case of rigid surfaces with small dissipation changes ($\Delta D < 2 \times 10^{-6}$), the adsorbed mass ($\Delta m$) can be calculated from the frequency change (Δf) through the Sauerbrey equation:[14]

$$\Delta m = -C \times \frac{\Delta f}{n} \qquad (3.3)$$

where C is the sensitivity constant (17.7 $\text{ng} \cdot \text{cm}^{-2} \cdot \text{Hz}^{-1}$ for the QCM sensor slides with f = 5 MHz) and n is the overtone number. However, for the soft layers with high viscosities and dissipation values, theoretical fitting based on a Voigt-based viscoelastic model[15] should be employed to study the physical properties of adsorbed materials. Under the assumption that the adsorbed layer is surrounded by a semi-infinite Newtonian fluid, the QCM-D curves of frequency and dissipation changes are fit by the Q-tools software from Q-Sense AB. The high overtone orders (n=5, 7 and 9) were used for estimation while low overtones such as n=1 and 3 were neglected because of insufficient energy trapping.[16] The acoustic mass including coupled water and adsorbed material can be deduced from the product of effective density and thickness of the adsorbed layer.

3.4.8 *In situ* Atomic Force Microscopy (AFM) Measurements. The samples were imaged in tapping mode on a Nanoscope III AFM at room temperature (Dimension 3000 scope with a Nanoscope IIIa controller, Digital Instruments, set point of ca. 0.6). AFM images are reported without any image processing except flattening. Cantilevers were exposed to ultraviolet irradiation for at least 0.5 h prior to use. The silicon nitride tips mounted into the fluid cell, had a nominal radius of 20 nm and a spring constant of 0.58 $\text{N} \bullet \text{m}^{-1}$. The fluid cell was attached to the exposed surface by a gasket. Pure solvent was flowed over the model surface by a syringe pump

(KDS 200, KD Scientific Inc.) at the same rate (0.25 mL·min^{-1}) and orders as SPR and QCM-D experiments. Images of the substrates at liquid/solid interfaces were taken after flowing solvent over the surface for one hour to allow for equilibrium swelling. Then the sample solution was injected into the fluid cell and was subsequently flushed with pure solvent flushing for at least 30 minutes. Post-adsorption images were taken at the same position in the liquid/solid interface for comparisons of the surface prior to and after adsorption.

3.5 References:

(1) Kaya, A.; Du, X.; Liu, Z.; Lu, J. W.; Morris, J. R.; Glasser, W. G.; Heinze, T.; Esker, A. R. *Biomacromolecules* **2009,** *10*, 2451-2459.

(2) Nichifor, M.; Lopes, S.; Bastos, M.; Lopes, A. *Journal of Physical Chemistry B* **2004**, *108*, 16463-16472.

(3) Edgar, C. D.; Gray, D. G. *Cellulose* **2003**, *10*, 299-306.

(4) Beck-Candanedo, S.; Roman, M.; Gray, D. G. *Biomacromolecules* **2005**, *6*, 1048-1054.

(5) Jiang, F.; Esker, A. R.; Roman, M. *Langmuir* **2010**, *26*, 17919–17925.

(6) Schaub, M.; Wenz, G.; Wegner, G.; Stein, A.; Klemm, D. *Adv. Mater.* **1993**, *5*, 919-922.

(7) Buchholz, V.; Wegner, G.; Stemme, S.; Ödberg, L. *Adv. Mater.* **1996**, *8*, 399-402.

(8) Wagner, P.; Hegner, M.; Guentherodt, H.-J.; Semenza, G. *Langmuir* **1995**, *11*, 867-3875.

(9) Mwaikambo, Y.; Ansell, M. P. *Die Angewandte Makromolekulare Chemie* **1999**, *272*, 108-116.

(10) Ni, S.; Yin, W.; Ferguson-McPherson, M. K.; Satija, S. K.; Morris, J. R.; Esker, A. R. *Langmuir* **2006**, *22*, 5969-5973.

(11) Fu, Z.; Santore, M. M. *Colloid Surface A* **1998**, *135*, 63-75.

(12) Green, R. J.; Frazier, R. A.; Shakesheff, K. M.; Davies, M. C.; Roberts, C. J.; Tendler, S. J. B. *Biomaterials* **2000**, *21*, 1823-1835.

(13) De Feijter, J. A.; Benjamins, J.; Veer, F. A. *Biopolymers* **1978,** *17*, 1759-1772.

(14) Sauerbrey, G. *Z. Phys.* **1959**, *155*, 206-22.

(15) Voinova, M. V.; Rodahl, M.; Jonson, M.; Kasemo, B. *Phys. Scr.* **1999**, *59*, 391-396.

(16) Bottom, V. E. *Introduction to Quartz Crystal Unit Design*; Van Nostrand Reinhold Co.: New York, 1982.

CHAPTER 4

Pullulan Cinnamate Adsorption onto Nanocrystalline Cellulose Films

4.1 Abstract

Surface plasmon resonance and *in situ* atomic force microscopy were used to study pullulan cinnamate (PC) adsorption onto nanocrystalline cellulose (NC) films. Smooth cellulose I films were spin coated from cellulose nanocrystal suspensions onto a cationic anchor of an amine-terminated alkanethiol self-assembled monolayer on gold (SAM-NH_2). The elemental composition of carbon vs. oxygen and the absence of elemental gold in the X-ray photoelectron spectra of the NC films indicated that the cellulose nanocrystals completely covered the underlying surface. Infrared spectra and X-ray diffraction patterns further confirmed the higher degree of crystallinity of the NC films relative to regenerated cellulose (RC) films. For pullulan and PC with low degrees of substitution (DS), the mass of the adsorbed polysaccharides was on the order of a flat polysaccharide monolayer and did not significantly change the surface morphology of the NC film. The interactions between PCs with higher DS and porous NC films presumably generated looped PC structures with surface concentrations at least a factor of two greater on thick NC films than on RC films. Several possible causes, including surface charge, the underlying SAM-NH_2 and crystalline degrees of cellulose films, were considered. However, it was found that the porous features of the NC films were responsible for the greater adsorption relative to RC films from studies of surface excess (Γ) versus film thickness (d). Plots of Γ vs. d for high DS PC showed linear regimes at small d, a cross-over point at intermediate d, and plateaus at high d. Experiments revealed that cinnamate group DS had a tremendous impact on the slope of the linear portion of the film, cross-over point, and plateau value. The fact that

extrapolated intercepts of Γ to d = 0 for NC coincided with values for nonporous RC was interpreted as a top layer which was similar for NC and amorphous RC. The "larger Γ" for NC films arose from partial penetration of PC into the inner layers of the porous cellulose films rather than thicker PC layers at the surface. This study of molecular interactions between PC and cellulose surfaces with natural cellulose I crystal structures sheds light on the affinity of lignin-carbonhydrate-complexes for cellulose.

4.2 Introduction

Natural materials, a combination of both organic and inorganic components, have superior physicochemical properties and bio-compatibility relative to comparable synthetic materials. For example, the complex structure of the secondary plant cell wall has a hierarchy of cellulose microfibrils and hemicelluloses that is believed to arise from self-assembly.[1,2] It was suggested that cellulosic and lignin-carbohydrate fibers could serve as reinforcing components in fiber-thermoplastic materials. To improve the compatibility of cellulose fibers with thermoplastics, the adsorption of polysaccharide derivatives onto cellulose surfaces were adopted to improve the adhesion and bonding at polymer-fiber interface.[3,4] Meanwhile, chemically modified polysaccharides, such as pullulan modified with photo-crosslinkable cinnamoyl groups, can be used to mimic the lignin-carbohydrate complex in cell wall biogenesis.[5,6] Through the study of PC adsorption onto cellulose surfaces, it might clarify the self-assembly of different components (cellulose, hemicellulose and lignin) in plant cell wall structures and inform future work aimed at the next generation of biomimetic nanocomposites.[7]

Model cellulose films have been frequently employed for the investigation of interactions between polymers and enzymes in wood-based system.[8] The first ultra thin cellulose films were regenerated from Langmuir-Blodgett films of trimethylsilyl cellulose,[9,10] whereas smooth films of cellulose I were prepared from cellulose nanocrystal suspensions.[11,12] Later, Ahola *et al.* prepared a new kind of cellulose surface composed of both crystalline and amorphous cellulose I regions from cellulose nanofibril dispersions that was closer to the native state of cellulose.[13] Inelastic neutron scattering showed the dynamic response of hydroxyl groups in various cellulose samples to water was affected by the degree of crystallinity. Sharp excitations were found in neutron time-of-flight difference spectra for crystalline cellulose, while broad peaks with little structure were found in less ordered regions.[14] Cellulose model films with different degrees of crystalline ordering also affected enzyme adsorption onto the surfaces and their subsequent hydrolysis.[15] Likewise, Eriksson *et al.*[16] showed surface adhesion hysteresis between loading and unloading cycles depended upon the degree of crystalline order between cellulose surfaces and polydimethylsiloxane. Furthermore, the swelling properties of cellulose films were affected by both crystalline ordering and the mesoscale structure of the films.[17]

In previous studies from our group, it was found that PC adsorption onto RC surfaces increased with increasing DS of cinnamate groups.[6] The resulting adsorbed PC films had smooth features in AFM images and small surface roughnesses. Cellulase adsorption onto RC films was independent of film thickness, whereas adsorption onto NC films increased with film thickness.[18] The enhanced adsorption onto NC films was consistent with greater access to the interior of NC films for guest molecules, like water and cellulases. In this chapter, effects of different physical properties, like polymorphs, crystallinity, and charge density on PC adsorption are examined. Previously reported investigations[6] of PC adsorption onto RC surfaces by SPR are compared with investigations of PC adsorption onto NC surfaces. Morphological differences at the mesoscopic scale between the two cellulose surfaces strongly affected PC adsorption.

4.3 Experimental

11-amino-1-undecanethiol for an amine-terminated alkanethiol self-assembled monolayers on gold (SAM-NH_2) was purchased from Asemblon. Cinnamic acid, 98% and N, N'-carbonyl diimidazole, 98% were purchased from Alfa Aesar. Pullulan was purchased from Sigma. Procedures for the PC synthesis, preparation of RC and NC films, film thickness measurement by multiple-angle-of-incidence ellipsometry, film characterization by reflection absorption infrared spectroscopy (RAIRS) and X-ray photoelectron spectroscopy (XPS), X-ray diffraction (XRD), electron diffraction, SPR measurements, solvent exchange measurements by QCM-D and *in situ* AFM imaging were described in Chapter 3.1.1, 3.3, and 3.4, respectively. In this chapter, P, PC003, PC006, PC008 correspond to pullulan (P) and pullulan cinnamates (PCs) with DS = 0.03, 0.06, and 0.08, respectively.

4.4 Results and Discussion

4.4.1 Film Preparation and Characterization

Fully covered NC films, were prepared by spincoating anionic cellulose nanocrystals (prepared by the hydrolysis of spruce pulp in 64 wt% H_2SO_4 [11,12]) onto cationic SAM-NH_2 surfaces. The well-ordered SAM on the gold surface was confirmed by RAIRS.[19] The asymmetric (2924 cm^{-1}) and symmetric (2854 cm^{-1}) stretching modes of the methylene groups along the backbone of the alkane chains indicated that the SAMs were densely packed (Figure 4.1). X-ray photoelectron spectra were used to determine the surface chemical composition of NC films spin-coated onto SAM-NH_2 surfaces in Figure 4.2. The experimental C:O ratio (57:43) was in agreement with the theoretical elemental composition of cellulose (C:O=6:5). The absence of gold from the substrate in the spectrum indicated that the SAM surface was well covered by cellulose nanocrystals. Ellipsometry studies of the prepared NC surfaces yielded an average film thickness of 14.9 ± 0.3 nm.

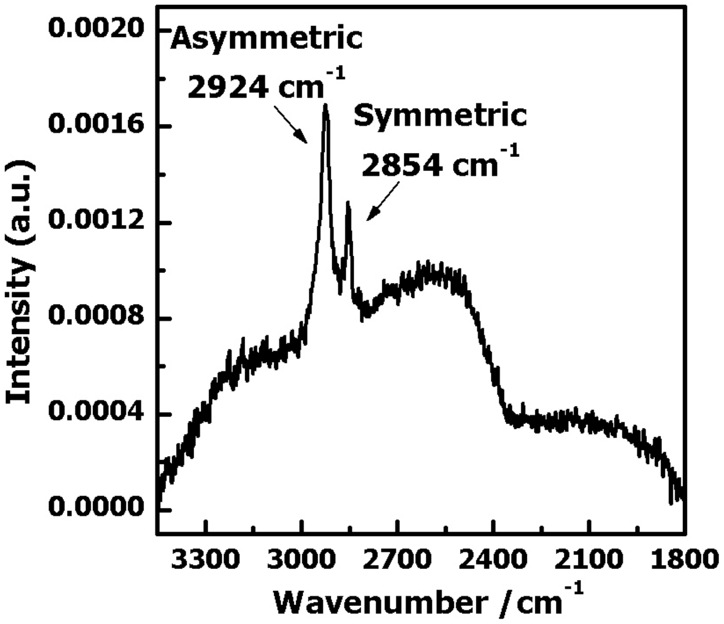

Figure 4.1. A representative RAIRS spectrum highlighting the asymmetric and symmetric C-H stretching region for SAM-NH_2.

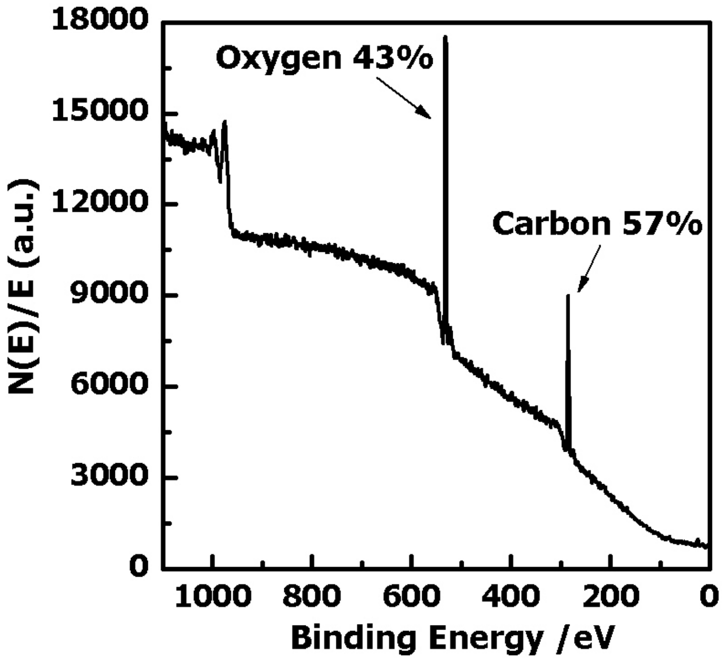

Figure 4.2. A representative X-ray photoelectron spectrum of NC spincoated onto the SAM-NH_2 surface. Percentage values indicate atomic percentages.

The fine structure of the NC surfaces was further characterized by RAIRS (Figure 4.3). The intramolecular hydrogen bonds for 2-OH···O-6 and 3-OH···O-5, and the intermolecular hydrogen bonds for 6-OH···O-3' in NC appeared at 3411, 3362, and 3309 cm^{-1}, respectively, which indicated an ordered structure existed, i.e., a high degree of crystallinity. In comparison with RC surfaces,[6] the absorption band at about 1430 cm^{-1}, assigned to the CH_2 scissoring motion, became more intense in NC films while the band at about 895 cm^{-1}, assigned as C–O–C stretching at the β-(1-4)-glycosidic linkage, became very weak due to the greater crystalline character. Additionally, sharper lineshapes were observed for the NC surfaces below 3000 cm^{-1} relative to regenerated cellulose surfaces. The intensity ratio of the absorbance at 1430 cm^{-1} to that at 895 cm^{-1} (I_{1430}/I_{895}) was used for a relative crystallinity index (CI_{IR}).[20] NC surfaces gave a CI_{IR} of 8.3 versus 1.8 for RC surfaces. X-ray diffraction analysis of cellulose nanocrystals clearly indicated the (002) crystalline plane in Figure 4.4, whereas the electron diffraction pattern of RC films exhibited no features characteristic of crystalline structures. The circular halo in Figure 4.5 indicated the RC samples were mostly unoriented and amorphous. All of these observations are consistent with NC samples having a greater degree of order (crystallinity) than RC.

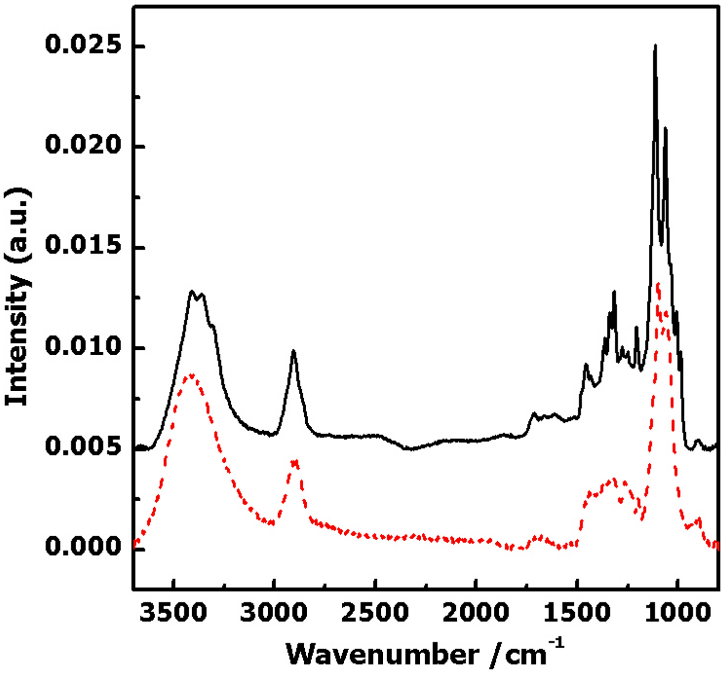

Figure 4.3. RAIRS spectra of a NC (dark solid line) and RC (red dashed line) films. Spectral assignments were provided in the text and Table 4.1.

Table 4.1. Spectral assignments for NC and RC films.[21,22]

NC surfaces*		RC surfaces	
Wavenumber (cm^{-1})[a]	Interpretation	Wavenumber (cm^{-1})[a]	Interpretation
3411 (s)	2-OH···O-6	3421 (s, br)	O-H stretching
3362 (s)	3-OH···O-5		
3309 (s)	6-OH···O-3'		
2907 (m)	C-H stretching	2892 (m)	C-H stretching
1470 (m)	C-H deformation	1458 (m)	C-H deformation
1432 (m)	CH$_2$ scissoring	1429 (m)	CH$_2$ scissoring
1362 (m)	C-H bending	1362 (m)	C-H bending
1317 (m)	CH$_2$ wagging	1313 (m)	CH$_2$ wagging
1206 (m)	C-O-H in-plane deformation	1194 (m)	C-O-H in-plane deformation
1113 (vs)	Ring asymmetric stretching	1094 (vs)	Ring asymmetric stretching
1060 (s)	C-O valence vibration	1056 (s, br)	C-O valence vibration
1037 (s)			
986 (m)			
897 (w)	C-O-C ring stretching	895 (m)	C-O-C ring stretching

[a] vs = very strong, s = strong, m = medium, w = weak, and br = broad

*Absorbance peaks for NC are relatively stronger and sharper than RC.

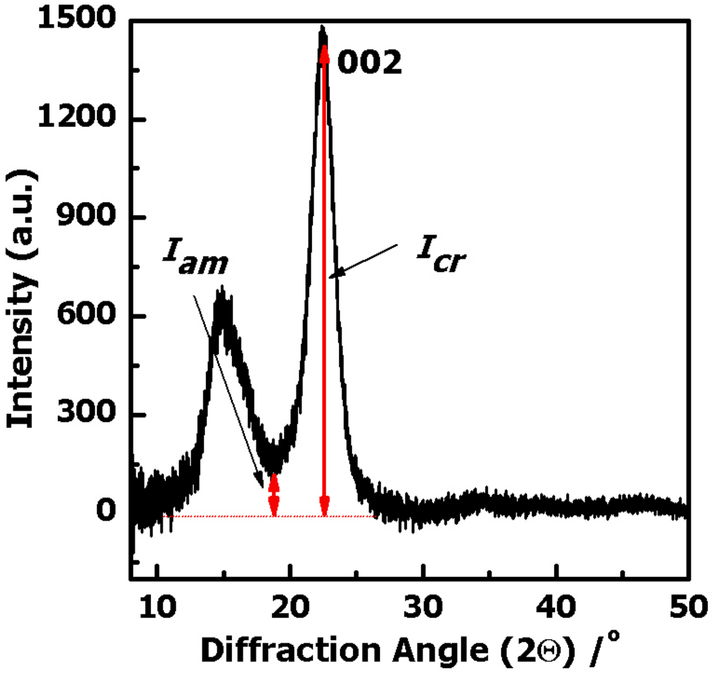

Figure 4.4. A representative wide angle X-ray diffraction pattern for a NC film. $CI_{XR} = 1-(I_{am}/I_{cr}) = 0.88$ using the method of Mwaikambo *et al.*[23]

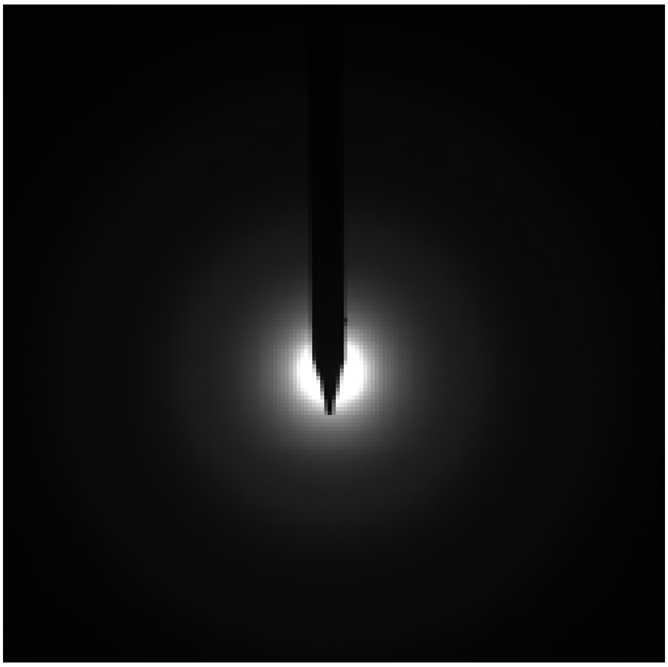

Figure 4.5. The electron diffraction pattern of RC films by transmission electron microscopy.

4.4.2 Adsorption onto Model Surfaces

Representative raw SPR data for the adsorption of pullulan and PCs with different DS onto NC surfaces are provided in Figure 4.6. Each experiment was carried out as least twice to obtain $\Delta\theta_{max}$ values for each concentration from SPR curves. Analysis of angle change followed the same procedure reported for PC adsorption onto regenerated cellulose.[6] Surface concentrations (Γ), for each bulk solution concentration were calculated through the equation of de Feijter *et al.* (Chapter 3.4.6)[24] and these values were plotted in Figure 4.7 as a function of the bulk solution concentration. There was no significant adsorption of P onto NC surfaces. Slight increases for DS ~ 0.03 PC (PC003) adsorption onto NC films were observed, while DS ~ 0.06 and DS ~ 0.08 PC (PC006 and PC008, respectively) adsorbed strongly onto NC films from aqueous solution. The results indicated that irreversible adsorption of high DS PCs was consistent with a hydrophobically driven process.

The PC adsorption isotherms for NC films were fit with a Langmuir model[25] (Figure 4.7 and Table 4.2) which is suitable for adsorption as a monolayer on homogeneous surfaces:

$$\Gamma = \frac{\Gamma_m \bullet K_L \bullet C}{1 + K_L \bullet C} \qquad (4.1)$$

where C is the bulk concentration of the adsorbates, Γ_m is the maximum adsorbed amount, K_L is the Langmuir constant or the equilibrium constant (the ratio of the adsorption rate constant and desorption rate constant). It was found that Γ_m systematically increased with increasing cinnamate DS and the trend reflected the hydrophobic character of the higher DS PCs. It is interesting to note the value of a flat polysaccharide monolayer adsorbed onto a substrate where Γ_m = 0.45 mg·m^{-2} and the thicknesses h_m = 5.4 Å.[26] Pullulan and PC003 adsorbed onto NC surfaces in an amount that was on the order of submonolayer ($\Gamma_m = 0.12 \pm 0.01$ mg•m^{-2}) to monolayer coverage ($\Gamma_m = 0.53 \pm 0.05$ mg•m^{-2}), whereas PC006 and PC008 layers adsorbed onto NC surfaces were thicker and on the order of ~5 ($\Gamma_m = 2.1 \pm 0.2$ mg•m^{-2}) and ~16 ($\Gamma_m = 7.7 \pm 0.3$ mg•m^{-2}) "monolayers". The affinity strength was also inferred from estimated K_L of the PCs as K_L of PC008 (0.021 ± 0.001 L•mg^{-1}) was 4-5 times greater than that of the lower DS PCs (0.004 ± 0.001 L•mg^{-1} for PC003 and 0.005 ± 0.001 L•mg^{-1} for PC006). Recently reported Langmuir fits of PC adsorption onto RC films[6] were also summarized in Table 4.2 for reference. As seen from the values in Table 4.2, adsorption onto NC surfaces was a factor of two or greater than adsorption onto RC for most DS.

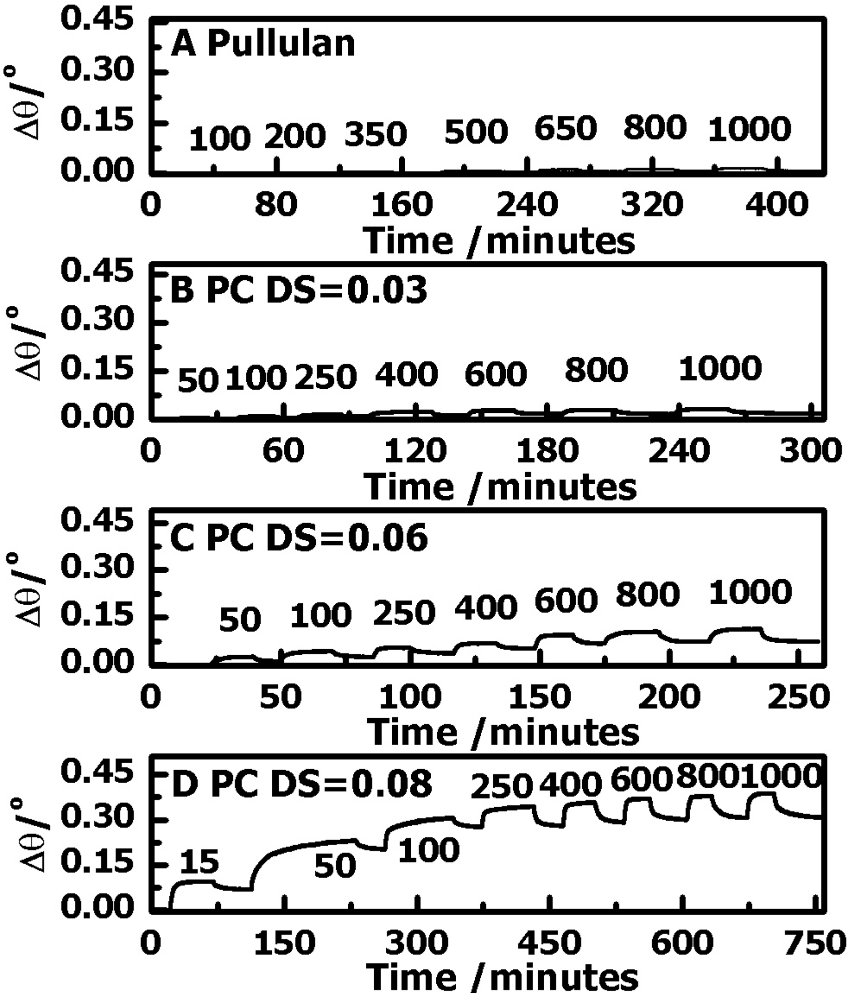

Figure 4.6. Representative SPR data for P and PC adsorption onto NC films at 20.0 °C. Graph (A) through (D) correspond to P, PC003, PC006, and PC008, respectively. Solution concentrations in units of mg·L^{-1} correspond to the numbers on (A) through (D). Water was flowed through the SPR instrument prior to and after each new adsorbate solution. Analysis of these curves followed the same procedure detailed elsewhere for RC.[6]

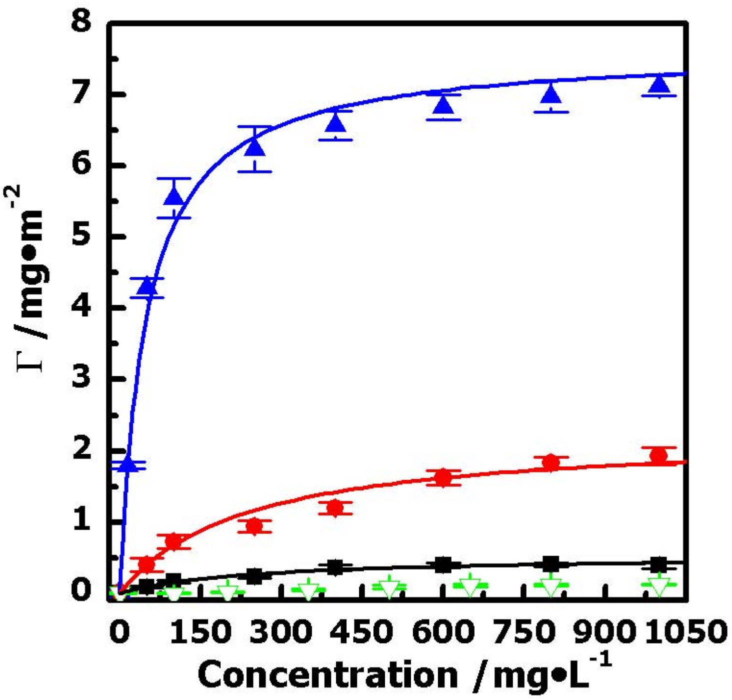

Figure 4.7. Adsorption isotherms for P and PC adsorption onto NC films at 20.0 °C. Symbols correspond to (▽) P, (■) PC003, (●) PC006, and (▲) PC008 with one standard deviation error bars. The solid lines represent fits with Langmuir isotherms.

Table 4.2. Isotherm parameters for P and PC adsorption onto NC and RC surfaces.

Adsorbate	NC surfaces [a]			RC surfaces [b]		
	Γ_m (mg•m^{-2}) [c]	h_m (Å) [c]	K_L (L•mg^{-1}) [d]	Γ_m (mg•m^{-2}) [c]	h_m (Å) [c]	K_L (L•mg^{-1}) [d]
P	0.12±0.01	1.5±0.1	—	0.06±0.03	0.8±0.4	—
DS=0.03	0.53±0.05	6.3±0.6	0.004±0.001	0.27±0.03	3.2±0.4	0.015±0.002
DS=0.06	2.1±0.2	26±3	0.005±0.001	1.4±0.1	17±1	0.009±0.001
DS=0.08	7.7±0.3	92±3	0.021±0.001	3.1±0.3	37±3	0.011±0.001

[a] The NC film were14.9 ± 0.3 nm thick. [b] From Ref. [6]. [c] From analysis of SPR data following Ref. [24]. The refractive index of all films was assumed to be 1.45. [d] From a fit with Eq. 4.1.

4.4.3 AFM Studies of P and PC Adsorption onto NC Surfaces

Representative *in situ* AFM images of the solid/liquid interface for NC surfaces prior to adsorption and the same surfaces after exposure to P and PC solutions for 2 hours and a subsequent one hour rinse with water are provided in Figure 4.8. The height images for the NC films contained cylindrical crystalline elements which were clearly visible prior to adsorption. The rod-like cellulose nanocrystals had a length between 100 and 150 nm with a width ~ 10 nm. The apparent width of cellulose nanocrystals is larger than previously published results[12] because of tip broadening that arose from an AFM tip with a curvature comparable to the size of the sample.[27] For the case of P and PC003 adsorption onto the NC surfaces (Figure 4.8 A-D), there were almost no changes of the surface morphologies. Pullulan and PC003 adsorption only led to a slight increase of the root-mean-sqaure (RMS) surface roughness from 2.5 and 2.6 nm to 2.9 and 3.0 nm, respectively. These observations were consistent with submonolayer to monolayer surface coverages deduced from the SPR measurements. Significant adsorption of the higher DS PC derivatives onto the NC surfaces resulted in substantial changes of surface topologies and roughnesses as seen in Figure 4.8 E-H. Uniform coverage of the NC surfaces by the adsorbed PC006 film masked the rodlike patterns of the underlying nanocrystals. Even thicker, presumably looped, PC aggregates were observed on the NC surfaces after PC008 adsorption. The RMS surface roughness increased from 2.4 to 3.2 nm and 2.4 to 4.7 nm after PC006 and PC008 adsorption, respectively.

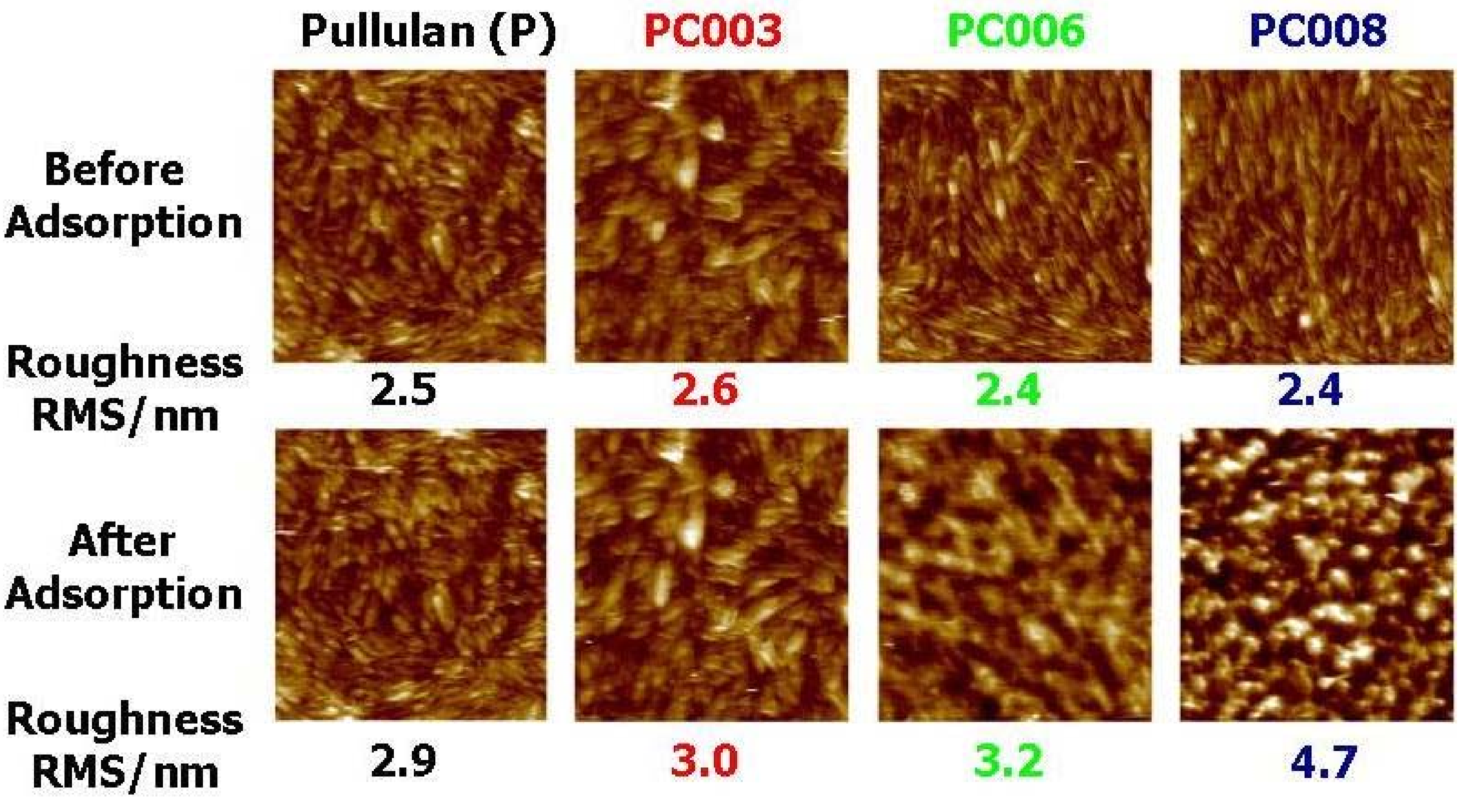

Figure 4.8. Representative AFM height images of the solid/liquid interface of nanocrystalline cellulose surfaces prior to and after P and PC adsorption from a bulk solution (1 g·L^{-1}). The AFM images are 2 µm x 2 µm and have Z-axis scales of 0 to 40 nm. Numbers under each picture indicate RMS roughnesses.

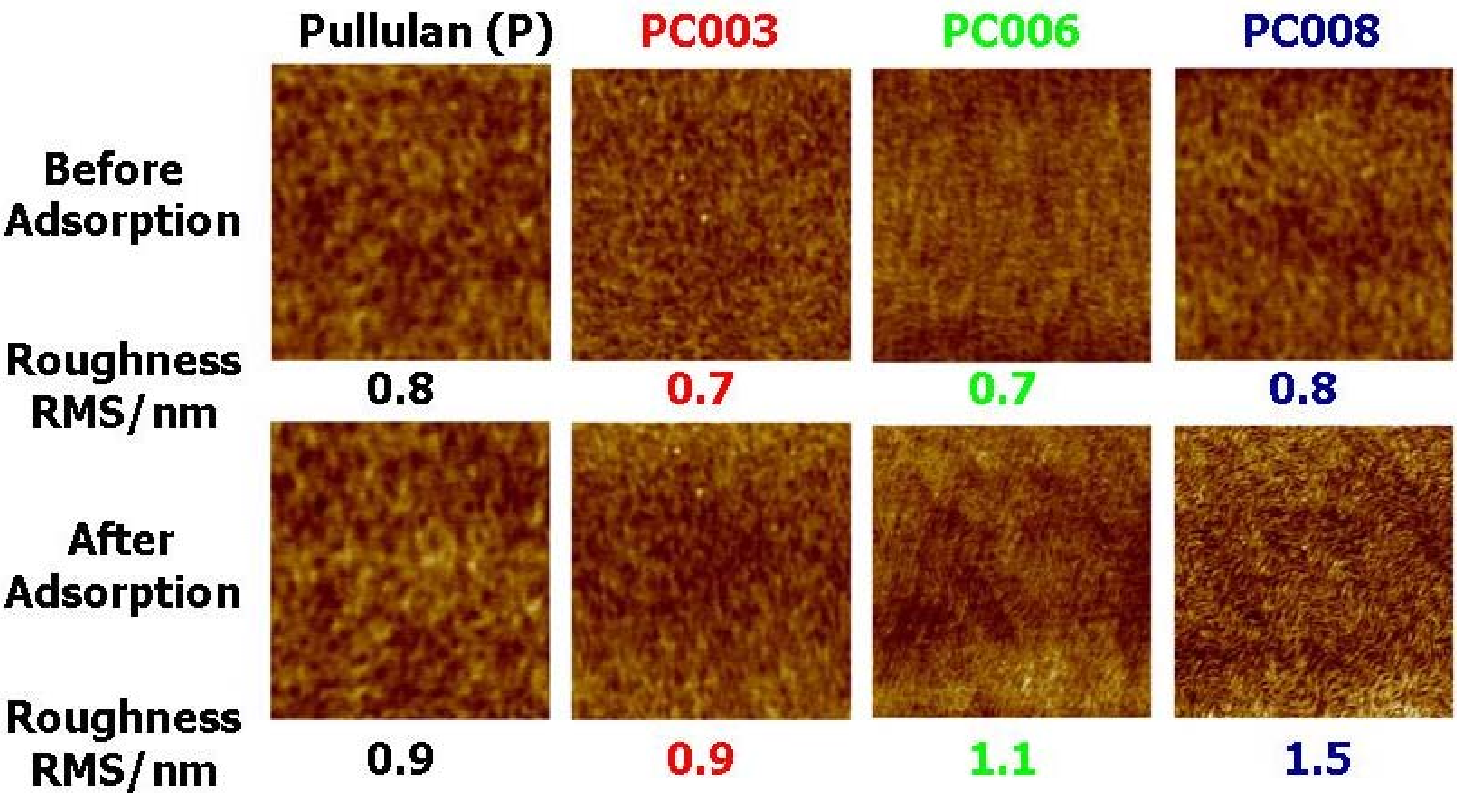

Figure 4.9. Representative AFM height images of the solid/liquid interface of regenerated cellulose surfaces prior to and after P and PC adsorption from a bulk solution (1 g·L^{-1}). The AFM images are 2 μm x 2 μm and have Z-axis scales of 0 to 20 nm. Numbers under each picture indicate RMS roughnesses.

AFM images of the solid/liquid interface for RC surfaces before and after P and PC adsorption are presented in Figure 4.9 as a reference.[6] The uniform coverage of RC surfaces by high DS PC were confirmed by the small surface roughness increase (< 1 nm). Insignificant adsorption of P and low DS PCs onto cellulose surfaces resulted in negligible morphological and RMS roughness change. Compared with the SPR data, all these observations indicated that polymer adsorption was limited to the top of the densely packed RC film without any significant penetration of the PCs into the interior of the film.

4.4.4 Mechanisms of PC Adsorption onto NC Surfaces

Several possible causes for the larger observed adsorption of PCs onto NC than RC surfaces were considered. First, effects of charged sulfate groups on the surface of cellulose nanocrystals were considered. On average, ~ 3% of the anhydroglucose units (AGU) contained one sulfate ester for cellulose nanocrystals prepared from softwood sulfite pulp in sulfuric acid at 45 °C. These sulfate groups can be removed by pyridine treatment which led to < 0.07% substitution degree of the AGUs by sulfate groups.[28] Figures 4.10 shows representative raw SPR data for adsorption of P and PCs onto NC surfaces treated by pyridine. Each experiment was carried out as least twice to obtain $\Delta\theta_{max}$ values from SPR curves. Differences in the maximal resonance angle and corresponding adsorbed amount for P and PC adsorption onto NC surfaces with fewer sulfate groups were less than 15% (see Table 4.3). This observation indicated that charge-dipole interactions did not have a large effect on PC adsorption.

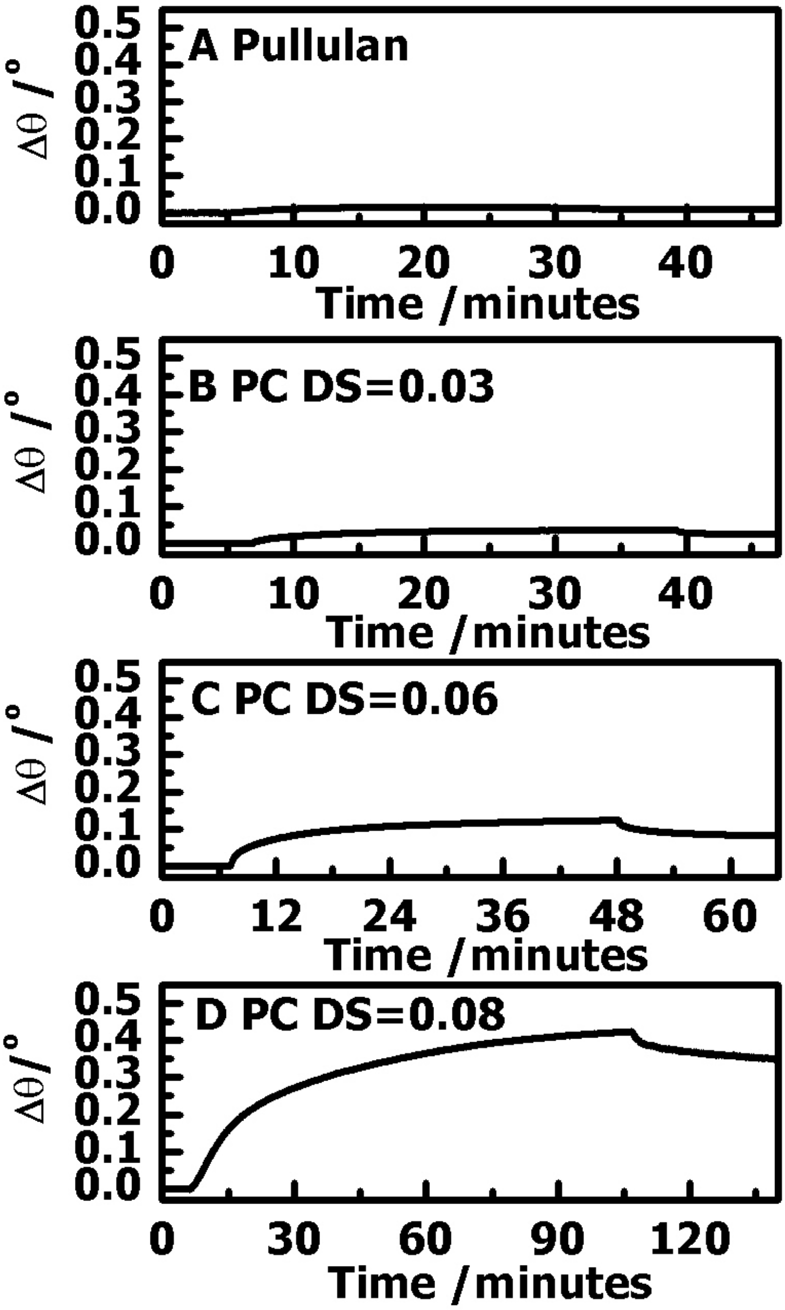

Figure 4.10. Representative SPR data for P and PC adsorption onto NC films which were pretreated by pyridine prior to spincoating. Graph (A) through (D) correspond to P, PC003, PC006, and PC008, respectively. Water was flowed through the SPR instrument prior to and after each new adsorbate solution. Analysis of these curves followed the same procedure detailed elsewhere for RC.[6]

Table 4.3. Maximum resonance angle change, surface excess and deduced film thickness for P and PC adsorbed onto NC samples pretreated by pyridine.

Adsorbates	$\Delta\theta_{max}$ (°)	Γ (mg•m^{-2}) [a]	h (Å) [a]
P	0.016±0.001	0.13±0.01	1.6±0.1
PC DS = 0.03	0.038±0.002	0.56±0.04	6.7±0.5
PC DS = 0.06	0.12±0.01	2.2±0.1	26±2
PC DS = 0.08	0.44±0.02	8.4±0.4	113±5

[a] From analysis of SPR data following Ref. [6]. The refractive index of all films was assumed to be 1.45.

Possible contributions of the SAM-NH_2 layer to the adsorption process were also probed. Results for P and PC adsorption onto SAM-NH_2 surfaces are provided in Figures 4.11 and 4.12 and Table 4.4. For the case of DS = 0.08 PC, Γ_m (4.2 ± 0.3 mg•m^{-2}) was only ~ 55% of the value observed for adsorption onto NC surfaces (7.7 ± 0.3 mg•m^{-2}). Pullulan and PCs with lower DS value also displayed less adsorption onto SAM-NH_2 than onto NC films. These results supported the fact that the high adsorption of P and PCs onto NC surfaces was caused by their intrinsic physical and chemical features. In comparison with a previous study,[6] it was noted that the general trend for PC adsorption onto SAM surfaces increased in the following order SAM-OH < SAM-NH_2 < SAM-CH_3 in line with the general order of attractive interactions between the adsorbate and SAM surfaces.[29] Corresponding AFM images and RMS roughnesses for SAM-NH_2 surfaces prior to and after pullulan and PC adsorption are provided in Figure 4.13. As seen in the height images, PC adsorption onto the SAM-NH_2 surfaces yielded smoother films with smaller features than PC films adsorbed onto NC surfaces.

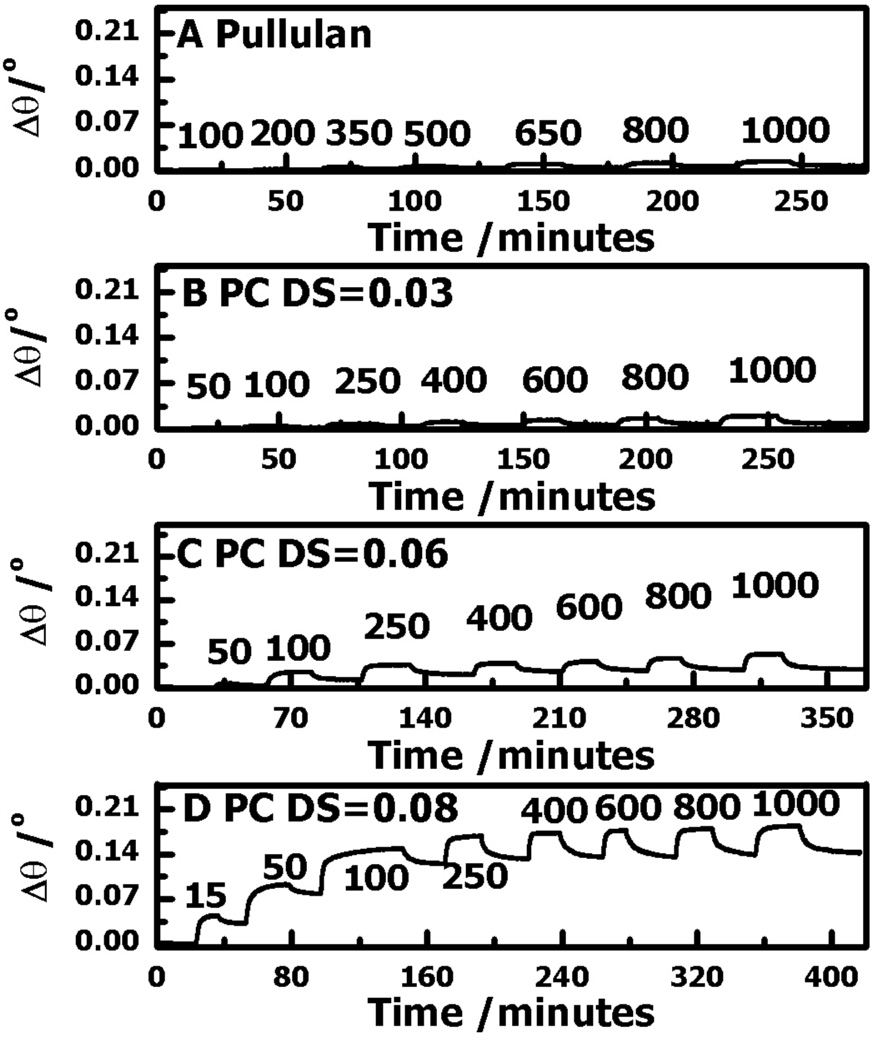

Figure 4.11. Representative SPR data for P and PC adsorption onto SAM-NH_2 films at 20.0 °C. Graphs (A) through (D) correspond to P, PC003, PC006, and PC008, respectively. Solution concentrations in units of mg·L^{-1} correspond to the numbers on (A) through (D). Water was flowed through the SPR instrument before and after each new adsorbate solution.

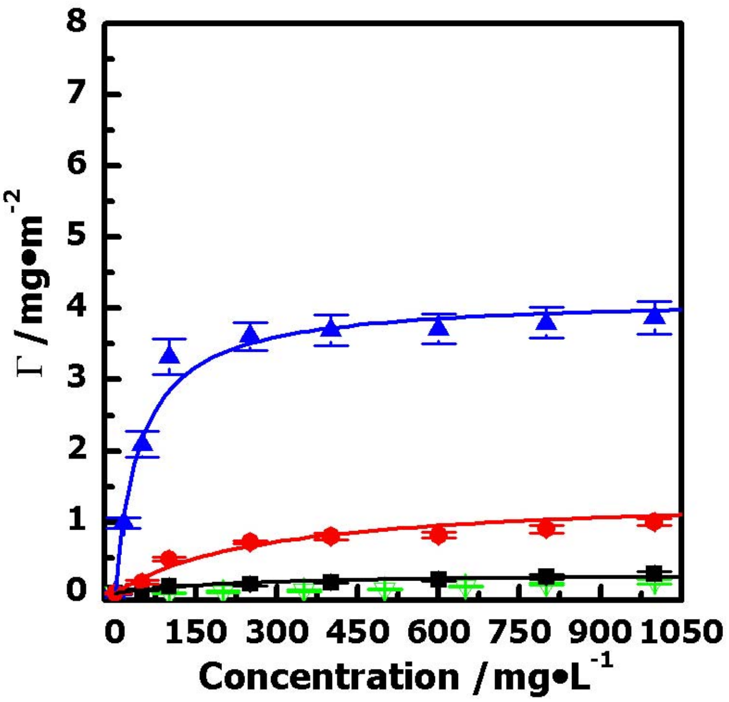

Figure 4.12. Adsorption isotherms for P and PC adsorption onto SAM-NH_2 at 20.0 °C. Symbols correspond to (▽) P, (■) PC003, (●) PC006, and (▲) PC008 with one standard deviation error bars. The solid lines represent fits with Langmuir isotherms. The y-axis range was chosen to match Figure 4.7 in order to highlight lower adsorption onto SAM-NH_2 surfaces relative to NC surfaces.

Table 4.4. Isotherm parameters for P and PC adsorption onto SAM-OH, SAM-NH_2, and SAM-CH_3 surfaces.

Adsorbate	SAM-OH [a]			SAM-NH_2			SAM-CH_3 [a]		
	Γ_m (mg•m^{-2}) [b]	h_m (Å) [b]	K_L (L•mg^{-1}) [c]	Γ_m (mg•m^{-2}) [b]	h_m (Å) [b]	K_L (L•mg^{-1}) [c]	Γ_m (mg•m^{-2}) [b]	h_m (Å) [b]	K_L (L•mg^{-1}) [c]
P	0.11±0.03	1.3±0.4	—	0.16±0.03	1.9±0.3	—	0.9±0.1	11±1	5±1
PC003	0.7±0.1	8±1	0.025±0.003	0.29±0.02	3.4±0.2	0.004±0.001	4.4±0.1	52±2	27±7
PC006	1.3±0.1	15±1	0.024±0.002	1.4±0.1	17±2	0.004±0.001	4.8±0.2	58±3	34±9
PC008	1.4±0.1	17±1	0.040±0.003	4.2±0.3	50±3	0.022±0.001	6.3±0.2	75±3	26±7

[a] From Ref. [12]. [b] From analysis of SPR data following Ref. [12]. The film refractive index was assumed to be 1.45. [c] From a fit to Eq. 4.1.

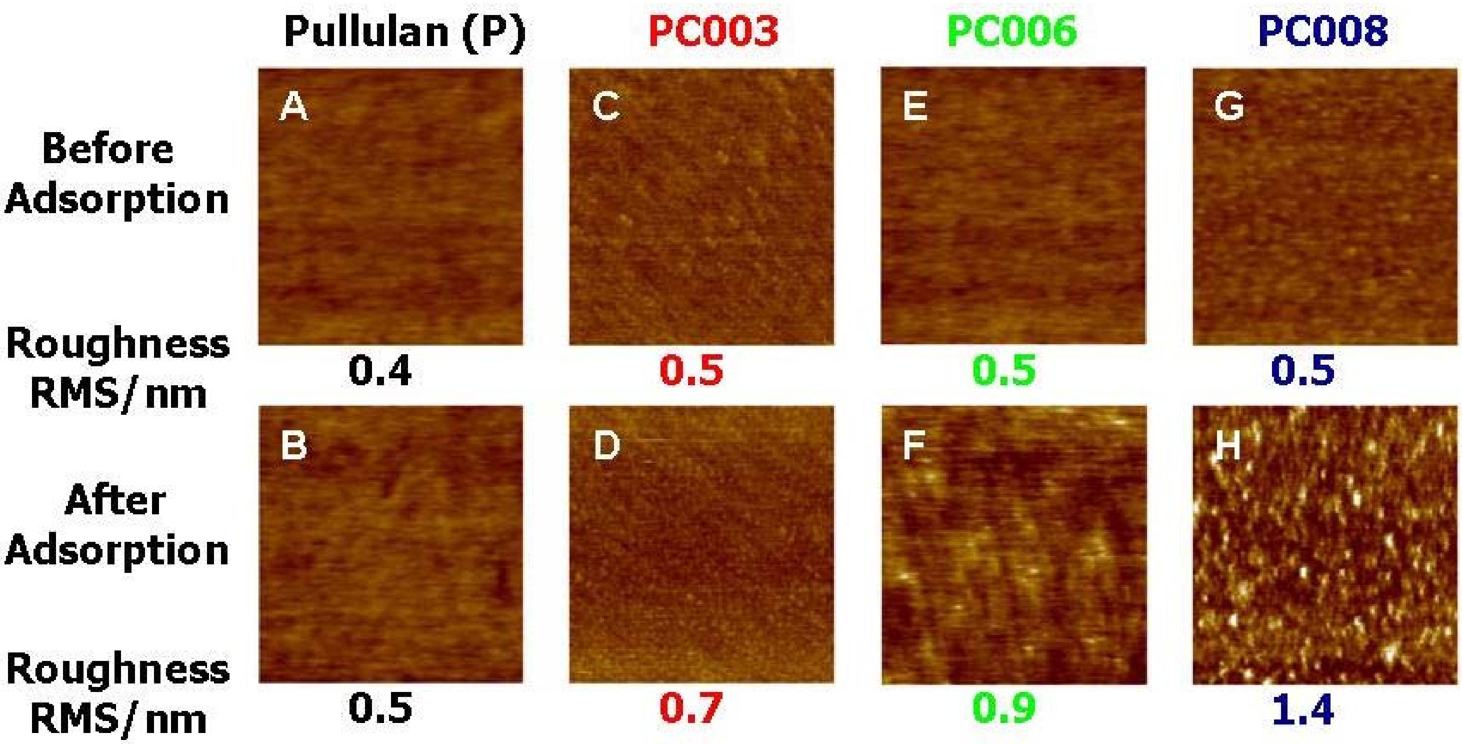

Figure 4.13. Representative AFM height images of the solid/liquid interface of SAM-NH_2 surfaces prior to and after P and PC adsorption from a bulk solution (1 g·L^{-1}). The AFM images are 2 μm x 2 μm and have Z-axis scales of 0 to 20 nm. The RMS surface roughnesses are indicated under each picture.

Last but not least, the NC films form three dimensional networks with greater available "surface area" for adsorption relative to RC films. As a consequence, these films should have absolute amounts of water that vary with film thickness. Recent work by Hook *et al.* and Craig *et al.* established a method to determine the solvent mass of a thin film via QCM-D measurements by deuterium exchange.[30,31] The adsorbed film was first measured in water followed by flowing deuterium oxide (D_2O) over the film. As D_2O replaced H_2O, the mass of the film increased. The frequency shift caused by the increased mass of the deuterium solvent can be calculated from

$$\left(\frac{\Delta f_{H20}}{n}\right) = \frac{\left(\frac{\Delta f_{H20}}{n}\right)}{\left(\frac{\rho_{D2O}}{\rho_{H2O}}\right) - 1} \qquad (2.14)$$

where Δf_{H20} and Δf_{D20} are the frequency differences between the bare surface in water and the adsorbed film in media for H_2O and D_2O, respectively, and ρ_{H20} and ρ_{D20} are the densities of H_2O and D_2O, respectively. Values of $(\Delta f_{H20}/n)$ could be converted into surface excess values through the Sauerbrey equation.[32] Figure 4.14 shows solvent exchange data for a bare gold sensor and a sensor coated with a RC film where a significant amount of water was present. The amount of water per monolayer of cellulose was further determined by using ellipsometry to determine the effective number of "cellulose layers". Results for different thicknesses of cellulose films and coupled water are shown in Table 4.5.[18] Note that the ratio of surface excess values for RC to water were roughly 4:3 by mass, indicating that approximately 6 water molecules were associated with each AGU, or about 2 water molecules per hydroxyl group of the AGU. Additionally, the ratio of cellulose to water for RC films was independent on thickness, suggesting the measured water content was accurate in the range of measured film thicknesses.

Meanwhile, NC films showed roughly five times the amount of water per unit mass of cellulose relative to RC films. As water could not penetrate the cellulose nanocrystals,[33,34] this data suggested that the NC films were highly porous. As shown in Figure 4.15, adsorbates like water molecules and polymer chains can potentially reach the inner layers of the nanocrystal networks, whereas only the top layers of the RC films were likely accessible to polymers.

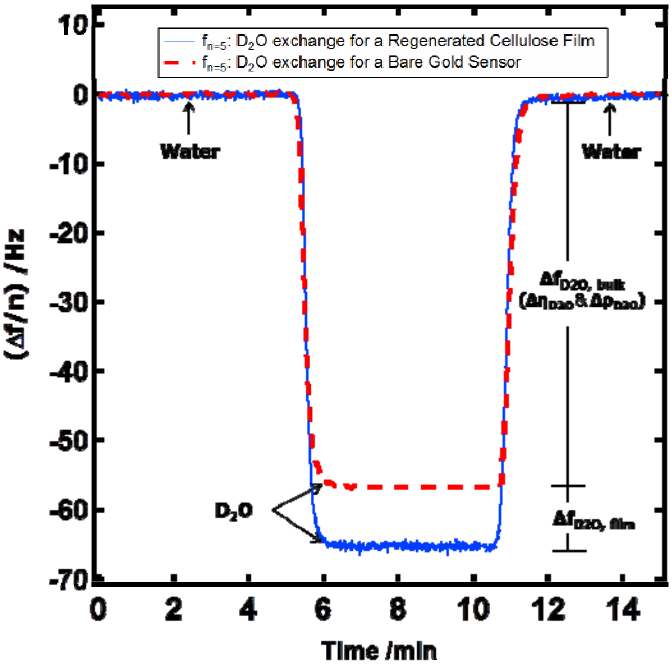

Figure 4.14. Solvent exchange data via QCM-D for a RC film. The difference between the frequency shift for a bare gold sensor and a sensor coated with the RC film during solvent exchange were used to calculate the water content of the cellulose film. The film thickness was 15.6 ± 1.6 nm.

Table 4.5. Water content of RC and NC films from solvent exchange. [a]

Cellulose	Film Thickness (nm)[b]	"Layers of Cellulose"	Γ_{H2O} (mg·m^{-2})	$\Gamma_{H2O/Layer}$ (mg·m^{-2}·layer^{-1})
RC	15.6 ± 1.6	43 ± 4	14 ± 2	0.32 ± 0.05
RC	44 ± 4	122 ± 10	35 ± 3	0.29 ± 0.04
NC	12.8 ± 0.4	36 ± 1	44 ± 3	1.2 ± 0.1
NC	18.2 ± 0.3	51 ± 1	67 ± 2	1.3 ± 0.1

[a] From Ref. [18].

[b] Determined via ellipsometry

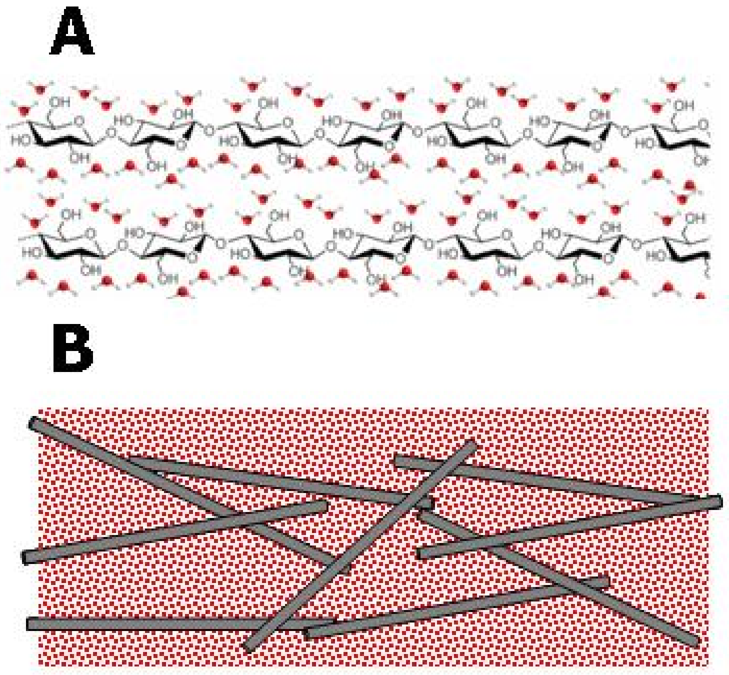

Figure 4.15. Schematic depiction of (A) RC and (B) NC films in aqueous media.[18]

To further probe the cause of greater adsorption onto NC films relative to RC films, measurements of pullulan and PC adsorption onto cellulose films with different thicknesses were carried out. Figures 4.16 and 4.17 show SPR data for 1 $g \cdot L^{-1}$ PC DS ~ 0.08 adsorption onto NC and RC films with film thicknesses varying from 4.5 nm to 15.3 nm. Each experiment was carried out as least twice. Surface excess (Γ) deduced from SPR experiments were plotted as a function of cellulose film thickness (d) in Figure 4.18. It was observed that Γ was proportional to film thickness up to d ~17 nm (sorption) after which the surface was saturated at ~ 7.3 $mg \cdot m^{-2}$ (combination of adsorption and sorption). This indicated the porosity of the NC films was fairly uniform while adsorption onto RC films was independent of film thickness (purely adsorption at the top of the film). A linear fit of PC008 onto NC films for d less than 17 nm yielded a slope of 0.29 ± 0.01 $mg \cdot m^{-2} \cdot nm^{-1}$. Another interesting feature to note is the similar intercept for NC (2.9 ± 0.1 $mg \cdot m^{-2}$) and RC (2.6 ± 0.1 $mg \cdot m^{-2}$) films when the linear fit of the NC data was extrapolated to d = 0. This suggests that the adsorption of PCs onto RC and NC were probably affected more by differences in accessible surface areas than the difference between amorphous and crystalline cellulose.

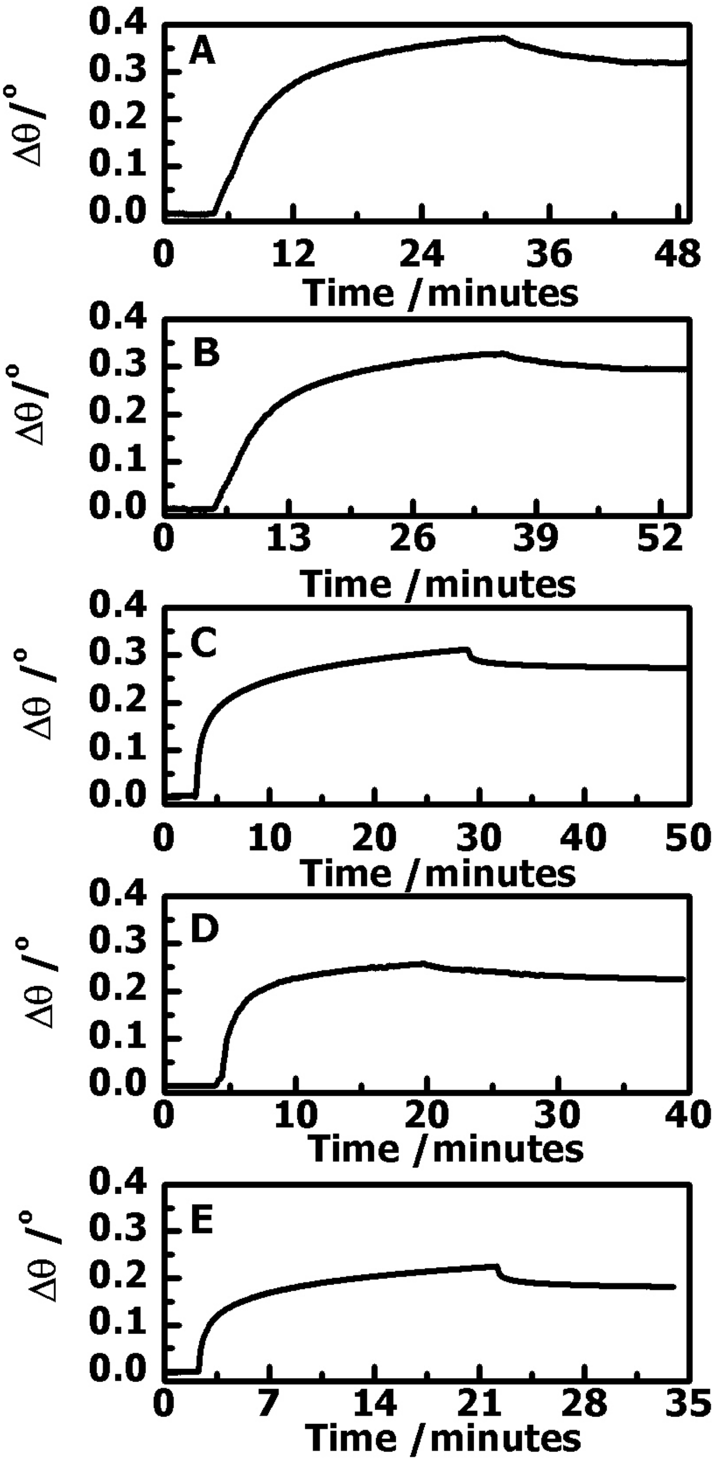

Figure 4.16. Representative SPR data for PC (DS = 0.08, 1 g·L^{-1}) adsorption onto (A) 14.9 nm, (B) 12.5 nm, (C) 10.2 nm, (D) 7.9 nm, and (E) 4.5 nm NC films at 20.0 °C.

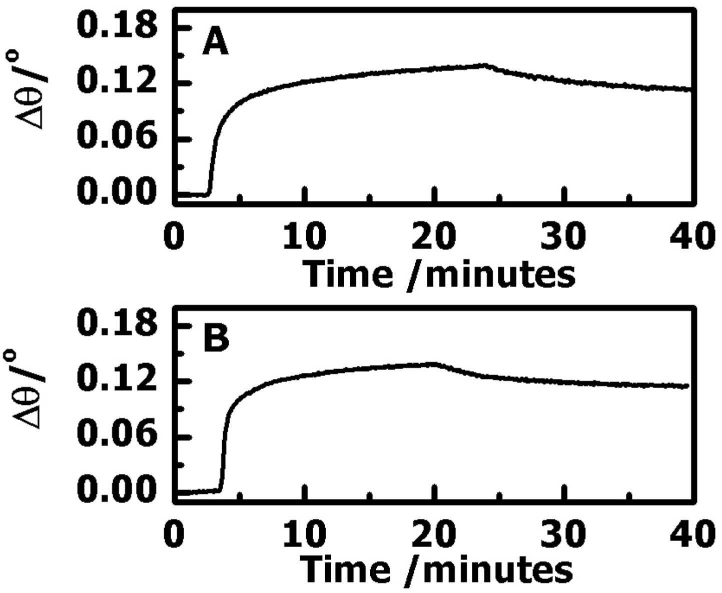

Figure 4.17. Representative SPR data for PC (DS = 0.08, 1 g·L^{-1}) adsorption onto (A) 6.2 nm and (B) 15.3 nm RC films at 20.0 °C.

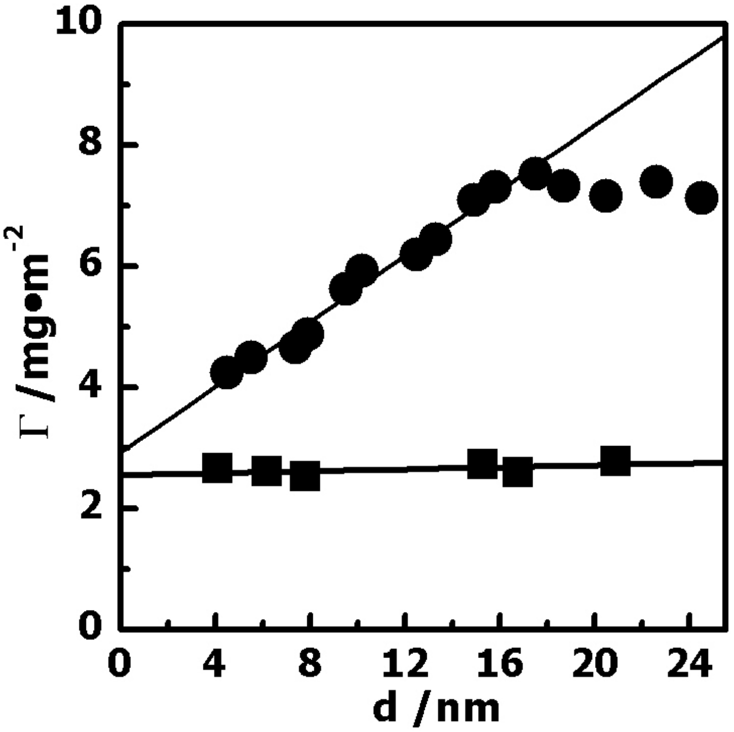

Figure 4.18. Γ versus d from ellipsometry for PC (DS = 0.08) adsorption onto (●) NC and (■) RC films. Solid lines represent linear fits.

The adsorption of PC (DS = 0.06) onto NC films with different thicknesses (Figures 4.19 and 4.21) was similar to data for PC (DS = 0.08). The PC (DS = 0.06) data exhibited a linear relationship between Γ and d up to d ~8 nm followed by a plateau around 2.1 $mg \cdot m^{-2}$. The slope of Γ vs. d (0.12 ± 0.01 $mg \cdot m^{-2} \cdot nm^{-1}$) was smaller than that of PC (DS = 0.08). The different slope values of Γ vs. d plots seem to be consistent with the binding affinity of a polymer with the NC films (higher slope = stronger adsorption). Γ was still independent of d for PC interactions with RC films (Figures 4.20 and 4.21). When extrapolated to d = 0, the intercepts for NC (1.24 ± 0.04 $mg \cdot m^{-2}$) and RC (1.17 ± 0.03 $mg \cdot m^{-2}$) films were also the same within experimental error. The fit parameters of Γ vs. d for PC DS ~ 0.06 and 0.08 before saturation are summarized in Table 4.6. The common intercept was interpreted as a PC film confined to the top of the NC surface that was similar to RC films. Hence, it was concluded that differences in accessible surface area between crystalline and amorphous cellulose films rather than differences in binding interactions between crystalline and amorphous surfaces was responsible for higher apparent binding to NC surfaces.

Table 4.6. Parameters from Γ versus d for DS = 0.06 and 0.08 PC prior to saturation in Figures 4.18 and 4.21.

	DS=0.08		DS=0.06	
	Intercept ($mg \cdot m^{-2}$)	Slope ($mg \cdot m^{-2} \cdot nm^{-1}$)	Intercept ($mg \cdot m^{-2}$)	Slope ($mg \cdot m^{-2} \cdot nm^{-1}$)
NC	2.9 ± 0.1	0.29 ± 0.01	1.24 ± 0.04	0.12 ± 0.01
RC	2.6 ± 0.1	—	1.17 ± 0.03	—

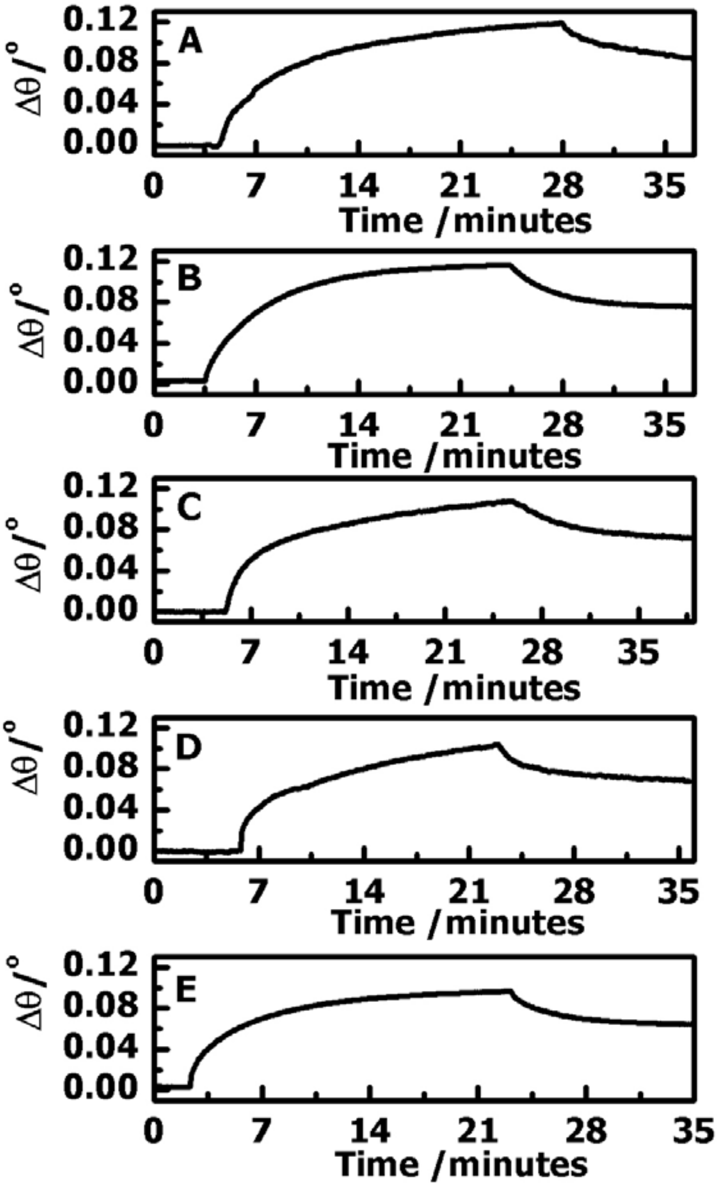

Figure 4.19. Representative SPR data for PC (DS = 0.06, 1 g·L^{-1}) adsorption onto (A) 7.6 nm, (B) 6.7 nm, (C) 5.3 nm, (D) 4.6 nm, and (E) 3.8 nm NC films at 20.0 °C.

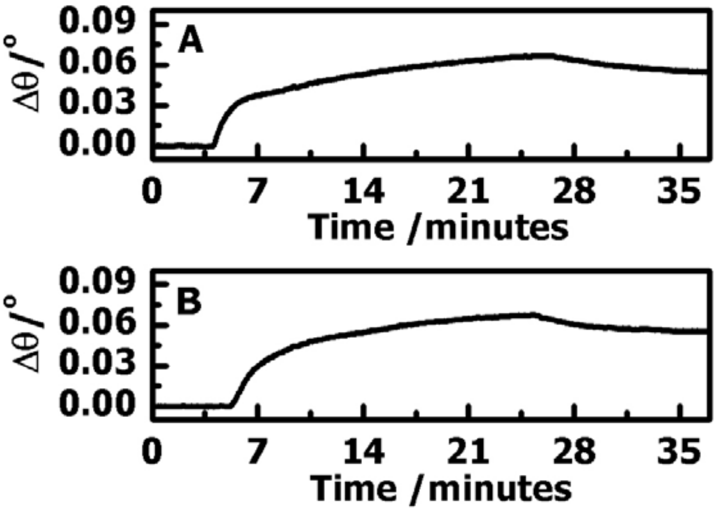

Figure 4.20. Representative SPR data for PC (DS = 0.06, 1 g·L^{-1}) adsorption onto (A) 4.4 nm and (B) 9.6 nm RC films at 20.0 °C.

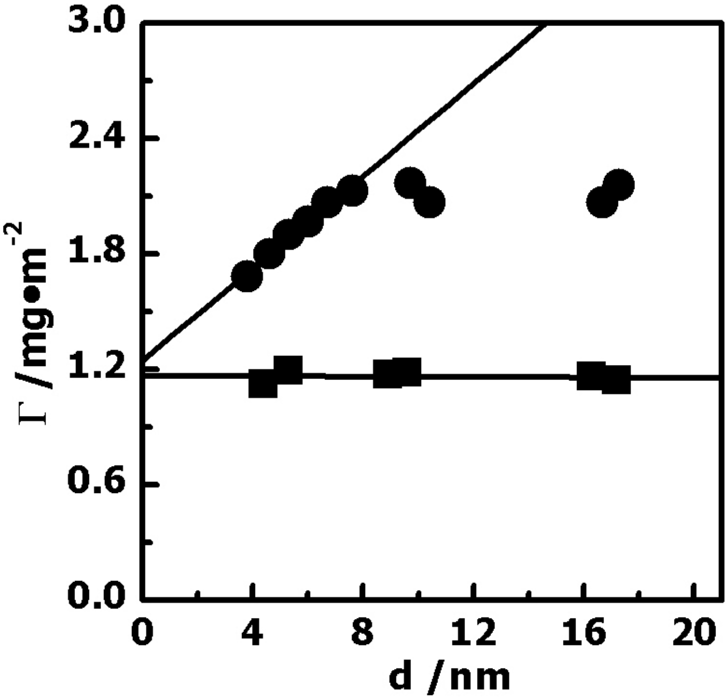

Figure 4.21. Γ versus d from ellipsometry for PC (DS = 0.06) adsorption onto (●) NC and (■) RC films. Solid lines represent linear fits.

We also measured PC (DS = 0.03) and pullulan adsorption onto cellulose films with variable thicknesses (Figure 4.22-4.27). However, there was no obvious dependence of Γ on d for PC (DS = 0.03) and pullulan adsorption onto NC films. This was attributed to the fact that pullulan and PC003 only adsorbed at the top of the NC films without significant penetration. Adsorption onto RC films yielded a slightly lower plateau Γ than the NC films. This further supported our hypothesis that crystallinity of cellulose samples had little impact on interactions of adsorbates with cellulose films. The excess Γ values observed for PC (DS = 0.06 and 0.08) arose from sorption into the NC films.

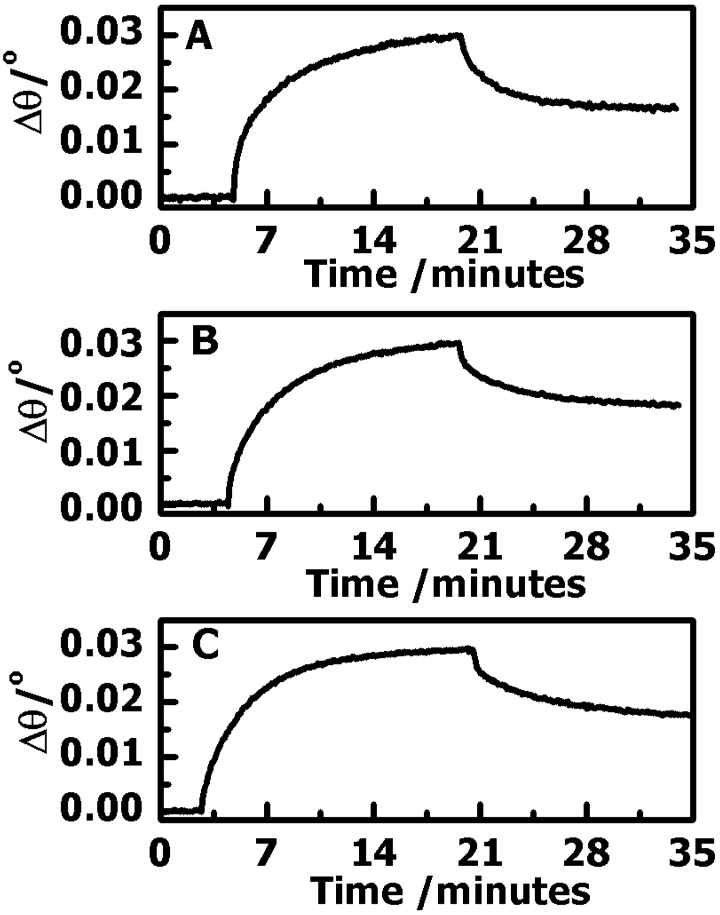

Figure 4.22. Representative SPR data for PC (DS = 0.03, 1 g·L^{-1}) adsorption onto (A) 16.7 nm, (B) 10.6 nm, and (C) 5.6 nm NC films at 20.0 °C.

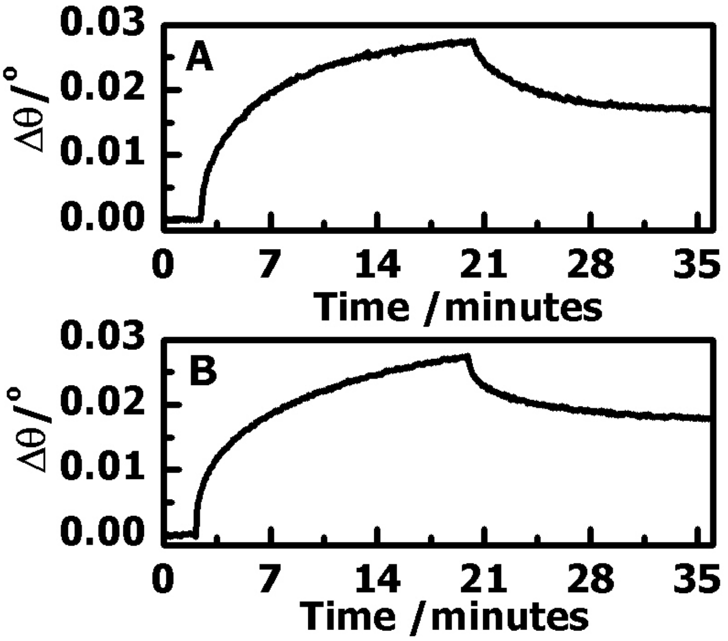

Figure 4.23. Representative SPR data for PC (DS = 0.03, 1 g·L^{-1}) adsorption onto (A) 8.5 nm and (B) 14.1 nm RC films at 20.0 °C.

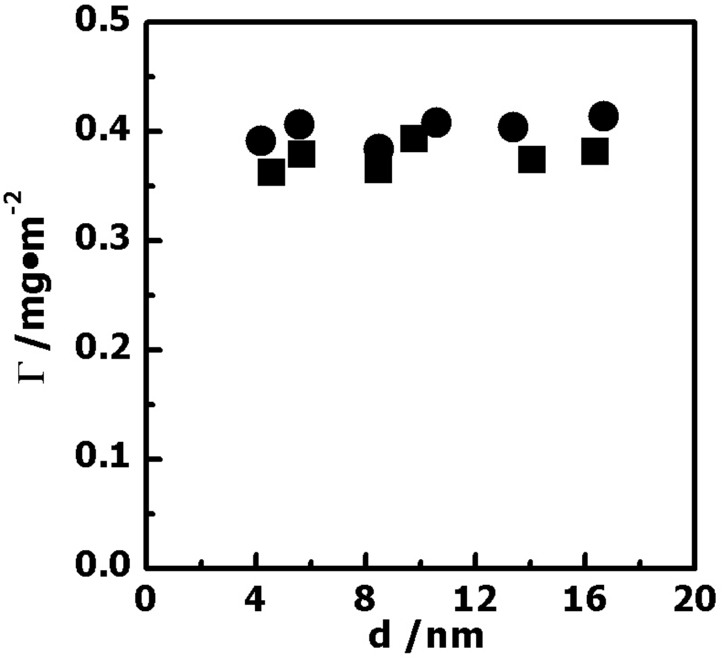

Figure 4.24. Γ versus d from ellipsometry for PC (DS = 0.03) adsorption onto (●) NC and (■) RC films.

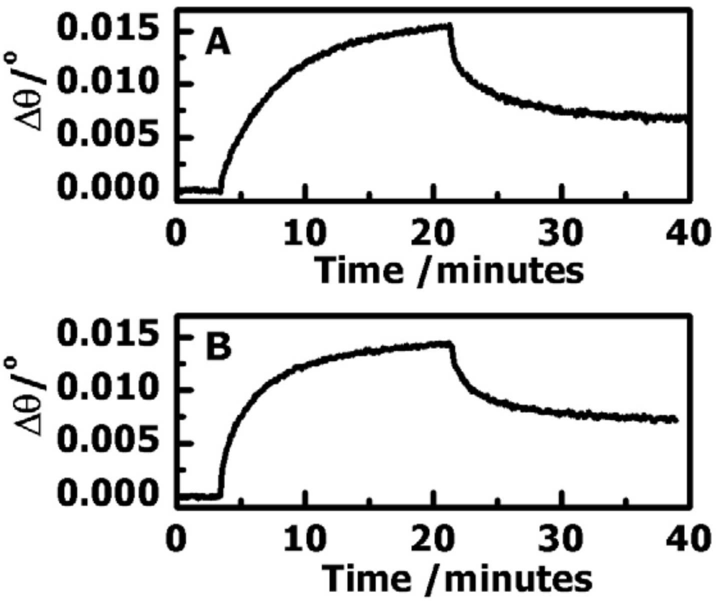

Figure 4.25. Representative SPR data for pullulan 1 g·L^{-1} adsorption onto (A) 13.7 nm and (B) 7.3 nm NC films at 20.0 °C.

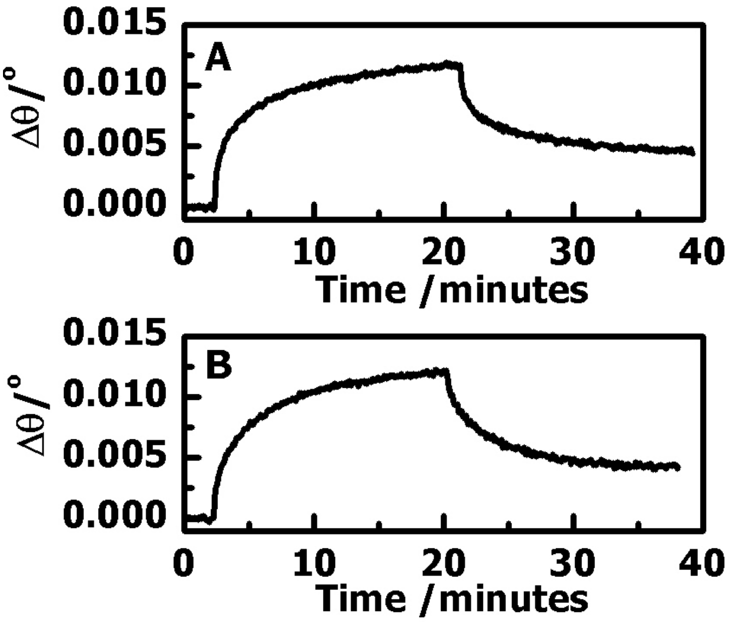

Figure 4.26. Representative SPR data for pullulan 1 g·L^{-1} adsorption onto (A) 6.5 nm and (B) 15.7 nm RC films at 20.0 °C.

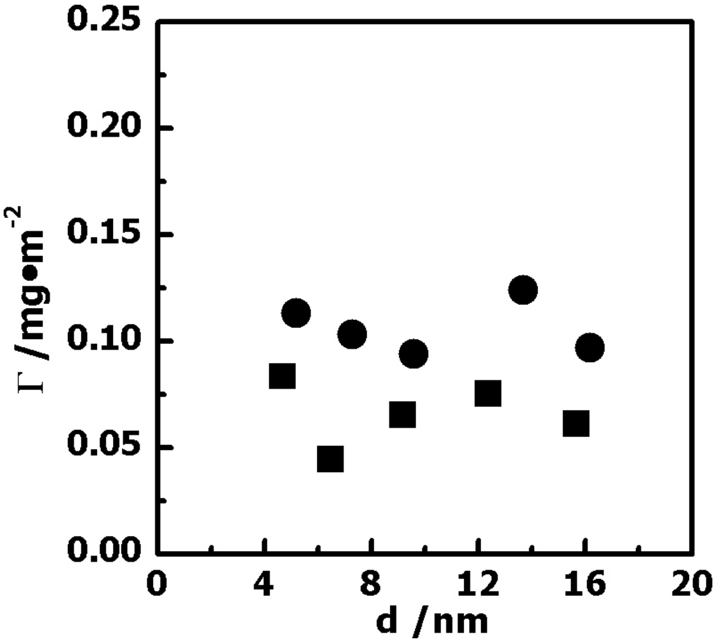

Figure 4.27. Γ versus d from ellipsometry for pullulan adsorption onto (●) NC and (■) RC films.

4.5 Conclusions

In summary, pullulan cinnamate adsorption onto NC films was studied by a combination of techniques. The cellulose I NC films anchored by a SAM-NH_2 surface were prepared from cellulose nanocrystal suspensions. The uniform NC films showed much greater crystallinity than RC films where cellulose chains were mostly unoriented and amorphous. The presented SPR measurements showed that pullulan and PC DS = 0.03 only adsorbed onto the top of the NC films at submonolayer to monolayer coverage (Figure 4.28 A). The excess Γ for the adsorption of PCs with high DS onto NC films arose from sorption into the NC films rather than only sticking to the top layers (Figure 4.28 B). The interactions between PC chains and the highly porous NC films led to looped conformations and significant roughness changes. As seen in the graph of Γ vs. d (Figure 4.29), the cross-over point, slope of the linear portion of the film, and plateau value were all affected by cinnamate DS. The fact that intercepts of Γ extrapolated to d =

0 for NC and RC films had the same values meant higher Γ values for NC films arose from porosity and accessible surface area differences rather than inherent differences in binding strength. The results in this chapter illustrate the impact of the surface properties of different model cellulose films on adsorption. These features need to be considered when trying to produce biomimetic nanocomposites based on the self-assembly seen in plant cell walls.

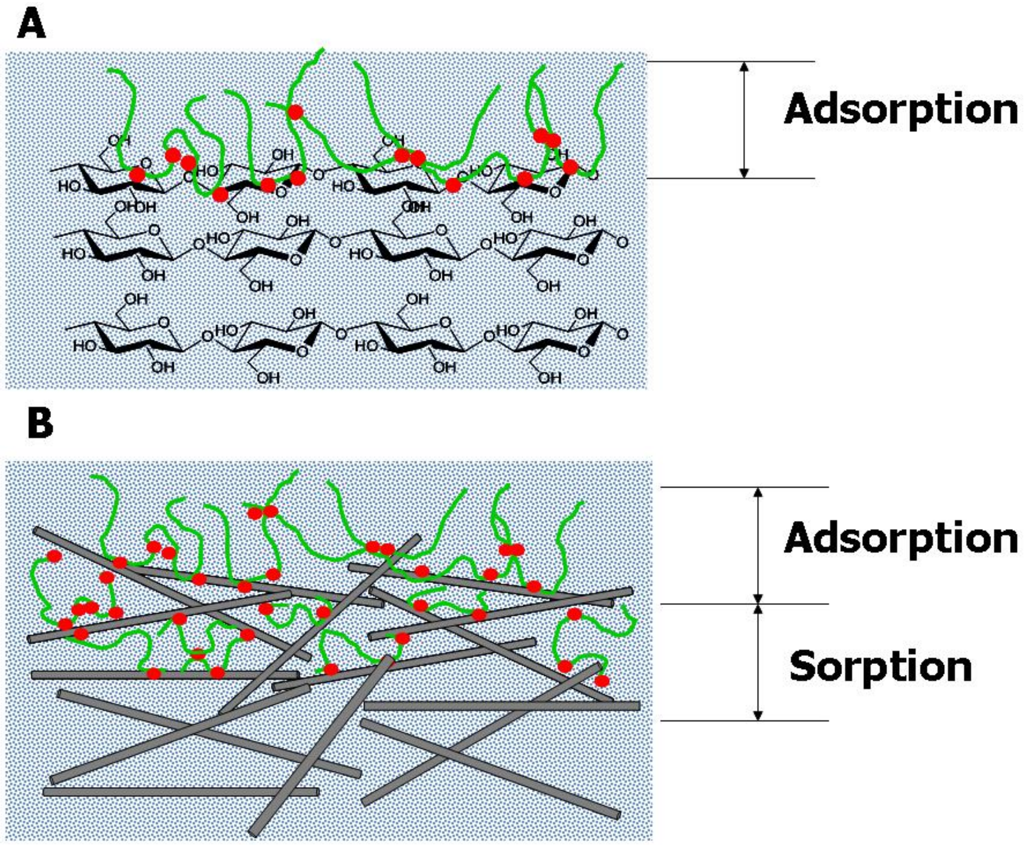

Figure 4.28. Schematic depiction of PC with high DS interactions with (A) RC and (B) NC films. Green lines represent pullulan chains whereas red spots are cinnamate groups.

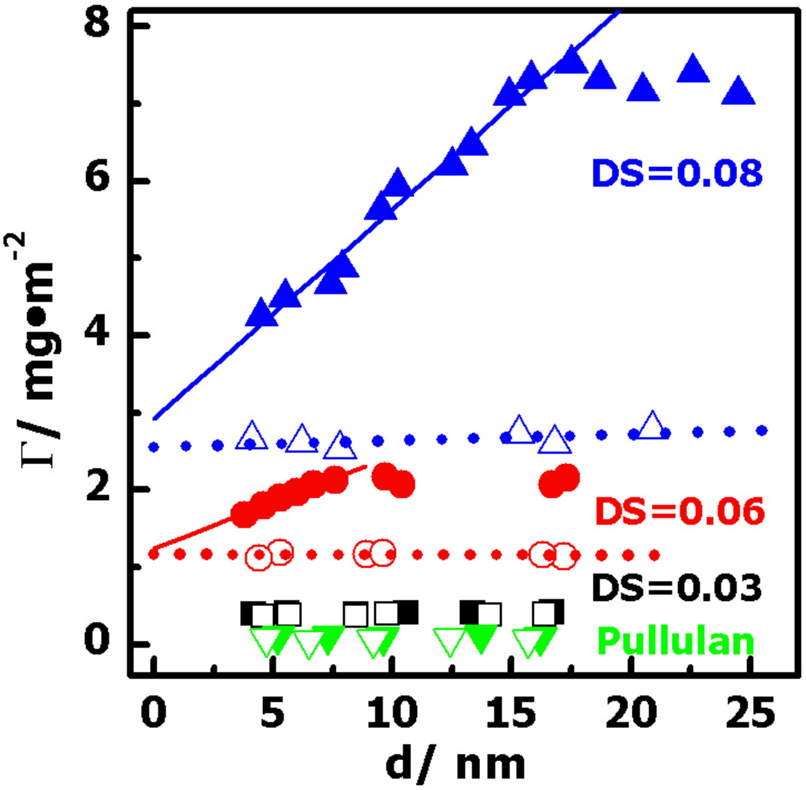

Figure 4.29. Γ versus d for P and PC adsorption onto NC (solid symbols) and RC (hollow symbols) films. Solid and dotted lines represent linear fits.

4.6 References:

(1) Dupuy, A. D.; Engelman, D. M. *Proc. Natl. Acad. Sci. U. S. A.* **2008**, *105*, 2848–2852.

(2) Alberts, B.; Johnson, A.; Lewis, J.; Raff, M.; Roberts, K.; Walter, P. Molecular Biology of the Cell, 4th Ed., Garland Science, New York, 2002.

(3) Mohanty, A. K.; Misra, M.; Drzal, L. T. *Composite Interfaces* **2001**, *8*, 313-343.

(4) Samir, M. A. S. A.; Alloin, F.; Dufresne, A. *Biomacromolecules* **2005**, *6*, 612-626.

(5) Gradwell, S. E.; Renneckar, S.; Esker, A. R.; Heinze, T.; Gatenholm, P.; Vaca-Garcia, C.; Glasser, W. *C. R. Biol.* **2004**, *327*, 945-953.

(6) Kaya, A.; Du, X.; Liu, Z.; Lu, J. W.; Morris, J. R.; Glasser, W. G.; Heinze, T.; Esker, A. R. *Biomacromolecules* **2009,** *10*, 2451-2459.

(7) Yennawar N. H.; Li L.; Dudzinski D. M.; Tabuchi A. ; Cosgrove D. J. *Proc. Natl. Acad. Sci. U. S. A.* **2006**,*103*, 14664-14671.

(8) Kontturi, E.; Tammelin, T.; Österberg, M. *Chem. Soc. Rev.* **2006**, *35*, 1287-1304.

(9) Schaub, M.; Wenz, G.; Wegner, G.; Stein, A.; Klemm, D. *Adv. Mater.* **1993**, *5*, 919-922.

(10) Buchholz, V.; Wegner, G.; Stemme, S.; Ödberg, L. *Adv. Mater.* **1996**, *8*, 399-402.

(11) Edgar, C. D.; Gray, D. G. *Cellulose* **2003**, *10*, 299-306.

(12) Beck-Candanedo, S.; Roman, M.; Gray, D. G. *Biomacromolecules* **2005**, *6*, 1048-1054.

(13) Ahola, S.; Salmi, J.; Johansson, L. S.; Laine, J.; Österberg, M. *Biomacromolecules* **2008**, *9*, 1273-1282.

(14) Müller, M.; Czihak, C.; Schober, H.; Nishiyama, Y.; Vogl, G. *Macromolecules* **2000**, *33,* 1834-1840.

(15) Ahola, S.; Turon, X.; Österberg, M.; Laine, J.; Rojas, O. J. *Langmuir* **2008**, *24*, 11592-11599.

(16) Eriksson, M.; Notley, S. M.; Wågberg, L. *Biomacromolecules* **2007,** *8*, 912-919.

(17) Aulin, C.; Ahola, S.; Josefsson, P.; Nishino, T.; Hirose, Y.; Österberg, M.; Wågberg, L. *Langmuir*, **2009**, *25*, 7675-7685.

(18) Kittle, J. D.; Du, X.; Jiang, F.; Qian, C.; Roman, M.; Heinze, T.; Esker, A. R. *Biomacromolecules,* **2011**, *12*, 2881-2887.

(19) Ni, S.; Yin, W.; Ferguson-McPherson, M. K.; Satija, S. K.; Morris, J. R.; Esker, A. R. *Langmuir* **2006**, *22*, 5969-5973.

(20) Oh, S. Y.; Yoo, D. I.; Shin, Y.; Kim, H. C.; Kim, H. Y.; Chung, Y. S.; Park, W. H.; Youk, J. H. *Carbohydr. Res.* **2005**, *340*, 2376-2391.

(21) Kondo, T.; Sawatari, C. *Polymer* **1996**, *37*, 393-399.

(22) Schwanninger, M.; Rodrigues, J. C.; Pereira, H.; Hinterstoisser, B. *Vib. Spectrosc.* **2004**, *36*, 23-40.

(23) Mwaikambo, Y.; Ansell, M. P. *Die Angewandte Makromolekulare Chemie* **1999**, *272*, 108-116.

(24) De Feijter, J. A.; Benjamins, J.; Veer, F. A. *Biopolymers* **1978,** *17*, 1759-1772.

(25) Evans, D. F.; Wennerström, H. *The Colloidal Domain: Where Physics, Chemistry, Biology, and Technology Meet* 2nd ed.; Wiley-VCH: New York, 1999.

(26) Kawaguchi, T.; Nakahara, H.; Fukuda, K. *Thin Solid Films* **1985**, *133*, 29-38.

(27) Sedin D. L.; Rowlen K. L. *Applied Surface Science* **2001**, *182*, 40-48.

(28) Jiang, F.; Esker, A. R.; Roman, M. *Langmuir* **2010**, *26*, 17919–17925.

(29) Bennett, M. E.; Alexander, W. A.; Lu, J. W.; Troya, D.; Morris, J. R. *J. Phys. Chem. C* **2008,** *112,* 17272-17280.

(30) Höök, F.; Kasemo, B.; Nylander, T.; Fant, C.; Sott, K.; Elwing, H. *Analytical chemistry* **2001**, *73*, 5796-5804.

（31） Craig, V. S.; Plunkett, M. *Journal of Colloid and Interface Science* **2003**, *262*, 126-129.

(32) Sauerbrey, G. *Zeitschrift Fur Physik* **1959**, *155*, 206-222.

(33) Müller, M.; Czihak, C.; Schober, H.; Nishiyama, Y.; Vogl, G. *Macromolecules* **2000**, *33*, 1834-1840.

(34) Hatakeyama, H.; Hatakeyama, T. *Thermochimica Acta* **1998**, *308*, 3-22.

CHAPTER 5

Phospholipid Vesicle Interactions with Cellulose Surfaces

5.1 Abstract

Interactions between phospholipid vesicles and regenerated cellulose (RC) or nanocrystalline cellulose (NC) films were investigated by quartz crystal microbalance with dissipation monitoring, surface plasmon resonance and *in-situ* atomic force microscopy experiments. Partial lipid layers of dioleoylphosphatidylcholine (DOPC) with smooth features formed on RC surfaces, whereas large aggregates of intact vesicles assembled onto NC surfaces. All the phospholipid structures were found on the top surface without permeation into the interiors of the cellulose films. The large differences in degree of hydration for DOPC structures on the two cellulose surfaces, ~ 30% versus ~ 80% by mass for RC versus NC, respectively, were consistent with different conformations from lamellar films to floppy layers, respectively. A vesicle to layer transformation on NC surfaces was triggered by a destabilizing agent, LysoPC. Initial binding of LysoPC micelles to unruptured vesicles was clearly resolved by SPR signals. The maximal uptake of LysoPC monomers by membranes reached 14% by mass percent followed by tremendous desorption of lipids and coupled water. The destabilization of the spherical vesicles and the final rupture of membrane structures are believed to arise from an exchange between LysoPC monomers and DOPC molecules and intimate contact between lipid headgroups, respectively. The resulting multilayer phospholipid structures on the NC surfaces (~ 4 DOPC layers) had similar degrees of hydration (~ 30% by mass) as the disconnected lipid islands on RC surfaces. The smooth structure of DOPC multilayers on NC films masked the underlying rod-like crystalline domains in both AFM height and phase images. These results supported the

hypothesis that LysoPC had the capability to facilitate the conversion of vesicles on solid substrates to layered structures. Overall, the vesicle layers versus planar layered structures, provide a perfect platform for studying membrane related processes within intact cells and lipid rafts.

5.2 Introduction

Over the past decades, supported lipid membranes on ultrathin hydrophilic polymer films have attracted intensive research attention. The resulting biomimetic cell membrane on hydrated polymer surfaces exhibited many advantages relative to rigid solid substrates such as greater lateral mobility and enough space for trans-membrane proteins.[1,2] It also provided a thermodynamically stable and homogeneous model surface for both fundamental investigations of membrane-related behavior, like transmembrane proteins insertion into biomimetic cell membranes and ion channels for biosensing applications. As the main component of plant cell walls, cellulose fibers have been noted for their interactions with cell membranes which are mostly composed of phospholipids.[3,4] The transmembrane protein complex within the phospholipid bilayers, cellulose synthase complex, is believed to be responsible for the polymerization of cellulose chains from single glucose units in plant cells.[5] Through the study of interactions between cellulose and phospholipids, underlying mechanisms of plant cell wall self-assembly may be elucidated and could inform the next generation of nanocomposites based upon biomimicry of plant cell wall structures.

The first model cellulose surfaces were obtained from Langmuir-Blodgett deposition of trimethylsilylcellulose (TMSC) followed by exposure of the TMSC coated surface to 10% hydrochloric acid vapor whereby regenerated cellulose (RC) films were obtained.[6,7] Later, RC films were also obtained from spincoated TMSC films.[8] Smooth nanocrystalline cellulose (NC) films have been prepared from cellulose nanocrystal suspensions in aqueous media.[9,10] Subsequently, cellulose surfaces composed of both crystalline and amorphous cellulose regions were prepared from cellulose nanofibril dispersions that were closer to the native state of cellulose structures.[11] The first reported deposition of a lipid bilayer onto model cellulose surfaces was achieved through horizontal Langmuir-Schaefer transfer.[12] More recently, it was shown that phospholipid bilayers could be formed on silica substrates through a fusion process that involved direct vesicle-substrate interactions.[13] In general, vesicles approached the surface followed by slight deformations once they contacted the substrate. Vesicle rupture occured when a critical concentration of vesicles was present on the surface. Phospholipid layers spontaneously propagated until a fully covered bilayer was formed.

The induced fusion of the cell membranes on gold surfaces by an amphiphilic peptide[14] was previously studied as a mechanism to facilitate vesicle to planar bilayer structure transitions. The conversion process was monitored by both acoustic and optical mass changes to better understand the initial binding of the peptide and corresponding conformational changes of the lipid structures. Another catalyst capable of triggering vesicle breakages, single-tail lipid micelles composed of monooleoylphosphatidylcholine, was investigated by micropipette techniques to follow their interactions with single phospholipid vesicles in solution.[15-17] The uptake of single-tail lipid molecules by the vesicle membrane was estimated by measuring the circumference change of the spherical vesicle. It was observed that single lysolipid molecules only interacted with the outer layer of the membrane and could be easily removed from the vesicle bilayer upon exposure to lysolipid-free media. After long-time exposure to lysolipid micelle solution above its critical micelle concentration (CMC), the collapse of phospholipid vesicle structure was observed by optical microscopy. The intimate contacts between lipid headgroups were believed to induce the exchange of micelle molecules with the phospholipid molecules within the vesicle membranes.

In this chapter, the interactions of phospholipid vesicles with two different cellulose surfaces, regenerated cellulose and nanocrystalline cellulose, were investigated through a combination of quartz crystal microbalance with dissipation monitoring (QCM-D), surface plasmon resonance (SPR) and *in situ* atomic force microscopy (AFM) experiments. Disconnected lipid islands were observed for 1,2-dioleoyl-sn-glycero-3-phosphocholine (DOPC) adsorption onto RC surfaces while NC surfaces favored intact vesicles. The intact vesicle layers on NC films were then transformed into planar multilayers over NC surfaces by exposure to the solution containing a fusion agent, 1-oleoyl-sn-glycero-3-phosphocholine (LysoPC).

5.3 Experimental

DOPC and LysoPC in chloroform were purchased from Avanti Polar Lipids (Alabaster, AL). Chloroform-solvated lipid mixtures were dried under nitrogen until a thin film formed at the bottom of the vials. The residual organic solvent was evaporated by vacuum oven drying (25 Torr, 50 ˚C) for 3 hours. Ultrapure water was then added to the vial containing dried phospholipid until the required lipid concentration was achieved. The resulting liposome solution was sonicated until it became clear. Procedures for the preparation of NC and RC films, film thickness measurement by multiple-angle-of-incidence ellipsometry, SPR measurements, QCM-D measurements and *in situ* AFM imaging were described in Chapter 3.3, and 3.4, respectively.

5.4 Results and Discussion

5.4.1 Adsorption of Phospholipid onto Model Surfaces by QCM-D and SPR

Representative frequency (Δf) and dissipation changes (ΔD) for one overtone ($n = 7$) by QCM-D measurements are shown in Figure 5.1. The cellulose surfaces were equilibrated in water for 1 hour until a flat baseline was achieved. After that, DOPC from a 250 mg•L^{-1} aqueous solution was flowed over the cellulose surfaces. The immediate signal change of Δf and ΔD was consistent with rapid liposome adsorption onto the cellulose surfaces. The large scaled frequency decrease, $(\Delta f/n) = -244 \pm 9$ Hz, and dissipation increase, $\Delta D = (46 \pm 2) \times 10^{-6}$ were observed after flushing with water. This significant adsorption was indicative of the adsorption of a floppy DOPC vesicle layer onto the corrugated NC surfaces without large elastic deformation of the vesicles, which enhanced energy dissipation of the adsorbed films.[18] Major contributions to the substantial acoustic mass and dissipation changes came from a large amount of trapped water in the interstices between unruptured vesicles and inside the centers of the vesicles which were mechanically coupled to the NC surfaces.[19] On the other hand, adsorption of DOPC onto RC surfaces only yielded a small frequency decrease of $(\Delta f/n) = -14 \pm 1$ Hz with a dissipation change of $\Delta D = (1.7 \pm 0.1) \times 10^{-6}$. This indicated that DOPC adsorbed onto RC surfaces formed a more rigid layered structure.

Since the ratio between dissipation changes and frequency decreases were not small for DOPC adsorption onto either type of cellulose film, the Sauerbrey equation[20] which is only valid for rigid films with a negligible ΔD/Δf ratio was not valid. Instead, a Voigt-base viscoelastic model[19] which takes into account both dissipation and frequency changes, was used to determine the hydrodynamic surface excess (Γ_{QCM-D}). Three overtones ($n = 5$, 7 and 9) were used to estimate Γ_{QCM-D}. The overtones $n = 1$ and 3 were neglected because of insufficient energy trapping.[21] Detailed parameters for DOPC liposome adsorption onto cellulose films are given in Table 5.1.

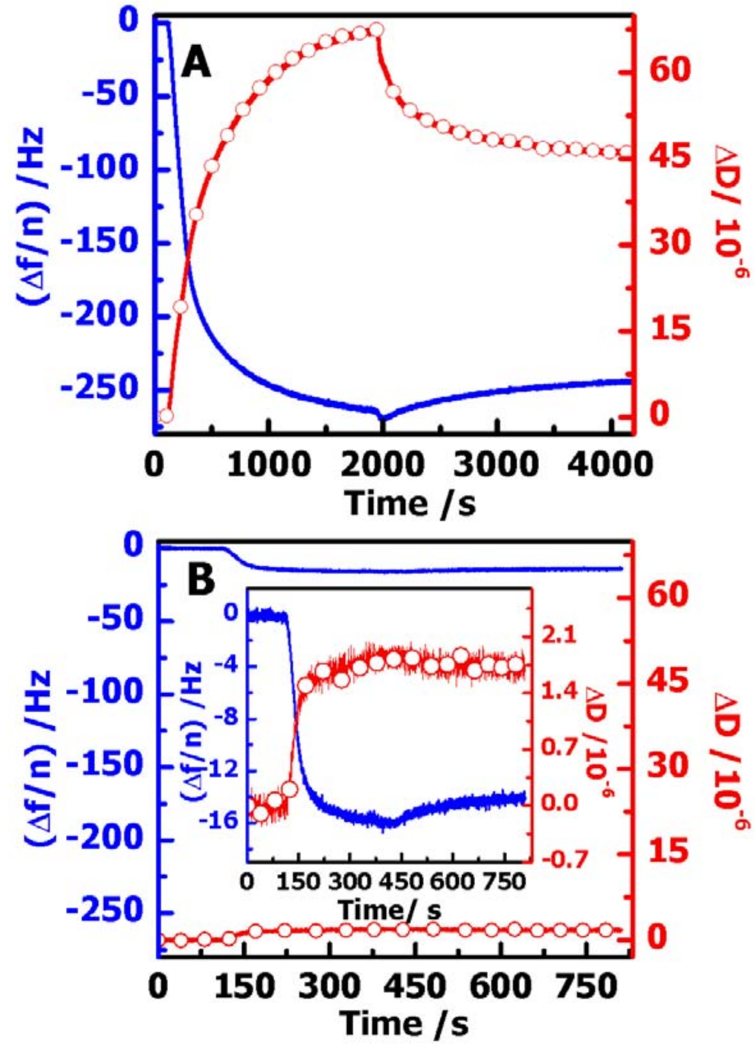

Figure 5.1. (Δf/n) (blue line) and ΔD (red line with circles) for the overtone n = 7 versus time for DOPC adsorption onto (A) NC surfaces and (B) RC surfaces at 20.0 °C. Water was flowed through the QCM-D module prior to and after DOPC solution. The y-axis range of graph B was chosen to match graph A in order to highlight greater adsorption onto NC surfaces relative to RC surfaces, whereas the inset in (B) magnified the changes for RC surfaces. Film thicknesses of the NC and RC films were 13.9 ± 0.4 nm and 14.1 ± 0.5 nm, respectively.

By taking the differential of the frequency and dissipation changes with respect to time,[22] differences in the rate of DOPC mass adsorption ($d(\Delta f/n)/dt$) onto cellulose substrates and the energy transfer from the surrouding media ($d\Delta D/dt$) could be detected (Figure 5.2). Both ($d(\Delta f/n)/dt$) and ($d\Delta D/dt$) graphs showed a narrow peak for DOPC deposition onto RC surfaces that quickly equilibrated to 0 over a period of 400 s, indicating that the bulk DOPC was deposited as essentially rigid structures within this time frame. In contrast, DOPC adsorption onto NC surfaces showed a much greater and broader peak that slowly approached zero. It indicated large mass deposition and energy transfer continued over a longer time scale for NC surfaces than RC surfaces. These results are explained by the high viscoelasticiy of intact vesicles and their stronger mechanical coupling and energy exchange with the surrounding media.

Table 5.1. Parameters for DOPC adsorption onto RC and NC surfaces.

Parameters	RC	NC
$\Delta\theta_{max}$ (°)	0.07 ± 0.01	0.67 ± 0.04
($\Delta f/n$) (Hz)	-14 ± 1	-244 ± 9
$\Delta D \times 10^6$	1.7 ± 0.1	46 ± 2
Γ_{SPR} ($mg \bullet m^{-2}$)	2.1 ± 0.4	16 ± 1
$\Gamma_{QCM\text{-}D}$ ($mg \bullet m^{-2}$)	3.0 ± 0.2	97 ± 4
%Degree of Hydration [a]	31 ± 6	84 ± 5

[a] %Degree of Hydration was calculated as $(1-\Gamma_{SPR}/\Gamma_{QCM\text{-}D})\times 100\%$

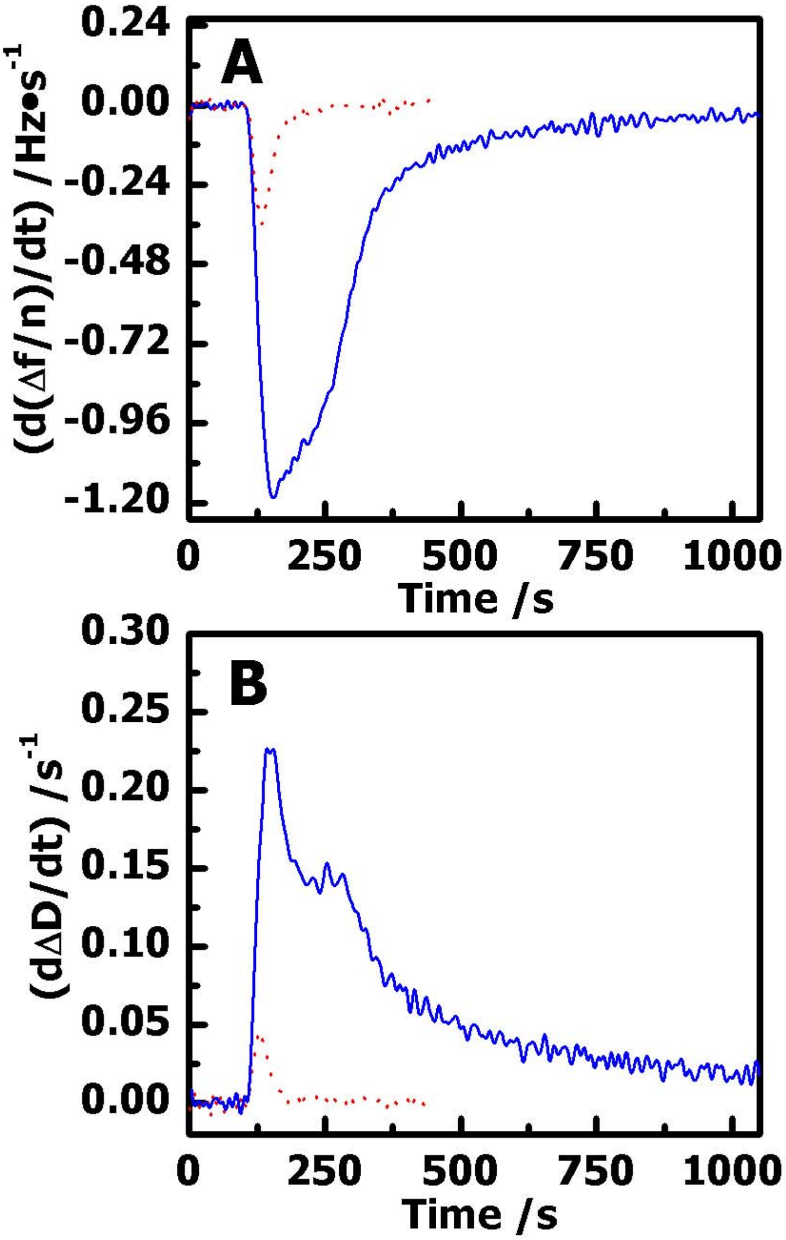

Figure 5.2. Differentials of (A) frequency (d(Δf/n)/dt) and (B) dissipation changes (dΔ*D*/d*t*) for the n = 7 vs. time for DOPC liposome adsorption onto NC (blue solid line) and RC (red dotted line) surfaces.

SPR was chosen to measure the optical mass or "dry mass" of DOPC structures onto cellulose films (analysis of SPR data was described in Chapter 3.4.6). Each experiment was carried out three times and angle changes for the Γ analysis were extracted from SPR curves like those shown in Figure 5.3. SPR data was consistent with DOPC adsorption onto NC surfaces at 8× greater levels than onto RC films. Similar values for the maximum ($\Delta\theta_{max}$) and irreversible angle changes ($\Delta\theta_{irr}$) of DOPC adsorption onto NC films were indicative of completely irreversible adsorption. The acoustic mass from QCM-D measurements corresponded to the total mass including water and phospholipid, whereas the optical mass deduced from SPR signals only determined the dry mass of DOPC structures (without coupled water). Therefore, the combination of QCM-D and SPR results allowed for the calculation of the degree of hydration of the adsorbed DOPC films (see Table 5.1). The highly hydrated vesicle layers of DOPC that adsorbed onto NC surfaces had degrees of hydration as great as 84 ± 5% by mass, while the degrees of hydration for lipid layer structures adsorbed onto regenerated cellulose surfaces were 31 ± 6% by mass. While the degrees of hydration were substantially different, it was interesting to note that there was still a significant amount of water associated with the bilayer patches. This fact further supported the legitimacy of Voigt-based viscoelastic modeling for the highly hydrated bilayer structures. After consideration of the molecular weight (786.1 $g \cdot mol^{-1}$) and molecular area (0.57 ± 0.02 nm^2) of the DOPC molecule,[23] the theoretical surface concentration of an intact well-ordered DOPC bilayer was $\Gamma = 4.6 \pm 0.1$ $mg \cdot m^{-2}$. The combination of the theoretical surface concentration with a 30% degree of hydration, yielded a theoretical $\Gamma = 6.6 \pm 0.1$ $mg \cdot m^{-2}$ for a wet DOPC bilayer on supported substrates. A comparison of the theoretical Γ with the experimental wet value from QCM-D ($\Gamma = 3.0 \pm 0.2$), revealed DOPC bilayers on RC films only covered ~ 45% of the surface.

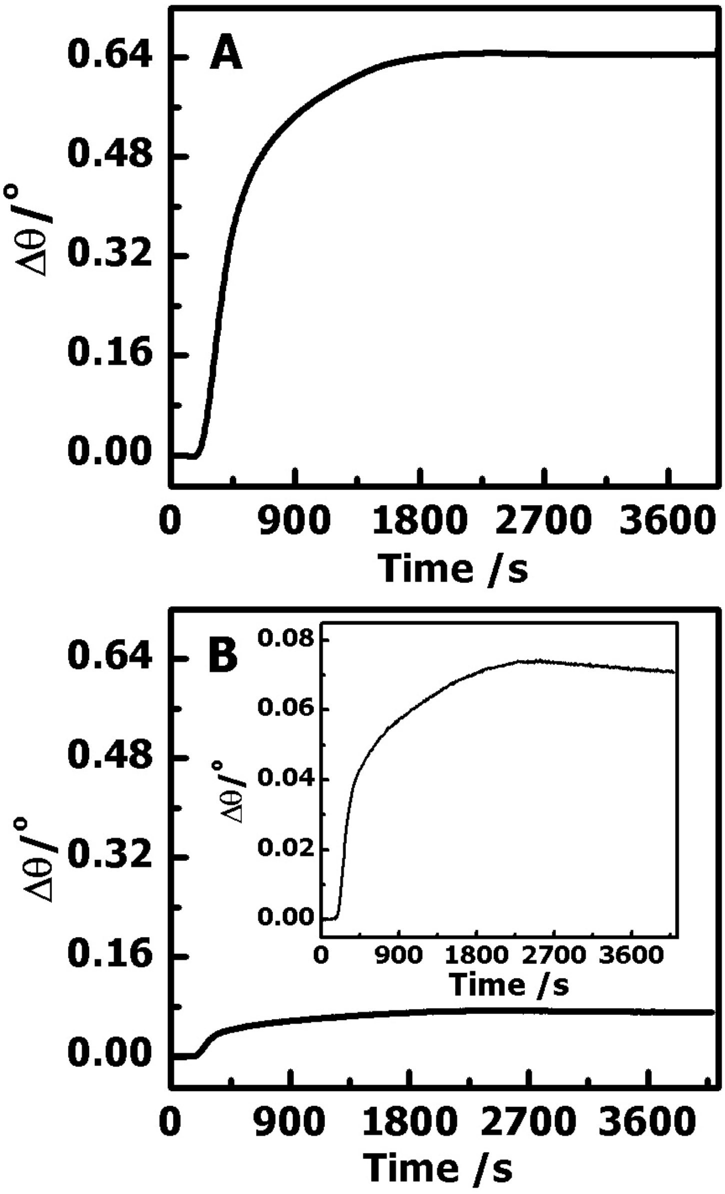

Figure 5.3. Representative SPR angle changes for DOPC adsorption onto (A) NC and (B) RC films at 20.0 °C. Water was flowed through the SPR fluid cell prior to and after DOPC solution. The y-axis range of graph B was chosen to match graph A in order to highlight greater adsorption onto NC surfaces relative to RC surfaces, whereas the inset in (B) magnified the changes for RC surfaces. Film thicknesses of NC and RC films were 13.9 ± 0.4 nm and 14.1 ± 0.5 nm, respectively.

In order to determine whether the DOPC vesicles or bilayers resided only on the top surface or penetrated through the polymer films, phospholipid adsorption onto cellulose films with different thicknesses (d) were carried out. The film thicknesses of cellulose films were measured by multiple-angle-of-incidence ellipsometry prior to adsorption measurements. Experimental results showed that after flushing with water, both the frequency decrease, $(\Delta f/n) \sim -250$ Hz for $n = 7$, and dissipation increase, $\Delta D = 45\times10^{-6}$, associated with DOPC adsorption onto NC films were independent of film thickness (Figure 5.4). This observation indicated that vesicles only adsorbed onto the top of the film rather than penetrating into porous NC films.[24] In Figure 5.5, similar behavior was observed for DOPC adsorption onto RC films with various film thicknesses, $(\Delta f/n) \sim -14$ Hz for $n = 7$, with a dissipation change around 1.6×10^{-6}. In contrast to pullulan cinnamate interactions with NC films (Chapter 4) where adsorption occurred at the top of the film, along with sorption into the film, DOPC showed no detectable penetration into the porous NC films or the densely packed RC films. These positive results led to further treatment of vesicle layers over cellulose films with the fusion agent, LysoPC.

Table 5.2. Parameters for DOPC adsorption onto RC and NC surfaces with various film thicknesses.

	d (nm)	(Δf/n) (Hz)	$\Delta D\times10^6$	Γ_{QCM-D} (mg•m^{-2})
NC	4.6 ± 0.2	-247 ± 9	47 ± 3	101 ± 6
	9.3 ± 0.3	-250 ± 8	44 ± 3	98 ± 5
	13.9 ± 0.4	-244 ± 9	46 ± 2	97 ± 4
RC	5.1 ± 0.2	-13 ± 1	1.6 ± 0.1	2.7 ± 0.2
	14.1 ± 0.5	-14 ± 1	1.7 ± 0.1	3.0 ± 0.2

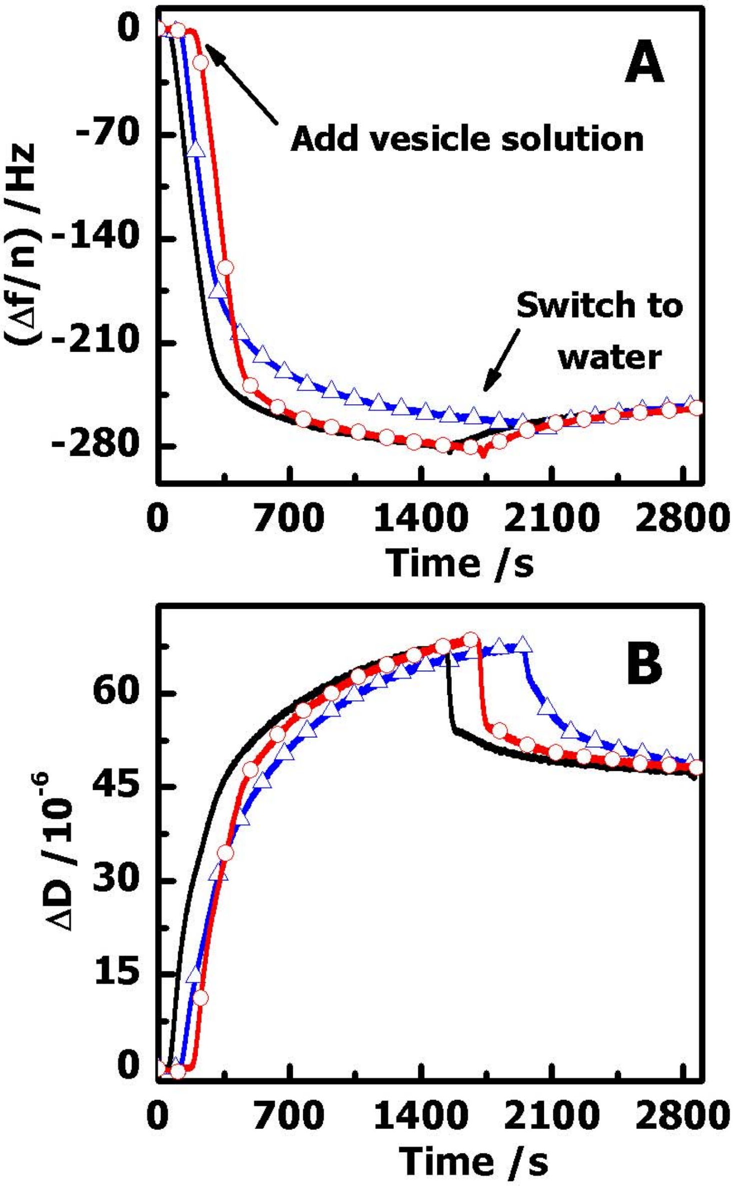

Figure 5.4. Representative (A) (Δf/n) and (B) ΔD for $n = 7$ vs. time for DOPC adsorption onto NC films with thicknesses of 4.6 nm (black line), 9.3 nm (red line with circles) and 13.9 nm (blue line with triangles) at 20.0 °C. Water was flowed through the QCM-D module prior to and after DOPC solution.

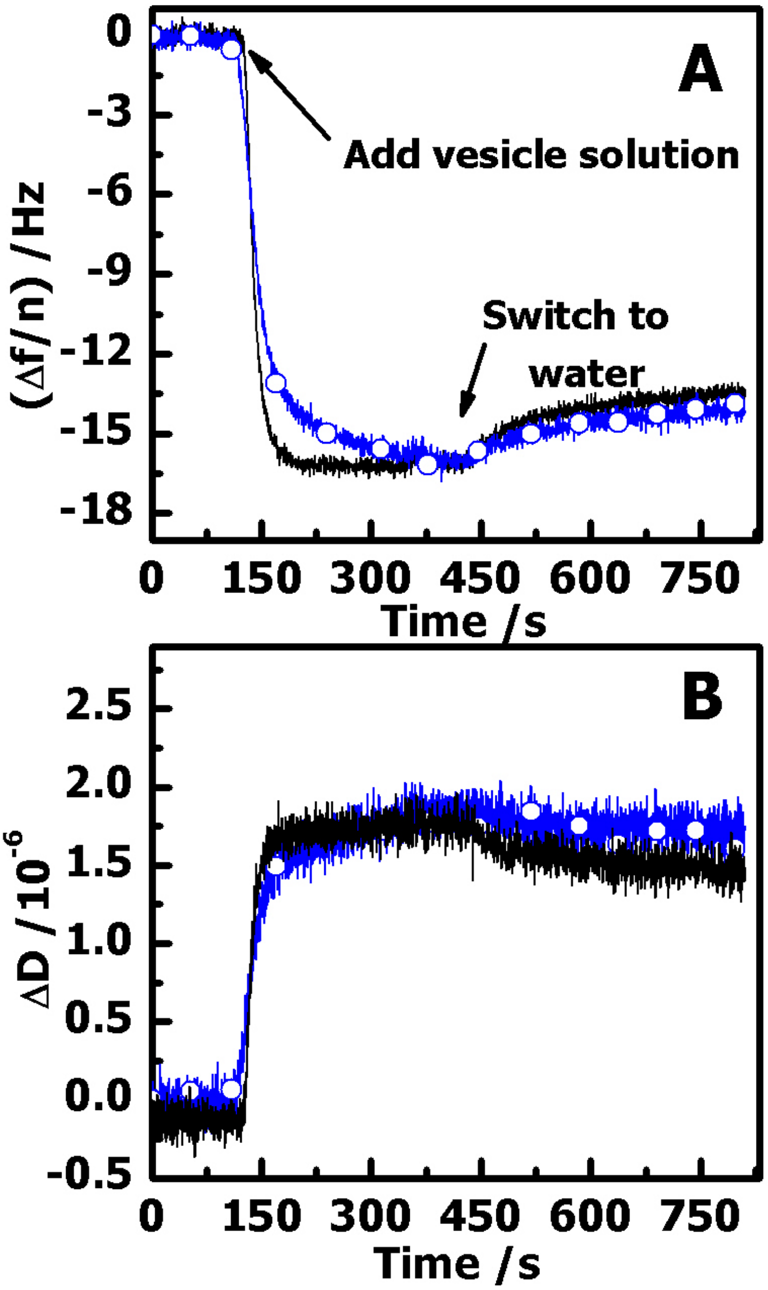

Figure 5.5. Representative (A) (Δf/n) and (B) ΔD for n = 7 vs. time for DOPC adsorption onto RC films with thicknesses of 5.1 nm (black line) and 14.1 nm (blue line with circles) at 20.0 °C. Water was flowed through the QCM-D module prior to and after DOPC solution.

5.4.2 AFM Studies of Phospholipid Adsorption onto Model Surfaces

Topologies of the solid/liquid interface for cellulose surfaces prior to adsorption and the same surfaces after exposure to DOPC liposomes from a 250 $mg•L^{-1}$ aqueous solution and a subsequent rinse with water observed by *in situ* AFM are shown in Figures 5.6 and 5.7. DOPC adsorption onto NC surfaces not only masked the rod-like cellulose nanocrystal morphology (Figure 5.6 A), but also led to large aggregates of intact DOPC vesicles (Figure 5.6 C and E). These aggregates could not be removed by a water rinse indicating irreversible adsorption. The root-mean-square (RMS) surface roughness changes of NC films nearly doubled from 2.6 nm to 4.3 nm after DOPC adsorption. To further confirm phospholipid vesicle adsorption onto the NC films, phase imaging known for its capability of differentiating between different components in composite materials on the basis of viscoelasticity are shown in Figure 5.6 B, D and F. The pronounced difference in phase contrast between DOPC aggregates and background cellulose films clearly showed phospholipid vesicles on top of the NC surfaces.

In contrast to the NC surfaces, RC films were smoother with smaller features (cellulose domains) in height and phase images (Figure 5.7 A and B).[25] Only disconnected lipid islands observed on height images of RC films after DOPC adsorption may have increased surface roughness from 0.9 nm to 1 nm. While the surface roughness in Figure 5.7 C and E might indicate a partially covered lipid layer on the RC films, the strong phase contrast between DOPC bilayers and underlying RC films in Figure 5.7 D and F facilitated unambiguous identification of planar phospholipid structures on top of the NC surfaces.

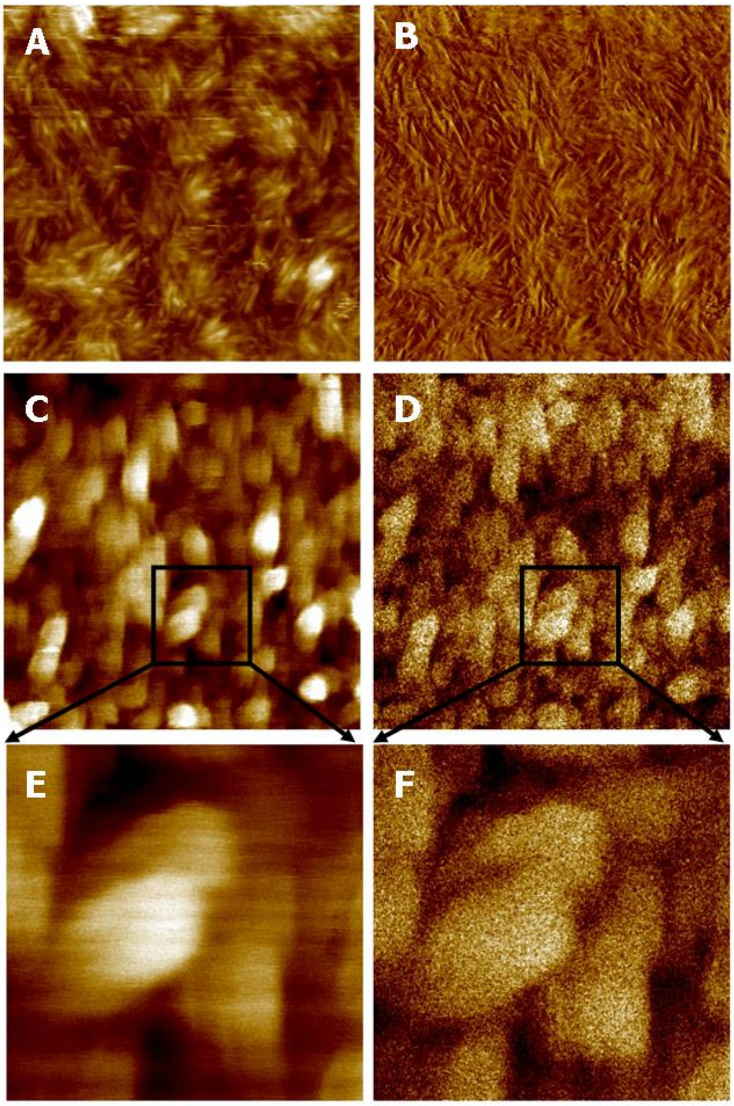

Figure 5.6. Representative AFM images. (A) Height and (B) phase images of the solid/liquid interface for nanocrystalline cellulose prior to DOPC adsorption. (C) Height and (D) phase images of the solid/liquid interface after DOPC adsorption onto nanocrystalline cellulose from a bulk solution (250 mg•L^{-1}). The AFM images of (A) through (D) are 2 × 2 μm^2 with z scales for height and phase of 0 to 40 nm and 0 to 10 degrees, respectively. (E) Height and (F) phase images were enlarged to 500 × 500 nm^2 from the black boxes in C and D, respectively, with the same z scales.

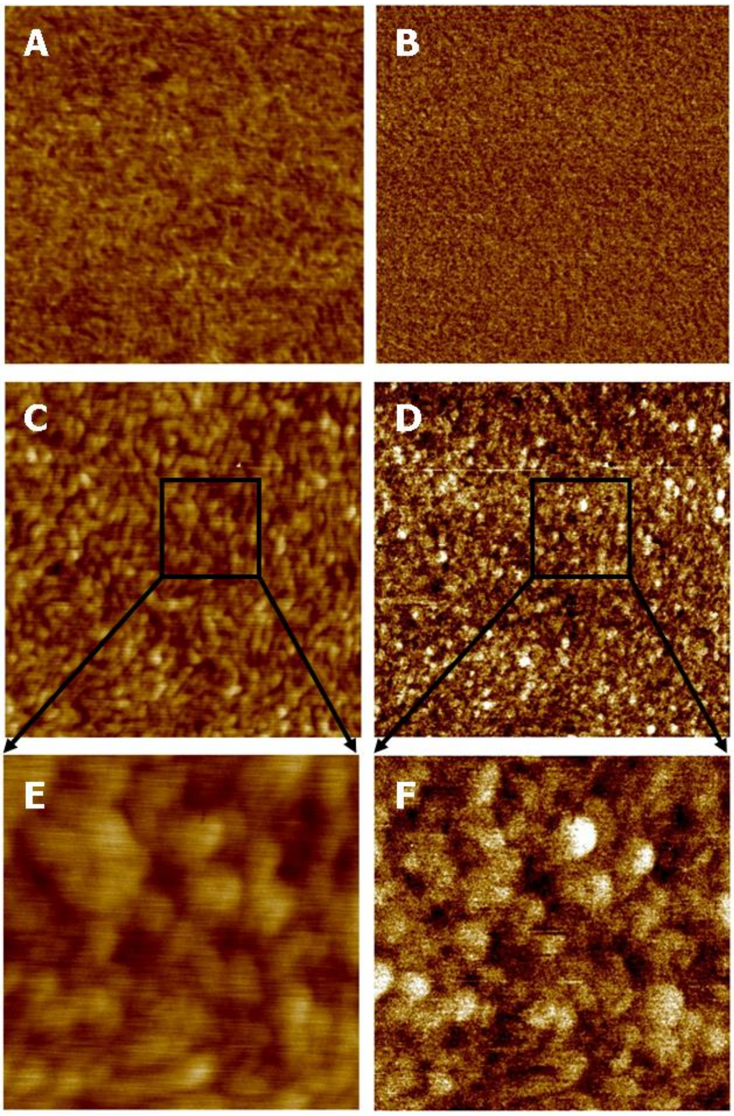

Figure 5.7. Representative AFM images. (A) Height and (B) phase images of the solid/liquid interface for regenerated cellulose prior to DOPC adsorption. (C) Height and (D) phase images of the solid/liquid interface after DOPC adsorption onto regenerated cellulose from a bulk solution (250 mg•L^{-1}). The AFM images of (A) through (D) are 2 × 2 μm^2 with z scales for height and phase of 0 to 20 nm and 0 to 5 degrees, respectively. (E) Height and (F) phase images were enlarged to 500 × 500 nm^2 from the black boxes in C and D, respectively, with the same z scales.

5.4.3 DOPC Vesicle Adsorption onto NC Surfaces Followed by LysoPC Treatment

A single-tailed phospholipid,[15-17] LysoPC, known for its positive curvature in micellar structures and ability to destabilize and rupture intact vesicles in solution was employed to convert the intact vesicles on NC surfaces into planar lipid layer structures. The combination of SPR and QCM-D measurements permitted us to observe the interactions between LysoPC micelles and intact vesicles with both dry and wet mass changes. The degree of hydration deduced from the optical and acoustic mass could indicate the role of LysoPC in the transformation process of vesicle (high water content) to layer structure (less coupled water). By monitoring mass changes and viscoelastic properties, we can resolve both the binding and destabilization processes of LysoPC onto intact vesicle layers.

Representative QCM-D and SPR data for DOPC liposome adsorption onto NC surfaces followed by exposure to 25 μM LysoPC are shown in Figures 5.8 and 5.9. Two regimes were clearly identified: (a) The formation of an intact vesicle layer over the NC films and (b) the conversion to a more rigid layer structure induced by LysoPC. The huge drop of ΔD from 46×10^{-6} to 4×10^{-6} for $n = 7$ after LysoPC treatment confirmed conversion from a floppy vesicle layer to a more rigid DOPC lamellar structure. The total mass of DOPC over NC films prior to and after LysoPC exposure were fit by a Voigt-based model using three overtones ($n=5$, 7 and 9). However, acoustic mass alone cannot resolve many of the details associated with interactions between the LysoPC micelles and the vesicles. Only a significant mass and dissipation decrease caused by the release of water was observable in the QCM-D measurements after the addition of LysoPC. The large acoustic mass decrease associated with the loss of water from leaking vesicles hides the initial binding of LysoPC to the DOPC vesicles. In contrast, SPR angle changes, which are a function of refractive index and effective thickness, detected the initial binding more effectively. As seen in Figure 5.9, the initial binding of LysoPC to DOPC vesicles occurred at 4000 s. The maximal uptake of LysoPC at 4200 s increased the total mass by ~ 14% prior to a huge mass decrease because of DOPC desorption shortly thereafter. The degree of hydration which recorded the hydrodynamically coupled water content were calculated as $(1-\Gamma_{spr}/\Gamma_{QCM\text{-}D})\times100\%$ assuming ideal solution behavior. The sudden decrease of the degree of hydration from 84 ± 5% to 29 ± 3% after LysoPC exposure confirmed the structural transformation from soft vesicle layer to rigid planar structure. This result shows that degree of hydration is an important indicator of viscoelastic properties and correlates well with both the mass and dissipation changes. By comparing the final $\Gamma_{QCM\text{-}D}$ of DOPC planar structures (14.05 ± 1.53 $mg{\bullet}m^{-2}$) with a fully covered hydrated bilayer on solid substrates ($\Gamma_{QCM\text{-}D} = 6.6 \pm 0.1$ $mg{\cdot}m^{-2}$), it was found that a multilayer structure composed of ~ 4 phospholipid layers formed on the NC surfaces after LysoPC treatment. All the parameters of DOPC structures over NC films prior to and after LysoPC treatment are summarized in Table 5.3.

Table 5.3. Parameters for DOPC adsorption onto NC surfaces before and after LysoPC treatment.

Parameters	NC Pre-LysoPC	NC Post-LysoPC
$\Delta\theta_{max}$ (°)	0.67 ± 0.04	0.4 ± 0.02
($\Delta f/n$) (Hz)	-244 ± 9	-60 ± 3
$\Delta D \times 10^6$	46 ± 2	4.0 ± 0.3
Γ_{SPR} (mg•m^{-2})	16 ± 1	9.9 ± 0.3
Γ_{QCM-D} (mg•m^{-2})	97 ± 4	14 ± 1
%Degree of Hydration [a]	84 ± 5	29 ± 3

[a] %Degree of Hydration was calculated as $(1-\Gamma_{spr}/\Gamma_{QCM-D})\times 100\%$

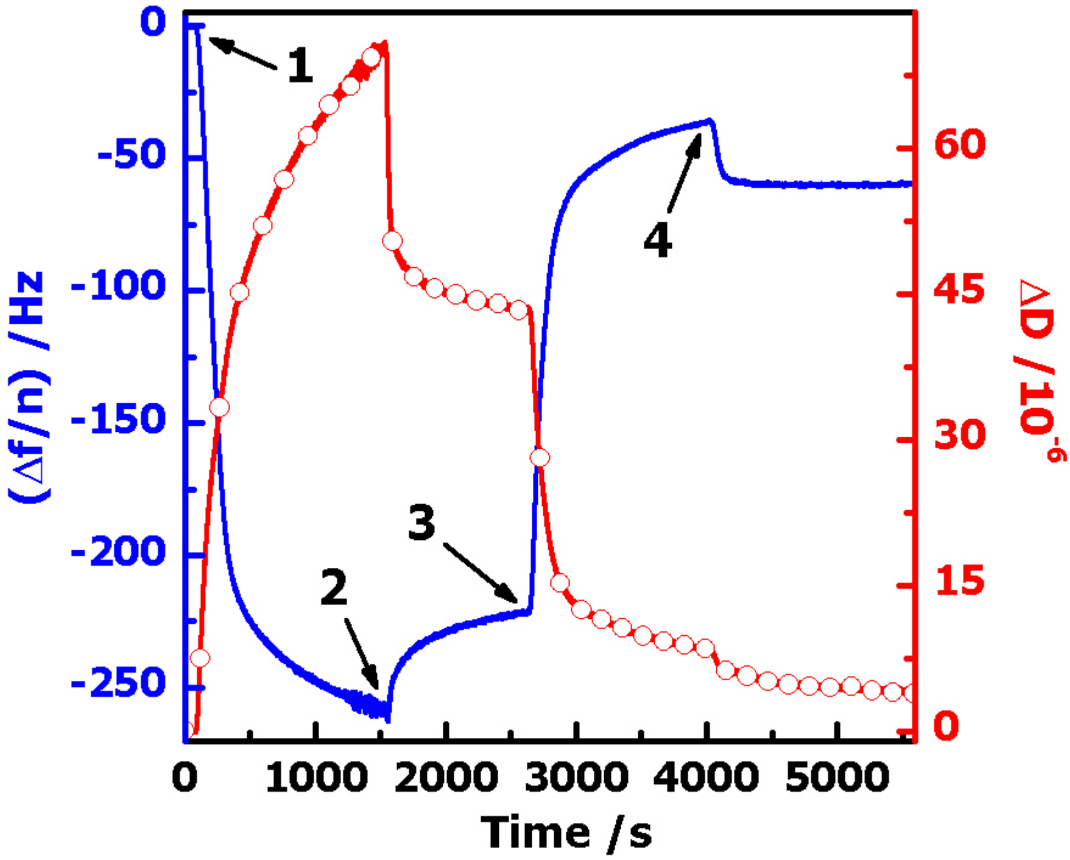

Figure 5.8. (A) (Δf/n) (blue solid line) and ΔD (red line with circles) for n = 7 vs. time for DOPC adsorption onto NC surfaces followed by exposure to LysoPC. After stabilization in water (arrow 1), DOPC was injected into the fluid cell. At arrow 2, water was flushed out the DOPC solution and revealed irreversibly adsorbed vesicles. At arrow 3, LysoPC solution was added to the intact vesicles on the NC surface. At arrow 4, water was flushed out the LysoPC solution.

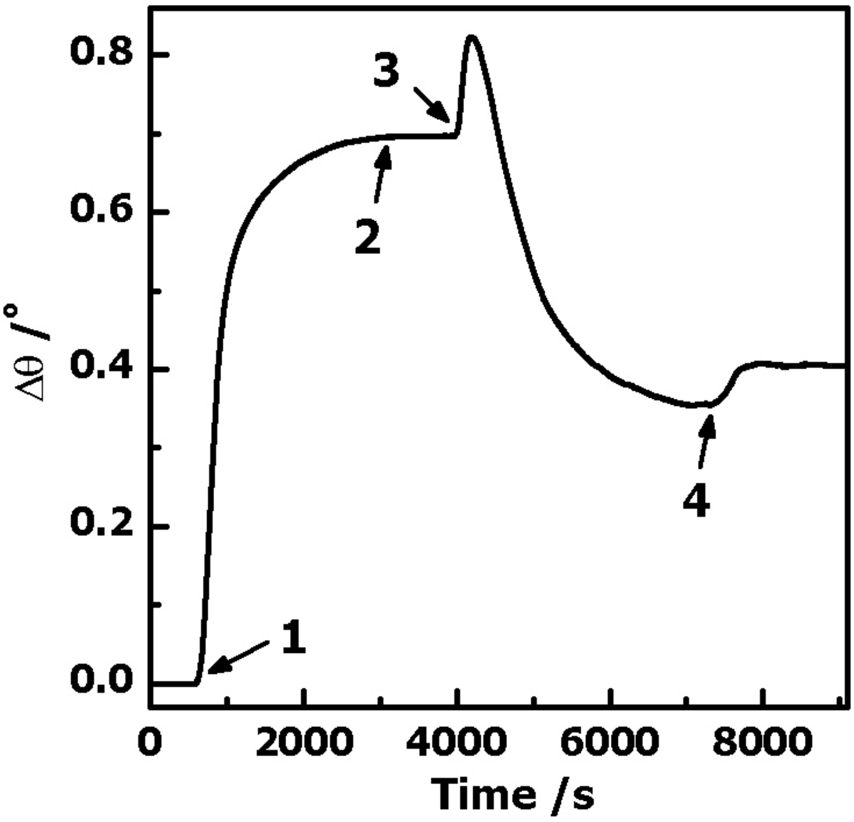

Figure 5.9. Representative SPR data for DOPC adsorption onto NC surfaces followed by exposure to LysoPC. After stabilization in water (arrow 1), DOPC was injected into the fluid cell. At arrow 2, water was used to flush out the DOPC solution and revealed irreversibly adsorbed vesicles. At arrow 3, LysoPC solution was added to the intact vesicles on the NC surface. At arrow 4 water was used to flush out the LysoPC solution.

To further investigate the LysoPC induced transition from vesicle layers of DOPC to planar lipid layers, AFM images were obtained at different stages of the process in Figures 5.8 and 5.9 and are provided in Figures 5.10 and 5.11. The three dimensional AFM images of NC surfaces in Figures 5.10A and 5.11A show a relatively flat feature in the height profile. In Figures 5.10B and 5.11C, packed vesicles as high as 40 nm on NC substrates were clearly observed after DOPC deposition and flushing by water removed irreversibly adsorbed materials. No induced fusion and corresponding vesicle collapse were seen for DOPC interactions with the NC surfaces. The large aggregates of vesicles increased the surface roughnesses of NC films from 2.4 nm to 4.6 nm. The lipid multilayer structures formed after the treatment of LysoPC micelles (Figure 5.10C and 5.11E) lowered the RMS roughness of the surfaces to 2.3 nm, a value comparable to the initially bare NC surface. The smooth lipid structures covered the underlying cellulose nanocrystals so well that no rod-like structures were easily identified in the height images. In the Figure 5.11F, the AFM phase contrast image shows phase boundaries between DOPC planar layers and the underlying crystalline NC films were ambiguous after exposure to LysoPC micelles. The smooth features of the formed phospholipid multilayer structures in the height and phase images are consistent with LysoPC lowering the energy barrier that inhibited the spontaneous formation of multilayer DOPC structures on NC surfaces.

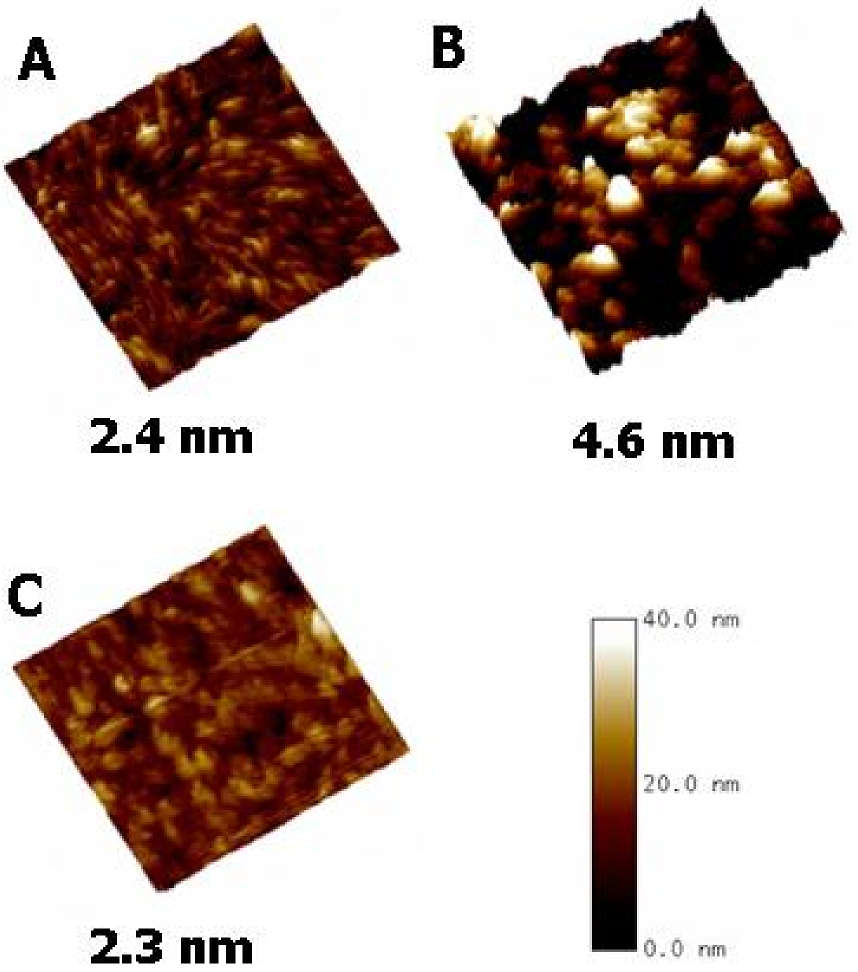

Figure 5.10. Three-dimensional AFM height images of the solid/liquid interface correspond to (A) a NC surface; (B) DOPC vesicles on a NC surface and (C) the exposed surface after the LysoPC treatment. All the AFM images are 2 × 2 μm^2 with a height scale bar from 0 to 40 nm. Root-mean-square surface roughnesses are indicated under each picture.

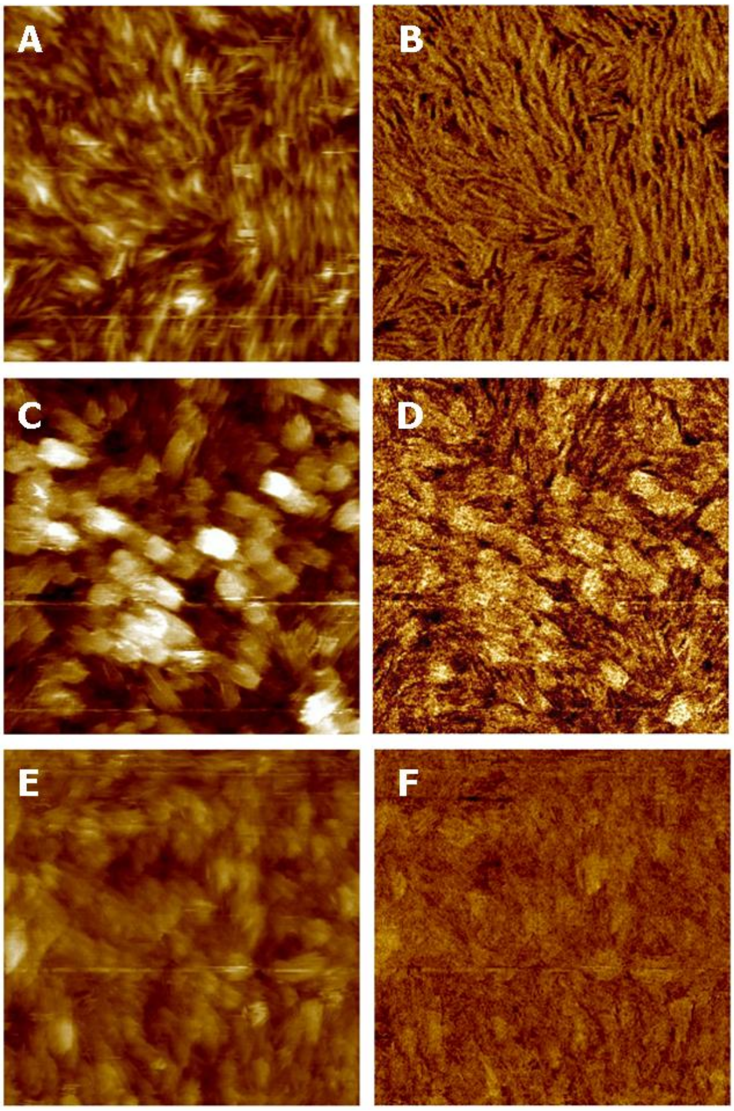

Figure 5.11. Representative AFM images. (A) Height and (B) phase images of the solid/liquid interface for NC prior to DOPC adsorption. (C) Height and (D) phase images of the solid/liquid interface after DOPC adsorption onto a NC surface from a bulk solution (250 mg•L^{-1}). (E) Height and (F) phase images of the solid/liquid interface after the LysoPC treatment. The AFM images are 2 × 2 μm^2 with z scales for height and phase of 0 to 40 nm and 0 to 10 degrees, respectively.

It is well known that surfactant molecules either as monomers or in micelles can interact with phospholipid vesicles by molecular exchange. This process has a huge impact on the stability and physical properties of the phospholipid bilayer of the vesicle. The exchange of lysolipids with lipid molecules within vesicle bilayers and the corresponding bilayer disruption was studied by micropipette techniques.[15] It was observed that lysolipid uptake was limited to the outer layer of the vesicle membrane and failed to cause bilayer solubilization at low concentrations (below the CMC), whereas long time exposure to higher concentrations of LysoPC molecules, i.e. well above the CMC, could lead to membrane solubilization. The interactions of LysoPC micelles with intact DOPC vesicles over NC surfaces were described in Figure 5.12. The micelles in solution approached vesicle bilayers after overcoming a small energy barrier (~ 3 kT).[15] The fast exchange of LysoPC monomers with DOPC molecules accompanied with micelle fusion (at a rate ~ 170 $M^{-1}\cdot s^{-1}$) was attributed to intimate contact between headgroups of the two kinds of lipid molecules. As the vesicles became more enriched with LysoPC molecules, the rupture tension of vesicle membranes decreased rapidly corresponding to a weaker integrity of the bilayer structure. As shown in Figure 5.9, SPR signals showed the uptake of LysoPC molecules by the vesicle membranes continued for about 200 seconds up to ~ 20 mole% prior to final breakage or a complete tensile failure of the vesicle structure. The trapped water inside the hollow vesicles was easily released whereas the bilayers propagated spontaneously to cover the underlying NC films. This whole process was completed when the solution was switched back to LysoPC-free aqueous medium to wash away detergent molecules within the planar DOPC multilayer structures. The desorption rate of LysoPC molecules as monomers from phospholipid bilayers was estimated as 0.4 ± 0.2 s^{-1} by Needham *et al.*[15]

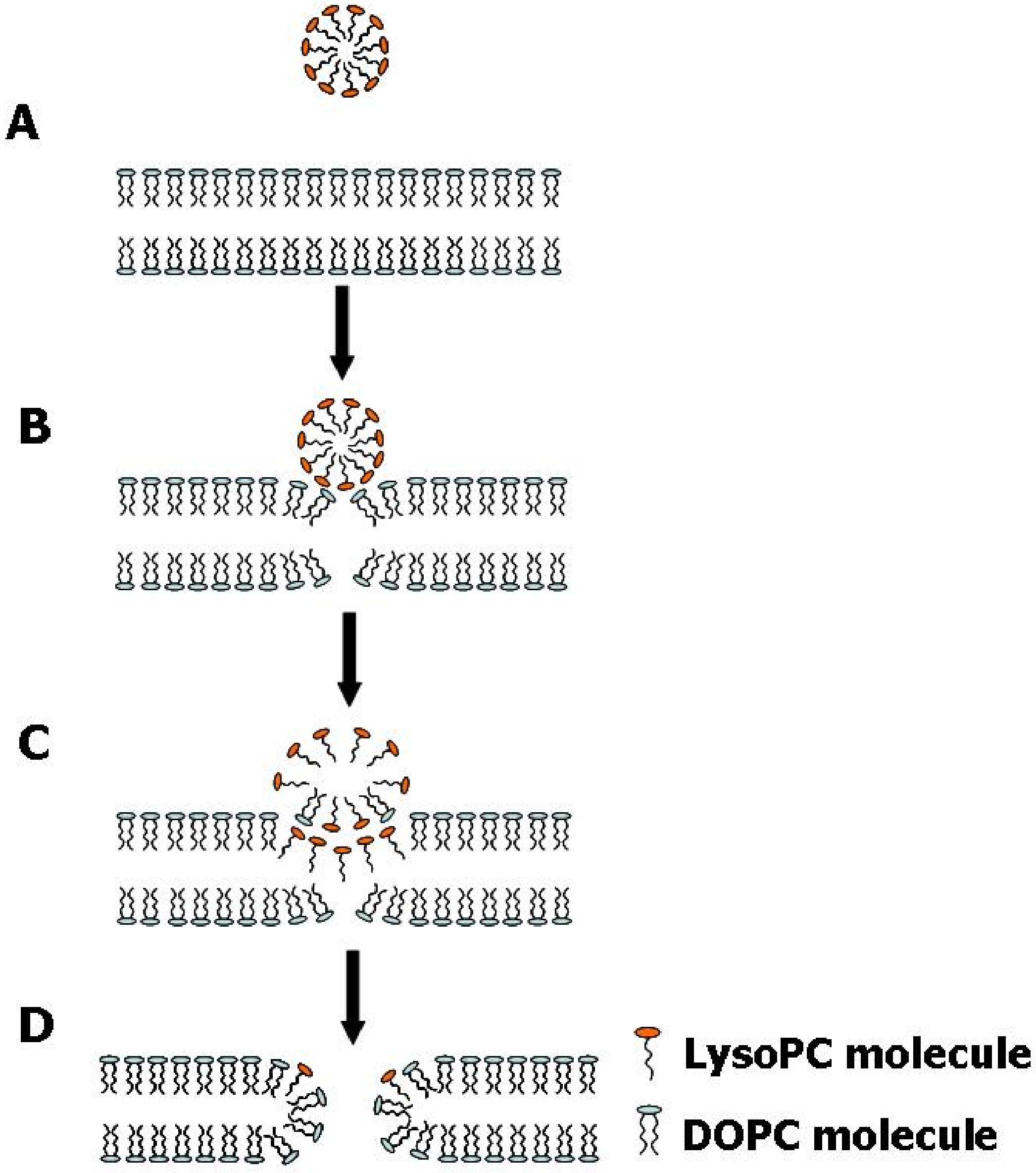

Figure 5.12. Schematic depiction of LysoPC micelle interactions with intact DOPC vesicles adsorbed onto NC surfaces. (A) Addition of LysoPC, (B) initial contact of LysoPC with DOPC bilayer, (C) exchange of two lipid monomers and (D) breakage of vesicle membrane.

5.5 Conclusions

In summary, interactions between DOPC lipid vesicles and regenerated or nanocrystalline cellulose surfaces were studied. QCM-D, SPR and *in-situ* AFM results indicated that partially covered lipid layer structures formed over regenerated cellulose films while unruptured vesicle layers assembled onto nanocrystalline cellulose surfaces. The higher water content (84 ± 5%) of DOPC structures on NC films was attributed to the large amount of trapped water between unruptured vesicles and inside vesicles while the degrees of hydration for phospholipid patches over RC surfaces were 31 ± 6%. Large aggregates of intact DOPC vesicles were observed on top of the NC surfaces in AFM height and phase images. For RC films, smoother surface structures of disconnected DOPC islands with smaller features were observed in height images. The existence of lipid patches was unambiguously resolved by the strong contrast between DOPC bilayers and the underlying RC films in phase images. By measuring DOPC vesicle adsorption onto cellulose films with various thicknesses, it was found that phospholipids only adsorbed onto the top of the films rather than partially penetrating into either the porous NC or non-porous RC films. Micelles of LysoPC, known for their ability to induce cell membrane rupture, were employed to promote the transformation of DOPC vesicles into multilayer structures on the NC substrate. The great decrease of the mass, dissipation change and degree of hydration for the lipid structures after exposure to LysoPC corresponded to the conversion of floppy vesicle layer to a more rigid DOPC lamellar structure. Resonance angle changes for SPR signals indicated that the uptake of LysoPC by vesicles lasted for 200 seconds with a maximal increase of 14% by mass prior to membrane collapse. The vesicle breakage consistent with the huge drop in degree of hydration led to a multilayer structures composed of ~ 4 phospholipid layers on the NC surfaces. Images from AFM showed the phospholipid multilayers completely covered the NC films. These results are consistent with the proposed mechanism of LysoPC action,[14-16] where LysoPC micelles exchange LysoPC molecules with intact DOPC vesicles. As LysoPC concentrations build in the DOPC vesicles, intimate contact between headgroups of the two types of lipids presumably lower the energy barrier associated with fusion that inhibits the conversion of intact vesicles to planar conformations. In this chapter we showed how to prepare biomimetic cell membranes in the conformations of both vesicle layers and planar structures on cellulose surfaces. These polymer-supported phospholipid layers will be useful for future studies of intact and ruptured protoplast systems to study aspects of plant cell wall self-assembly in a native system.

5.6 References:

(1) Sackmann, E. *Science*, **1996**, *271*, 43-48.

(2) Tanaka, M.; Sackmann, E. *Nature* **2005**, *437*, 656-663.

(3) Dupuy, A. D.; Engelman, D. M. *Proc. Natl. Acad. Sci. U. S. A.* **2008**, *105*, 2848–2852.

(4) Alberts, B.; Johnson, A.; Lewis, J.; Raff, M.; Roberts, K.; Walter, P. Molecular Biology of the Cell, 4th Ed., Garland Science, New York, 2002.

(5) Yennawar, N. H.; Li, L.; Dudzinski, D. M.; Tabuchi, A. ; Cosgrove, D. J. *Proc. Natl. Acad. Sci. U. S. A.* **2006**, *103*, 14664-14671.

(6) Schaub, M.; Wenz, G.; Wegner, G.; Stein, A.; Klemm, D. *Adv. Mater.* **1993**, *5*, 919-922.

(7) Buchholz, V.; Wegner, G.; Stemme, S.; Ödberg, L. *Adv. Mater.* **1996**, *8*, 399-402.

(8) Kontturi, E.; Thüne, P. C.; Niemantsverdriet, J. W. *Langmuir* **2003**, *19*, 5735-5741.

(9) Edgar, C. D.; Gray, D. G. *Cellulose* **2003**, *10*, 299-306.

(10) Beck-Candanedo, S.; Roman, M.; Gray, D. G. *Biomacromolecules* **2005**, *6*, 1048-1054.

(11) Ahola, S.; Salmi, J.; Johansson, L. S.; Laine, J.; Österberg, M. *Biomacromolecules* **2008**, *9*, 1273-1282.

(12) Wiegand, G.; Jaworek, T.; Wegner, G.; Sackmann, E. *Langmuir* **1997**, *13*, 3563-3569.

(13) Keller, C. A.; Glasmastar, K.; Zhdanov, V. P.; Kasemo, B. *Phys. Rev. Lett.* **2000**, *84*, 5443-5446.

(14) Cho, N.; Wang, G.; Edvardsson, M.; Gleen, J. S.; Hook, F.; Frank, C. W. *Anal. Chem.* **2009**, *81*, 4752-4761.

(15) Needham, D.; Stoicheva, N.; Zhelev, D. V. *Biophysical Journal* **1997**, *73*, 2615-2629.

(16) Hamai, C.; Yang, T.; Kataoka, S.; Cremer, P. S.; Musser, S. M. *Biophysical Journal* **2006**, *90*, 1241-1248.

(17) Hamai, C.; Cremer, P. S.; Musser, S. M. *Biophysical Journal* **2007**, *92*, 1988-1999.

(18) Lee, S. D.; Na, Y. J.; Lee, S. D. *Langmuir* **2009**, *25,* 5421-5425.

(19) Voinova, M. V.; Rodahl, M.; Jonson, M.; Kasemo, B. *Phys. Scr.* **1999**, *59*, 391-396.

(20) Sauerbrey, G. *Z. Phys.* **1959**, *155*, 206-22.

(21) Bottom, V. E. *Introduction to Quartz Crystal Unit Design*; Van Nostrand Reinhold Co.: New York, 1982.

(22) Dorvel, B. R.; Keizer, H. M.; Fine, D.; Vuorinen, J.; Dodabalapur, A.; Duran, R. S. *Langmuir* **2007**, *23*, 7344–7355.

(23) Hianik, T.; Vitovic, P.; Humenik, D.; Andreev, S. Y.; Oretskaya, T. S.; Hall, E. A. H.; Vadgama, P. *Bioelectrochemistry* **2003**, *59*, 35-40.

(24) Kittle, J. D.; Du, X.; Jiang, F.; Qian, C.; Roman, M.; Heinze, T.; Esker, A. R. *Biomacromolecules,* **2011**, *12*, 2881-2887.

(25) Kaya, A.; Du, X.; Liu, Z.; Lu, J. W.; Morris, J. R.; Glasser, W. G.; Heinze, T.; Esker, A. R. *Biomacromolecules* **2009**, *10*, 2451-2459.

CHAPTER 6

Cholesterol Effects on Phospholipid Vesicle Interactions with Cellulose Surfaces

6.1 Abstract

Surface plasmon resonance, quartz crystal microbalance with dissipation monitoring and *in situ* atomic force microscopy experiments revealed the role of cholesterol in phospholipid interactions with model cellulose surfaces. Pure phospholipid and phospholipid with low cholesterol contents formed disconnected lipid islands on regenerated cellulose (RC) surfaces while supported vesicular layers formed over RC surfaces with high cholesterol content (≥ 6.3% by mole). The inhibition of vesicle rupture was attributed to the ability of cholesterol to relax the stresses of the intact vesicle to accommodate vesicle deformation. Compared to regenerated cellulose surfaces, the formation of vesicle layers on silica surfaces required the percentage of cholesterol in the vesicle membrane to be ≥ 55% by mole. By comparing the dry mass and wet mass of phospholipid structures, the degree of hydration for phospholipid patches and vesicle layers on regenerated cellulose surfaces were seen as ~ 30% and ~ 70% by mass, respectively. In contrast, intact vesicles were always observed for phospholipid/cholesterol blends on nanocrystalline cellulose (NC) surfaces despite the increased cholesterol content. This was explained by the reduced mobility and fluidity of phospholipid molecules via interactions with cholesterol molecules buried within the vesicle membrane. The highly hydrated vesicle layers that adsorbed onto NC surfaces had even higher degrees of hydration ~ 80% by mass.

6.2 Introduction

The properties and functions of cellular membranes have attracted tremendous research interest in recent decades. Stable membrane structures not only protect cells from the outside environment but also contain selective transport channels for metabolites and ions.[1] Apart from phospholipids, the main component in the cell membrane, cholesterols are universally present in plasma membranes and regulate the stiffness or rigidity of lipid bilayers by altering the lateral movement of phospholipid molecules.[2-5] Cholesterols in the membrane also play an important role in accommodating vesicle deformation and resisting mechanical fatigue.[6,7] Force-distance curves measured by atomic force microscopy (AFM) for the effect of cholesterol on egg yolk phosphatidylcholine vesicles showed cholesterol increased the Young's and bending modula several-fold.[8] The presence of cholesterol was observed to decrease the transport rate of K^+, Na^+, Cl^-, glucose[9] and organic cations across the biomimetic membrane, but enhanced permeability towards organic anions.[10] Other studies have shown that the rafts made by cholesterol domains in liquid phase cell membranes were responsible for the recruitment and generation of certain trans-membrane proteins.[11,12] By comparing the behavior of the mixed phospholipid/cholesterol bilayers to the properties of the pure phospholipid bilayers, numerous characterization tools including quartz crystal microbalance with dissipation monitoring (QCM-D),[13] AFM,[8,14] scanning tunneling microscopy (STM),[15,16] neutron reflectivity[17,18] and second harmonic generation[19] were employed to investigate the effect of cholesterol on the structure of supported lipid membrane. To make the study of complex membrane structure more easily detectable and straightforward, 1,2-dioleoyl-sn-glycero-3-phosphocholine (DOPC),[20-22] with a low melting temperature ($T_m \sim -20$ °C), was frequently used. The chosen molecules with long acyl chains and unsaturation are believed to pack tightly with cholesterols to form raft domains in the liquid-ordered phase.[12]

Supported lipid membranes on polymer films serve as biomimetic membranes to study peptide-membrane interactions, lipid lateral mobilities, phase behavior and other membrane-related properties.[23,24] As the main component of plant cell walls, cellulose fibers have been noted for their interactions with cell membranes.[25,26] Lipid bilayers can be deposited onto model cellulose surfaces through horizontal Langmuir transfer.[27] In Chapter 5, it was observed that partially covered lipid layer structures formed over regenerated cellulose (RC) films through direct fusion process while unruptured vesicle layers assembled onto nanocrystalline cellulose (NC) surfaces.[28] In this chapter, various compositions of phospholipid/cholesterol mixtures were employed to study the interactions of DOPC/Cholesterol vesicles with two different cellulose surfaces, RC and NC through a combination of QCM-D, surface plasmon resonance (SPR) and *in-situ* AFM experiments. Partially covered lipid layer structures were observed for the adsorption of DOPC vesicles with low cholesterol content onto RC surfaces, whereas mixtures with high cholesterol content favored the adsorption of intact vesicles. It was also observed that cholesterol had little effect on the interactions of lipid/cholesterol vesicles with NC surfaces. These results provide information on the effects sterols have on phospholipid vesicle interactions with model cellulose surfaces.

6.3 Experimental

Cholesterol and DOPC in chloroform were purchased from Avanti Polar Lipids (Alabaster, AL). Lipids and cholesterol were mixed in various ratios in chloroform. The molar percentages of cholesterol in the prepared mixture were 0, 3.5, 6.3, and 11.9%. These blend systems will be abbreviated as DOPC, DOPC/Chol_3.5%, DOPC/Chol_6.3% and DOPC/Chol_11.9%. Chloroform was then removed under nitrogen until a thin film formed at the bottom of the vials. The residual solvent was evaporated by vacuum oven drying (25 Torr, 50 ˚C) for 3 hours. Ultrapure water was then added to the dried phospholipid or lipid/cholesterol until the lipid concentration of 250 mg•L^{-1} was achieved. The resulting liposome solution was sonicated until it became clear. Procedures for the preparation of NC and RC films, SPR measurements, QCM-D measurements and *in situ* AFM imaging were described in Chapter 3.3, and 3.4, respectively.

6.4 Results and Discussion

6.4.1 Adsorption onto Model Surfaces by QCM-D

Representative frequency (Δf) and dissipation changes (ΔD) for the seventh overtone ($n = 7$) by QCM-D measurements are shown in Figure 6.1. Each experiment was carried out as least twice to reproduce the results. The cellulose surfaces were equilibrated in water for 1 hour until a flat baseline was achieved. Next, a 250 mg•L^{-1} aqueous solution of DOPC or a DOPC/cholesterol mixture as was flowed over the cellulose surfaces. The adsorption of DOPC and DOPC/Chol_3.5% onto RC surfaces yielded a frequency decrease of ($\Delta f/n$) = -14 Hz for $n = 7$ with a dissipation change slightly greater than 1.7×10^{-6} for $n = 7$. This indicated that lipid vesicles adsorbed onto RC surfaces and spontaneously formed a rigid layer structure. In contrast, lipid mixtures with higher cholesterol contents (DOPC/Chol_6.3% and DOPC/Chol_11.9%) strengthened the vesicles which consequently led to the adsorption of intact vesicles as seen by a scaled frequency decrease of about -75 Hz for $n = 7$ with a dissipation change around 11.8×10^{-6} for $n = 7$. The immediate signal change was consistent with rapid liposome adsorption onto the cellulose surfaces. Larger shifts in ($\Delta f/n$) and ΔD indicated intact vesicles remained on the surface after rinsing. Major contributions to the substantial acoustic mass and dissipation changes came from trapped water in the interstices between unruptured vesicles and inside vesicles which was mechanically coupled to the RC surfaces.[29] The difficulties with vesicle rupture were mainly attributed to the ability of cholesterol to accommodate vesicle deformation on the cellulose surfaces.[6-8,13] The cholesterol molecules buried in the chain region of the bilayers reduce the curvature and stresses of the intact vesicles.[30]

On the other hand, adsorption of DOPC aqueous solution with different amounts of cholesterol onto NC surfaces showed almost the same behavior (Figure 6.2). For example, a larger scaled frequency decrease, $(\Delta f/n) = -244$ Hz for $n = 7$, and dissipation increase, $\Delta D = 46\times10^{-6}$, were observed for pure DOPC after water flushing. This adsorption was indicative of intact DOPC vesicle adsorption onto the NC surfaces. The curves for vesicle adsorption onto cellulose surfaces were fit by a Voigt-based viscoelastic model[29] which uses dissipation and frequency changes to obtain mass changes. The high overtone orders ($n=5$, 7 and 9) were used for estimation while low overtones such as $n=1$ and 3 were neglected because of insufficient energy trapping.[31] Detailed parameters for DOPC and DOPC/cholesterol liposome adsorption onto cellulose films are given in Tables 6.1 and 6.2.

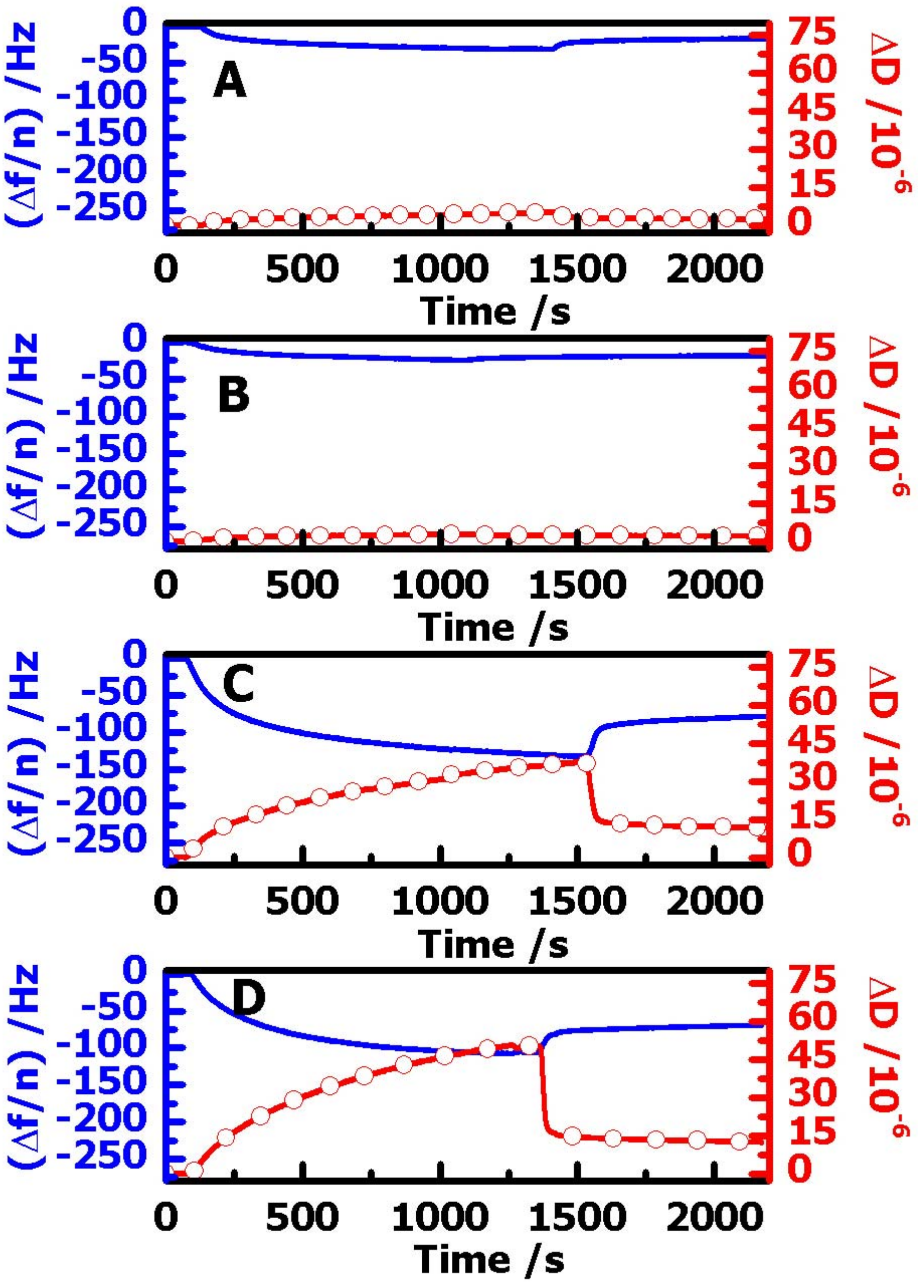

Figure 6.1. Representative (Δf/n) (blue lines) and ΔD (red lines with circles) for n = 7 vs. time for DOPC and DOPC/cholesterol liposome adsorption onto RC films. Graphs (A) through (D) correspond to DOPC, DOPC/Chol_3.5%, DOPC/Chol_6.3% and DOPC/Chol_11.9%, respectively. Water was flowed through the QCM-D module prior to and after adsorption.

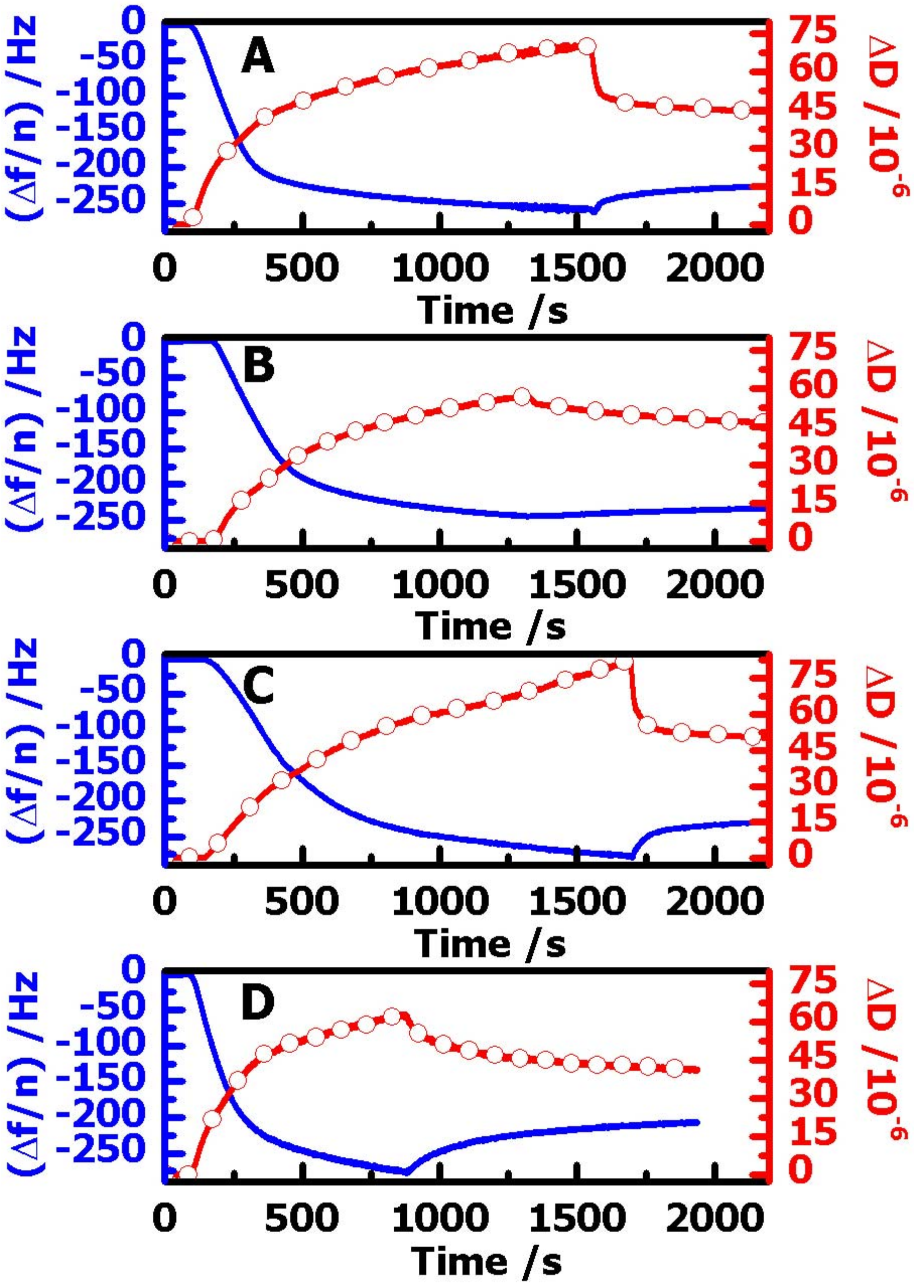

Figure 6.2. Representative ($\Delta f/n$) (blue lines) and ΔD (red lines with circles) for n = 7 vs. time for DOPC and DOPC/cholesterol liposome adsorption onto NC films. Graphs (A) through (D) correspond to DOPC, DOPC/Chol_3.5%, DOPC/Chol_6.3% and DOPC/Chol_11.9%, respectively. Water was flowed through the QCM-D module prior to and after adsorption.

It was interesting to compare the effect cholesterol had on vesicle interactions with cellulose surfaces and another commonly used substrate: silica. Representative QCM-D data in the form of (Δf/n) and ΔD for DOPC/cholesterol liposome adsorption onto silica surfaces are shown in Figure 6.3. The formation of phospholipid bilayers on silica substrates via a fusion process has been attributed to direct vesicle-substrate interactions and intervesicular stresses between neighboring vesicles.[32] Generally, vesicles approach the surface followed by slight deformations once they contact the substrate. Vesicles rupture when a critical concentration of vesicles are present on the surface. Phospholipid layers spontaneously propagate until a fully covered bilayer forms. A bilayer of DOPC on a silica surface yields a frequency decrease of (Δf/n) ~ -25 Hz for n = 7 with a dissipation change ~ 0.5×10^{-6} for n = 7 after a water rinse. Even for vesicles containing 50% cholesterol by mole, (Δf/n) and ΔD values after the exposure of silica to vesicle solutions and a water rinse yielded values identical to single-component DOPC vesicles. Dramatic changes occurred at ~ 55% cholesterol by mole when (Δf/n) ~ -40 Hz for n = 7 and ΔD ~ 6×10^{-6} for n = 7. The larger dissipation change indicated a floppy vesicle film formed on the silica substrate. Further increases of cholesterol, *c.a.* 70% by mole, led to even greater (Δf/n) and ΔD changes prior to the water rinse, however, the final equilibrium values were similar to the 55% cholesterol by mole system. This irreversible adsorption of vesicles onto silica surfaces demonstrated the important role of cholesterols in accommodating vesicle deformations and reducing the stresses of the intact vesicles. Compared to the case of RC surfaces where the critical percentage of cholesterols in vesicles were much smaller, it implied greater interactions between DOPC headgroups and hydroxyl groups on the silica surfaces.

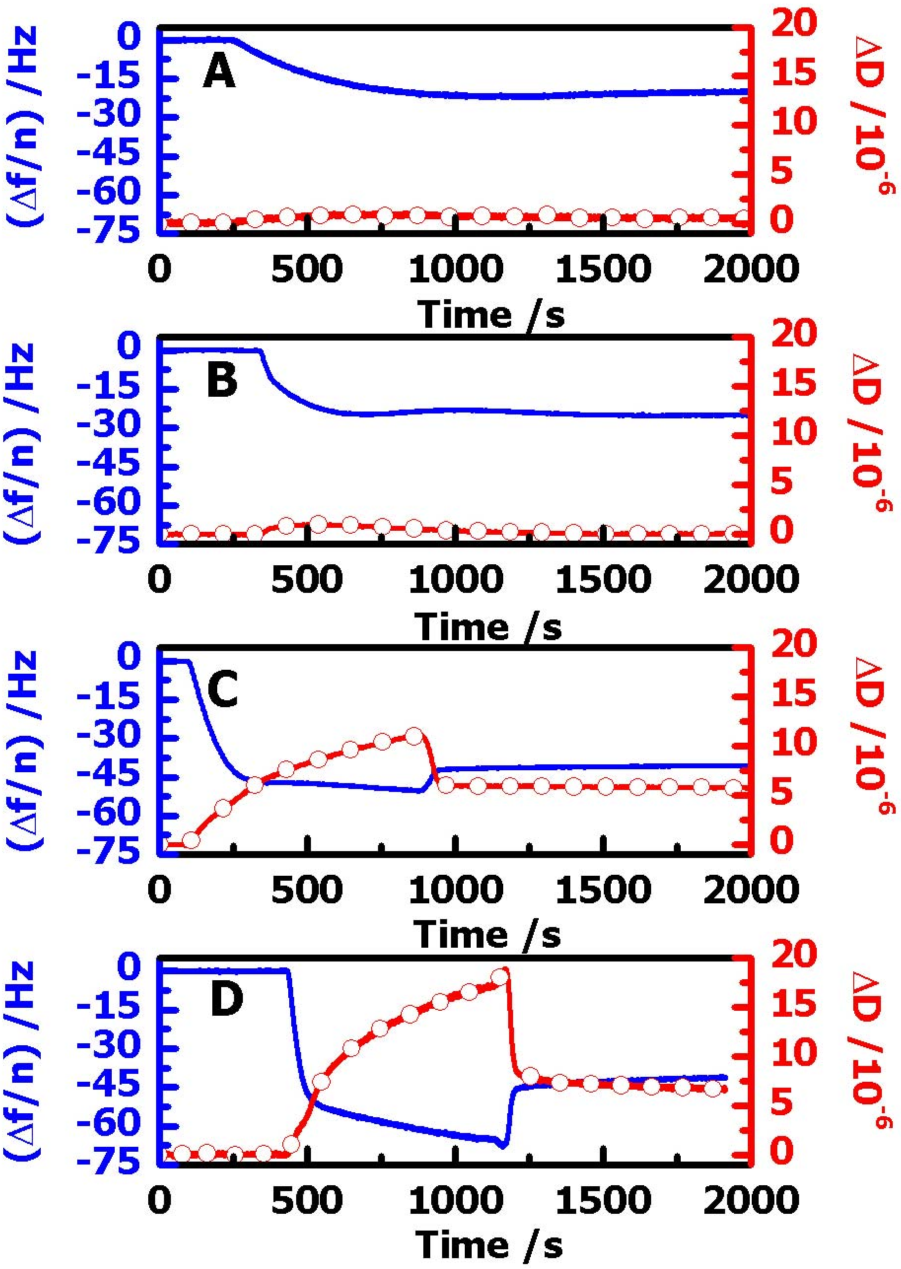

Figure 6.3. Representative (Δf/n) (blue lines) and ΔD (red lines with circles) for n = 7 vs. time for DOPC and DOPC/cholesterol liposome adsorption onto silica surfaces. Graphs (A) through (D) correspond to DOPC, DOPC/Chol_50%, DOPC/Chol_55% and DOPC/Chol_70%, respectively. Water was flowed through the QCM-D module prior to and after adsorption.

6.4.2 Adsorption onto Model Surfaces by SPR

The optical dry mass of DOPC/cholesterol structures adsorbed onto cellulose films was measured by SPR. Analysis of SPR data was described in Chapter 3.4.6. Each experiment was carried out at least twice with representative SPR curves provided in Figures 6.4 and 6.5. Surface excess (Γ) analysis was calculated through the equation of de Feijter et al.[33] The SPR results were consistent with the observations from QCM-D experiments where DOPC and DOPC/cholesterol gave similar adsorption onto NC surfaces. Eight times greater DOPC and DOPC/Chol_3.5% adsorption occurred onto NC films versus RC films. Higher amounts of cholesterols in DOPC vesicles (DOPC/Chol_6.3% and DOPC/Chol_11.9%) led to approximately 2× greater adsorption onto RC films than DOPC and DOPC/Chol_3.5%. Similar values for the maximum ($\Delta\theta_{max}$, prior to water flushing) and irreversible resonant angle changes ($\Delta\theta_{irr}$, after water flushing) of DOPC and DOPC/cholesterol adsorption onto cellulose films were indicative of completely irreversible adsorption. The combination of optical mass changes and acoustic mass changes deduced from SPR and QCM-D results, respectively, allowed for the calculation of the degrees of hydration of the adsorbed DOPC films.[34] The highly hydrated vesicle layers of DOPC that adsorbed onto NC surfaces had degrees of hydration greater than 82% by mass, whereas the degrees of hydration for DOPC and DOPC/Chol_3.5% structures adsorbed onto RC surfaces were only about 30% by mass. While the degrees of hydration were substantially different, there was still a significant amount of water associated with the bilayer structure. It was interesting to note that DOPC/Chol_6.3% and DOPC/Chol_11.9% films adsorbed onto RC surfaces also had high degrees of hydration ~ 70% by mass. This value is consistent with intact vesicles conformations on the RC substrates.

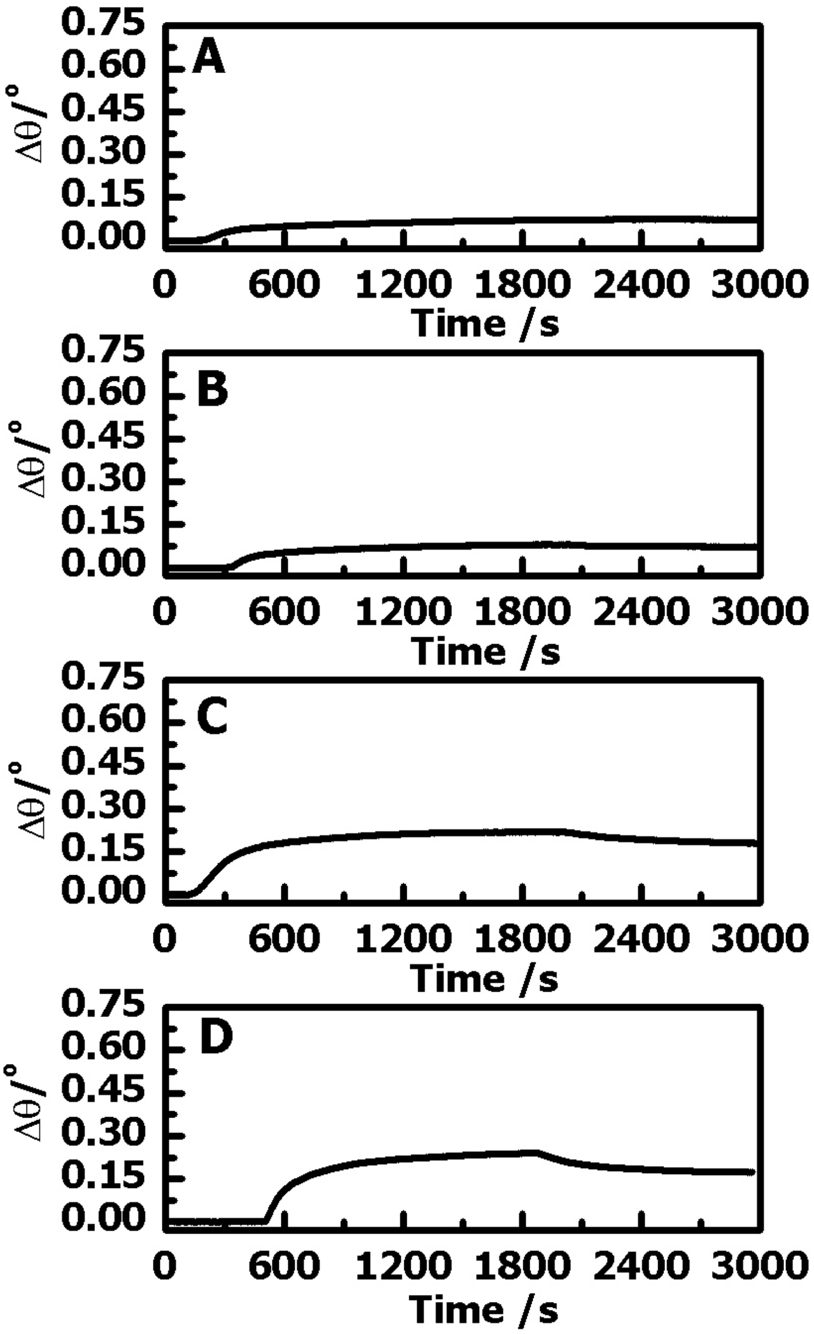

Figure 6.4. Representative SPR angle changes with time for DOPC and DOPC/cholesterol liposome adsorption onto RC films. Graphs (A) through (D) correspond to DOPC, DOPC/Chol_3.5%, DOPC/Chol_6.3% and DOPC/Chol_11.9%, respectively. Water was flowed through the SPR instrument prior to and after adsorption.

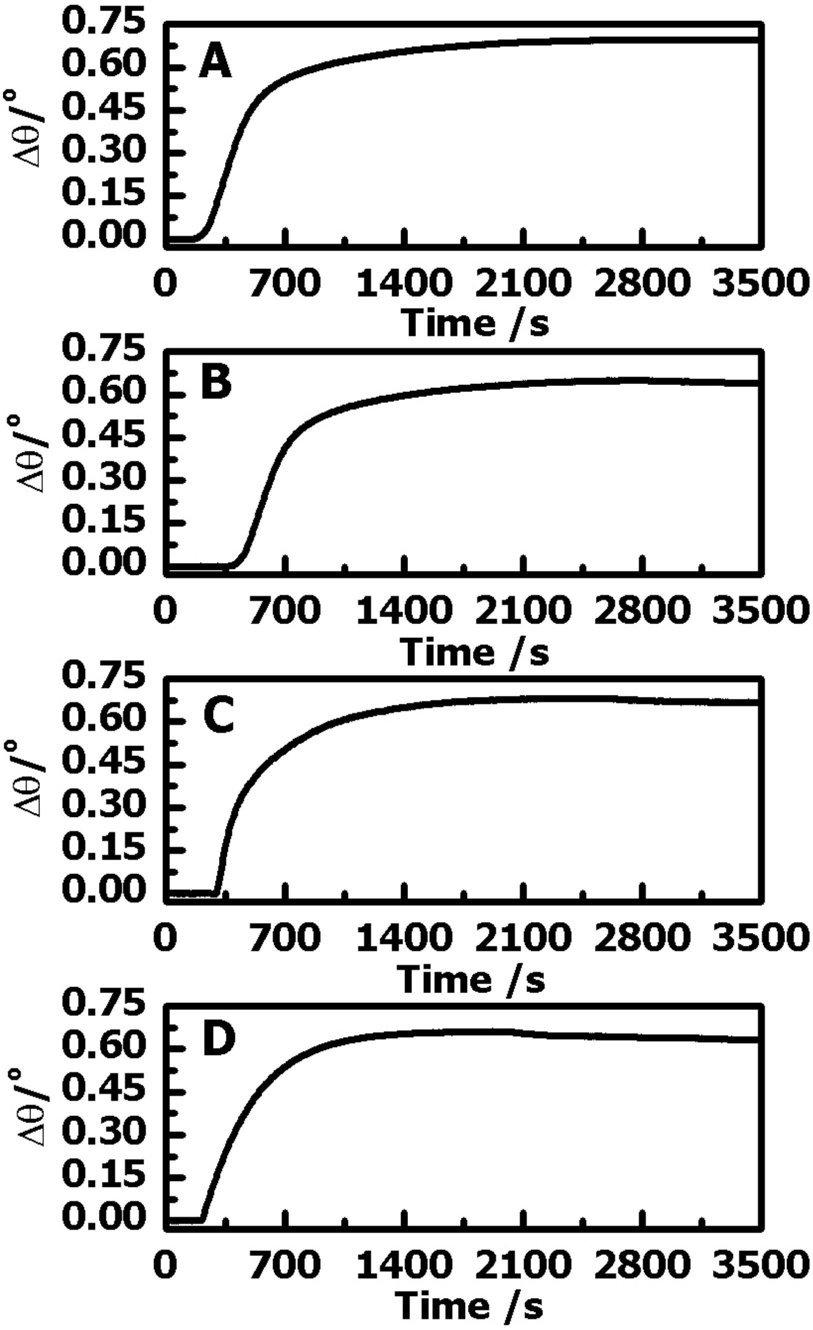

Figure 6.5. Representative SPR angle changes with time for DOPC and DOPC/cholesterol liposome adsorption onto NC films. Graphs (A) through (D) correspond to DOPC, DOPC/Chol_3.5%, DOPC/Chol_6.3% and DOPC/Chol_11.9%, respectively. Water was flowed through the SPR instrument prior to and after adsorption.

Table 6.1 Raw data for DOPC and DOPC/cholesterol adsorption onto RC and NC surfaces.[a]

	RC surfaces			NC surfaces		
	($\Delta f/n$) (Hz)	$\Delta D \times 10^6$	$\Delta\theta_{max}$ (°)	($\Delta f/n$) (Hz)	$\Delta D \times 10^6$	$\Delta\theta_{max}$ (°)
DOPC	-14 ± 1	1.7 ± 0.1	0.07 ± 0.01	-244 ± 9	46 ± 2	0.67 ± 0.04
DOPC/Chol_3.5%	-15 ± 1	1.6 ± 0.1	0.08 ± 0.01	-242 ± 10	47 ± 3	0.68 ± 0.03
DOPC/Chol_6.3%	-75 ± 5	11.8 ± 0.4	0.21 ± 0.01	-246 ± 8	45 ± 3	0.69 ± 0.04
DOPC/Chol_11.9%	-74 ± 4	12.1 ± 0.4	0.23 ± 0.01	-243 ± 10	45 ± 3	0.67 ± 0.03

[a] Errors represent one standard deviation.

Table 6.2 Parameters for DOPC and DOPC/cholesterol adsorption onto RC and NC surfaces.[a]

Adsorbates	RC surfaces			NC surfaces		
	Γ (mg•m^{-2})		%Degree of Hydration [b]	Γ (mg•m^{-2})		%Degree of Hydration [b]
	SPR	QCM-D		SPR	QCM-D	
DOPC	2.1 ± 0.4	3.0 ± 0.2	31 ± 6	16 ± 1	97 ± 4	84 ± 5
DOPC/Chol_3.5%	2.2 ± 0.3	3.2 ± 0.2	30 ± 5	17 ± 1	96 ± 6	83 ± 6
DOPC/Chol_6.3%	5.1 ± 0.2	22 ± 3	77 ± 10	17 ± 1	97 ± 3	82 ± 4
DOPC/Chol_11.9%	5.5 ± 0.3	22 ± 2	75 ± 8	17 ± 1	97 ± 6	83 ± 6

[a] Errors represent one standard deviation.

[b] %Degree of Hydration was calculated as $(1-\Gamma_{spr}/\Gamma_{QCM\text{-}D})\times 100\%$.[34]

6.4.3 AFM Studies of Lipid and Lipid/Cholesterol Adsorption onto Model Surfaces

Topologies of the solid/liquid interface for RC surfaces prior to and after exposure to 250 mg•L^{-1} aqueous solutions of DOPC and DOPC/cholesterol liposomes and a subsequent rinse with water were obtained from *in situ* AFM images provided in Figures 6.6 and 6.7. As seen in the height images in Figure 6.6, RC surfaces had relatively flat features in the height profile. After flushing with water to remove irreversibly adsorbed materials, disconnected lipid islands were observed on RC films after DOPC and DOPC/Chol_3.5% adsorption (Figure 6.6 B and D), whereas intact vesicles with spherical shapes were found for DOPC/Chol_6.3% and DOPC/Chol_11.9% ((Figure 6.6 F and H)) over RC surfaces. Planar lipid structures that formed on the RC surfaces led to slight surface roughness changes after DOPC and DOPC/Chol_3.5% adsorption. No induced fusion and corresponding membrane collapse were observed for DOPC/Chol_6.3% and DOPC/Chol_11.9% interactions with NC surfaces. The coverage of intact vesicles over RC resulted in a substantial increase of the root-mean-square (RMS) roughnesses from 0.9 nm to 1.4 nm for both DOPC/Chol_6.3% and DOPC/Chol_11.9%. Phase imaging in Figure 6.7 further confirmed the phospholipid structures adsorbed onto RC films. While the small surface roughness might prevent further identification of lipid layer structures formed over RC films, the strong phase contrast between bilayer patches of DOPC or DOPC/Chol_3.5% and underlying RC films in Figure 6.7 B&D facilitated unambiguous resolution of planar phospholipid structures on top of the RC surfaces. The even more pronounced phase contrast between intact vesicles and background cellulose films (Figure 6.7 F&H) clearly showed vesicle aggregates on top of the cellulose surfaces.

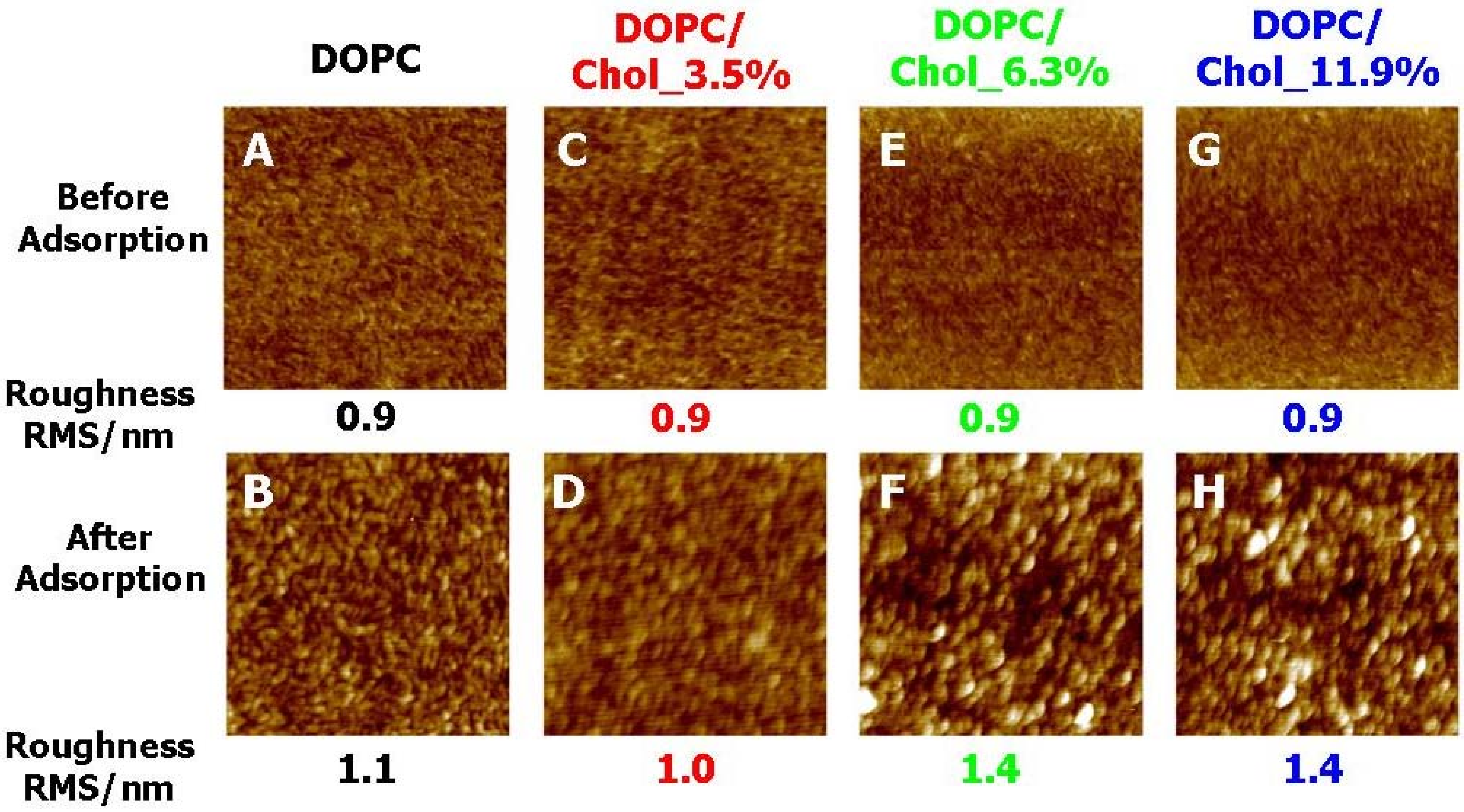

Figure 6.6. Representative AFM height images of the solid/liquid interface of RC surfaces prior to and after DOPC and DOPC/cholesterol liposomes adsorbed from 250 mg·L^{-1} bulk solutions. The AFM images are 2 μm x 2 μm and have Z-axis scales of 0 to 20 nm. Numbers under each picture are RMS surface roughnesses.

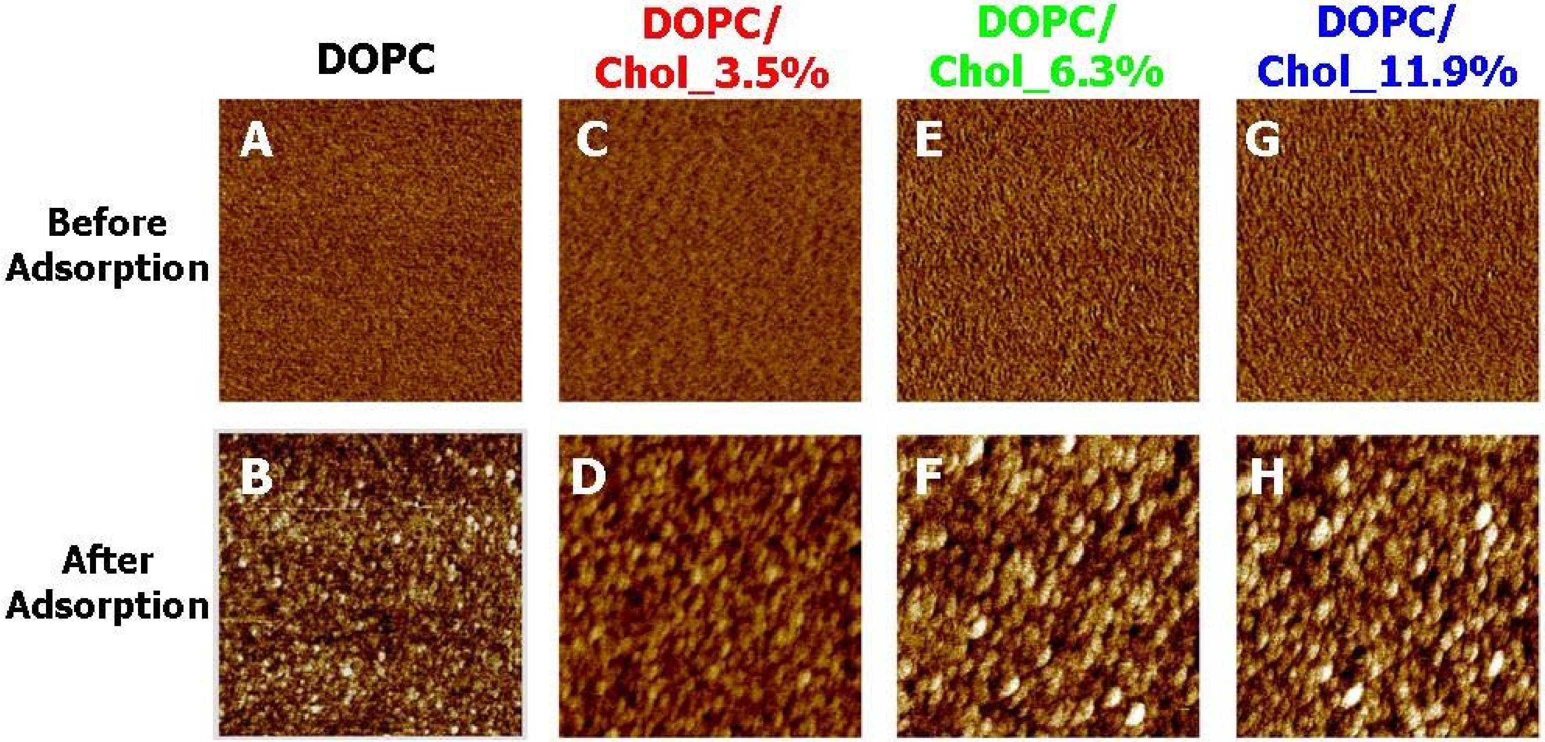

Figure 6.7. Representative AFM phase images of the solid/liquid interface for RC surfaces prior to and after DOPC and DOPC/cholesterol liposomes adsorbed from 250 mg·L^{-1} bulk solutions. The AFM images are 2 × 2 μm^2 and have Z-axis scales as 0 to 5 degrees.

Topologies of the solid/liquid interface for NC surfaces prior to and after exposure to 250 mg•L^{-1} aqueous solutions of DOPC and DOPC/cholesterol liposomes and a subsequent water rinses were obtained from *in situ* AFM images provided in Figures 6.8 and 6.9. Consistent with QCM-D and SPR measurements, DOPC and DOPC/Cholesterol adsorbed onto NC surfaces, masked the rod-like patterns of the underlying nanocrystals, and had conformations consistent with large vesicle aggregates. The RMS surface roughnesses of NC films after adsorption were greater than those prior to adsorption by at least a factor of 1.5. The fact that intact vesicle layers were always observed for lipid/cholesterol mixtures over NC surfaces regardless of the cholesterol content indicated cholesterol molecules buried within the vesicle membrane did not destabilize the vesicles. Table 6.3 summarizes the RMS roughnesses at the solid/liquid interface before and after DOPC and DOPC/cholesterol adsorption onto RC and NC surfaces for the images in Figures 6.6 and 6.8.

Table 6.3. RMS surface roughnesses at the solid/liquid interface before and after DOPC and DOPC/cholesterol adsorption onto RC and NC surfaces from 250 mg·L^{-1} aqueous solutions.

Model surfaces	RC		NC	
	Before (nm)	After (nm)	Before (nm)	After (nm)
DOPC	0.9	1.1	2.6	4.3
DOPC/Chol_3.5%	0.9	1.0	2.6	4.2
DOPC/Chol_6.3%	0.9	1.4	2.7	4.3
DOPC/Chol_11.9%	0.9	1.4	2.6	4.4

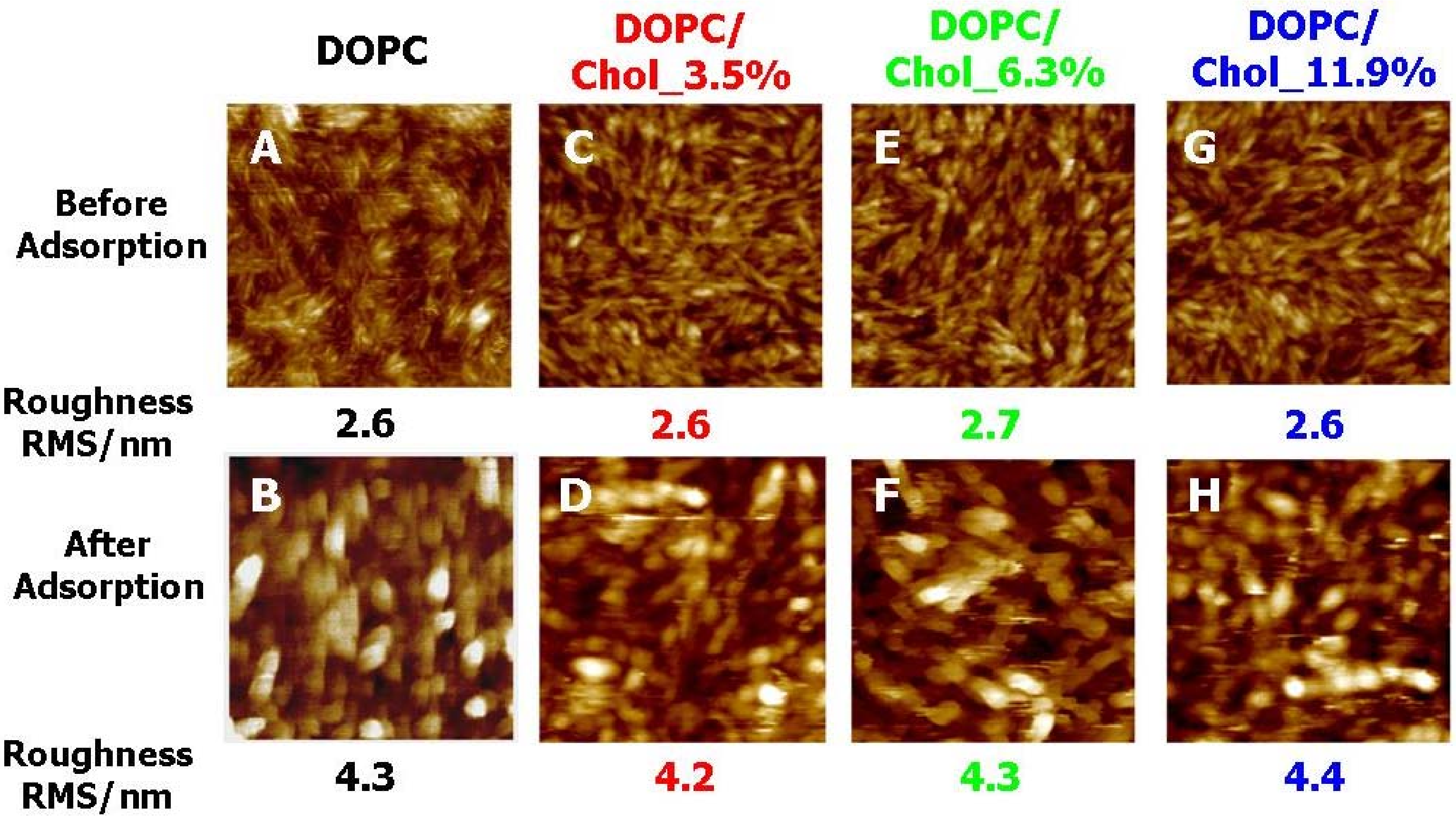

Figure 6.8. Representative AFM height images of the solid/liquid interface of NC surfaces prior to and after DOPC and DOPC/cholesterol liposomes adsorbed from 250 mg·L^{-1} bulk solutions. The AFM images are 2 μm x 2 μm and have Z-axis scales of 0 to 40 nm. Numbers under each picture are RMS surface roughnesses.

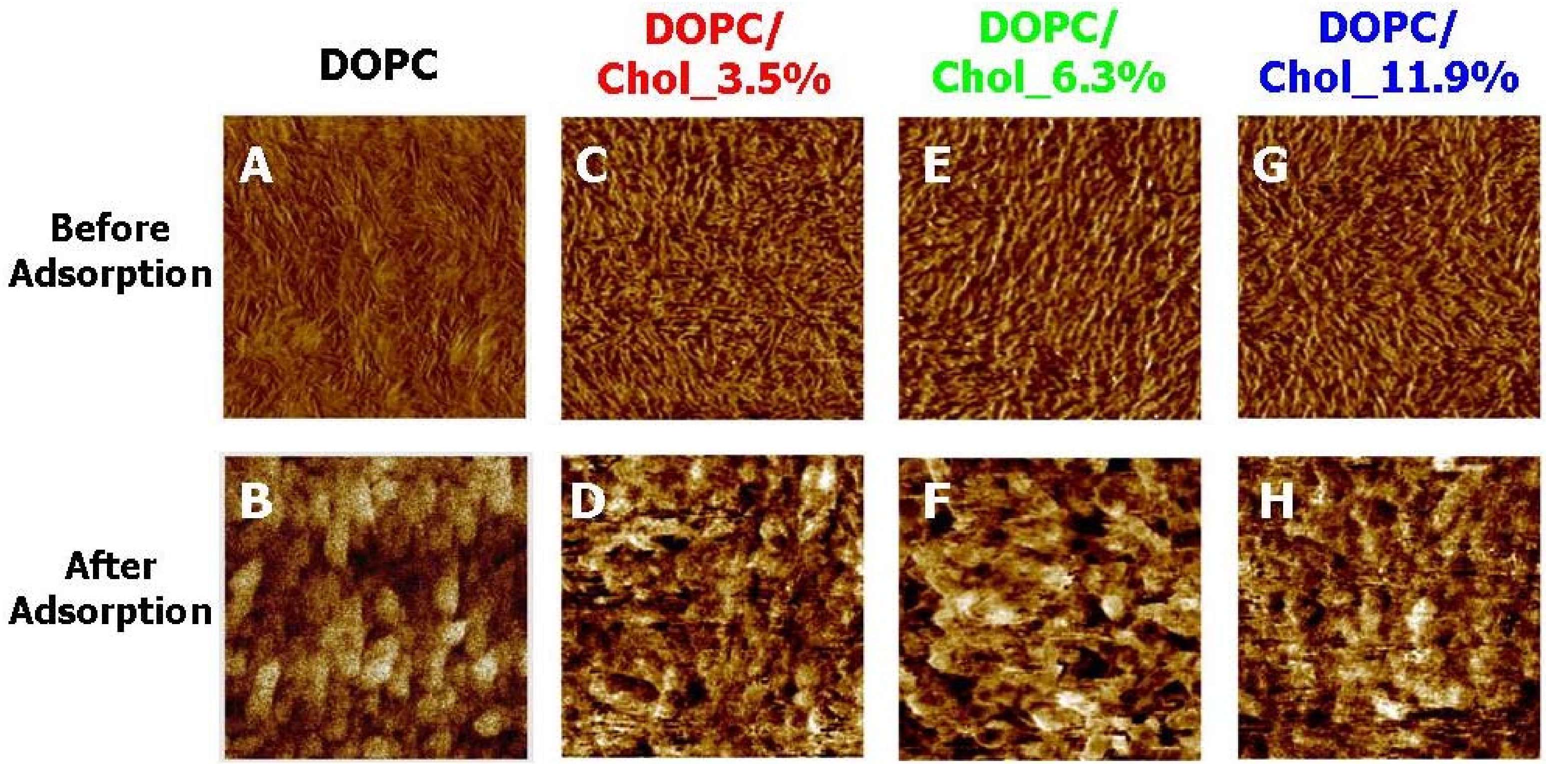

Figure 6.9 . Representative AFM phase images of the solid/liquid interface for NC surfaces prior to and after DOPC and DOPC/cholesterol liposomes adsorbed from 250 mg·L^{-1} bulk solutions. The AFM images are 2 × 2 μm^2 and have Z-axis scales of 0 to 10 degrees.

6.4.4 Mechanism for Cholesterol Effects on Vesicle Interactions with RC Surfaces

It was reported that cholesterol incorporation into the vesicle membrane had a tremendous impact on bilayer packing.[2-5] Below the gel-liquid transition temperature of DOPC (T_m ~ -20 °C), cholesterol enhanced the fluidity and intravesicle interactions of vesicles, while the mobility of the acyl chains of the phospholipid molecules were greatly restricted above T_m. Figure 6.10 illustrates the proposed mechanism of cholesterol action within vesicles over RC surfaces. The fusion of vesicle membranes on RC substrates were facilitated through both the interactions of DOPC headgroups with hydroxyl groups on top of the substrates and intervesicle stresses imposed by adjacent vesicles. The process of membrane breakage was divided into three steps: (a) vesicle flattening after adsorption onto substrates, (b) spontaneous rupture above a critical concentration of vesicles on the surface and (c) phospholipid layers forming a confluent membrane over the substrates.

When cholesterol molecules were buried in the bilayers, the hydrophilic 3β-OH headgroups of cholesterol molecules interacted with the carbonyl groups of phospholipid molecules through hydrogen bonding.[8] Meanwhile, the hydrophobic steroid portions of cholesterol were packed parallel to the acyl chains of the lipid molecules leading to further stability of the vesicle membrane. The interaction between the cholesterol and phospholipid bilayer were believed to play an important role in the increase of membrane cohesion, as confirmed by the enhanced Young’s and bending modula. The inhibition of vesicle rupture for DOPC/Chol_6.3% and DOPC/Chol_11.9% on RC surfaces were attributed to reduced vesicle deformation in the presence of cholesterol.

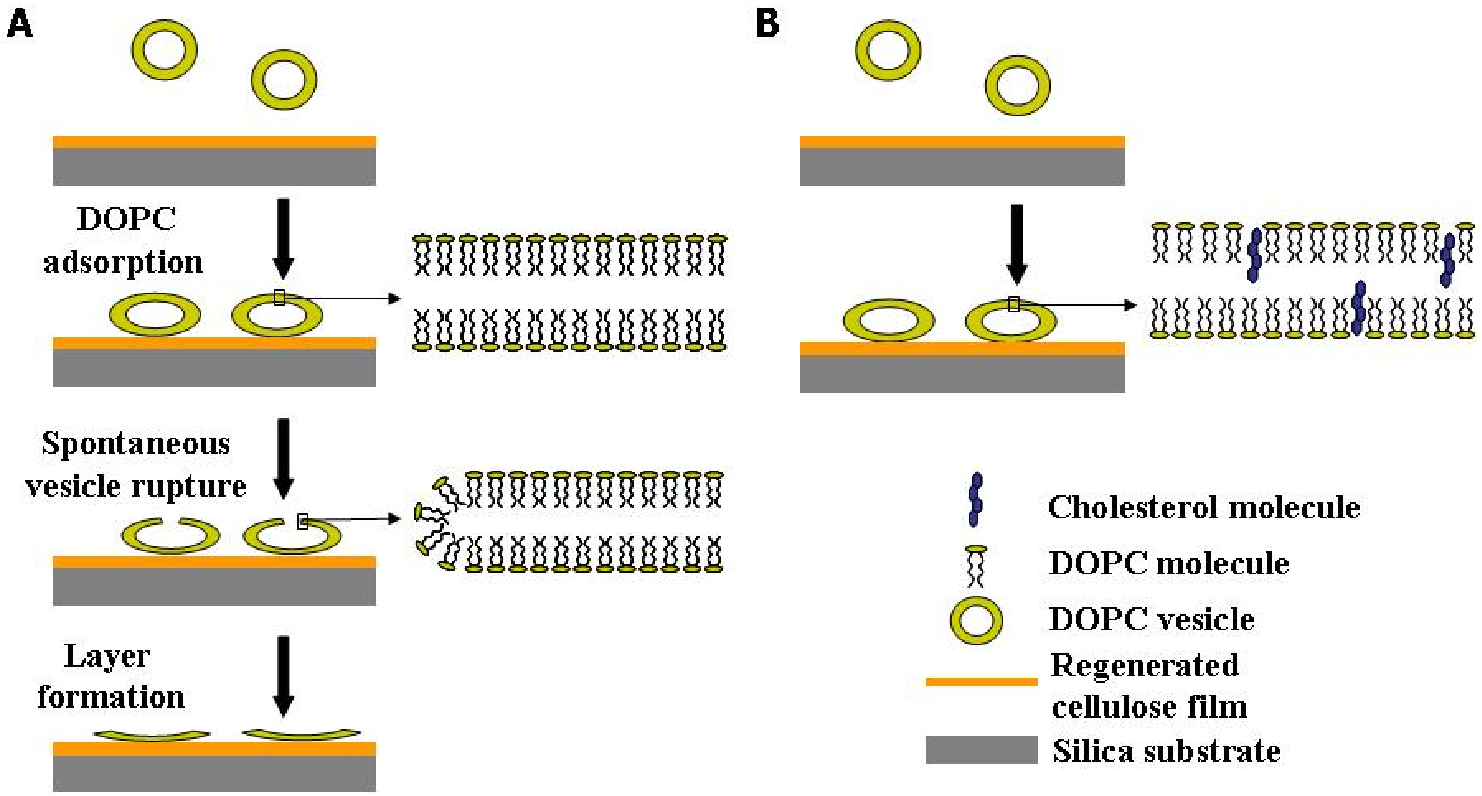

Figure 6.10 . Schematic depiction of DOPC and DOPC/cholesterol adsorption onto RC surfaces. (A) DOPC or DOPC/Chol_3.5% and (B) DOPC/Chol_6.3% or DOPC/Chol_11.9%.

6.5 Conclusions

In summary, interactions of phospholipid and phospholipid/cholesterol vesicles with regenerated or nanocrystalline cellulose films were investigated by QCM-D, SPR and *in-situ* AFM experiments. The adsorption of DOPC and DOPC/Chol_3.5% onto RC surfaces yielded small frequency decreases and dissipation changes. Disconnected lipid islands with strong phase contrast were observed in AFM height and phase images. This indicated that lipid vesicles adsorbed onto RC surfaces formed a rigid layer structure. Phospholipid mixtures with higher cholesterol contents (DOPC/Chol_6.3% and DOPC/Chol_11.9%) enhanced the rigidity (stiffness) of membrane structures whereby vesicles remained intact on the RC surfaces. Compared to silica surfaces where the critical percentage of cholesterol required to prevent vesicle fusion was ≥ 55% by mole, interactions between DOPC headgroups and RC surfaces were much weaker. Through the combination of SPR and QCM-D measurements, the degree of hydration for phospholipid patches and vesicle layers on RC surfaces were calculated as 30% and 70% by mass, respectively. While cholesterol affects the interactions of phospholipid/cholesterol vesicles with RC surfaces, intact vesicle layers were always observed for phospholipid/cholesterol mixtures over NC surfaces regardless of the cholesterol content. This further confirmed that cholesterol molecules buried within the vesicle membrane did not destabilize the vesicles. The highly hydrated vesicle layers that adsorbed onto NC surfaces had even greater degrees of hydration ~ 82% by mass. It was previously proposed that hydrogen bonding between the 3β-OH headgroups of cholesterol with the carbonyl groups of phospholipid molecules enhanced the integrity of vesicle structures while acyl chains of the phospholipid molecules were packed tightly with the steroid parts of cholesterol molecules within the vesicle membrane.[8] The present study illustrates how sterols influence phospholipid interactions with cellulose surfaces and will inform future work aimed at stabilizing cells on cellulose surfaces.

6.6 References:

(1) Karp, G., 2004. Cell and Molecular Biology: Concepts and Experiments, 4th ed. Wiley&Son (Chapter 4).

(2) Chen, M.; Li, M.; Brosseau, C. L.; Lipkowski, J. *Langmuir* **2009**, *25*, 1028-1037.

(3) Lipowski, R.; Sackmann, E., Eds. *Structure and Dynamics of Membranes*; Elsevier, Amsterdam, 1995.

(4) Yeagle, P. L. *Biology of Cholesterol*; CRC Press: Boca Raton, FL, 1988.

(5) Finegold, L. *Cholesterol and Membrane Models*; CRC Press: Boca Raton, FL, 1993.

(6) Lemmich, J.; Mortensen, K.; Ipsen, J. H.; Honger, T.; Bauer, R.; Mouritsen, O. G. *Eur. Biophys. J.* **1997**, *25*, 293-304.

(7) Yeagle, P. L. *Biochim. Biophys. Acta* **1985**, *822*, 267-287.

(8) Liang, X.; Mao, G.; Ng, K. Y. S. *Journal of Colloid and Interface Science* **2004**, *278*, 53-62.

(9) Papahadjopoulos, D.; Nir, S.; Ohki S. *Biochim. Biophys. Acta.* **1971**, *226*, 561–583.

(10) Szabo, G. *Nature* **1974**, *252*, 47– 49.

(11) Brown, D. A.; London, E. *Annu. Rev. Cell Dev. Biol.* **1998**, *14*, 111–136.

(12) Simons, K.; Ikonen, E. *Nature*, **1997**, *387*, 569–572.

(13) Sundh, M.; Svedhem, S.; Sutherland, D. S. *Phys. Chem. Chem. Phys.* **2010**, *12*, 453–460.

(14) Li, M.; Chen, M.; Sheepwash, E.; Brosseau, C. L.; Li, H.-Q.; Pettinger, B.; Gruler, H.; Lipkowski, J. *Langmuir* **2008**, *24*, 10313-10323.

(15) Xu, S.; Szymanski, G.; Lipkowski, J. *J. Am. Chem. Soc.* **2004**, *126*, 12276-12277.

(16) Sek, S.; Xu, S.; Chen, M.; Szymanski, G.; Lipkowski, J. *J. Am. Chem. Soc.* **2008**, *130*, 5736-5743.

(17) Burgess, I.; Szymanski, G.; Li, M.; Horswell, S. L.; Lipkowski, J.; Majewski, J.; Satija, S. *Colloids Surf. B. Biointerfaces* **2005**, *40*, 117-122.

(18) Burgess, I.; Szymanski, G.; Li, M.; Horswell, S. L.; Lipkowski, J.; Majewski, J.; Satija, S. *Biophys. J.* **2004**, *86*, 1763-1776.

(19) Yan, E. C. Y.; Eisenthal, K. B. *Biophys. J.* **2000**, *79*, 898-903.

(20) Bacia, K.; Schwille, P.; Kurzchalia, T. *Proc. Natl. Acad. Sci. U. S. A.* **2005**, *102*, 3272–3277.

(21) Baumgart, T.; Hess, S. T.; Webb, W. W. *Nature* **2003**, *425*, 821–824.

(22) Kaizuka, Y.; Groves, J. T. *Biophys. J.* **2004**, *86*, 905–912.

(23) Sackmann, E. *Science*, **1996**, *271*, 43-48.

(24) Tanaka, M.; Sackmann E. *Nature* **2005**, *437*, 656-663.

(25) Dupuy, A. D.; Engelman, D. M. *Proc. Natl. Acad. Sci. U. S. A.* **2008**, *105*, 2848–2852.

(26) Alberts, B.; Johnson, A.; Lewis, J.; Raff, M.; Roberts, K.; Walter, P. Molecular Biology of the Cell, 4th Ed., Garland Science, New York, 2002.

(27) Wiegand, G.; Jaworek, T.; Wegner, G.; Sackmann, E. *Langmuir* **1997**, *13*, 3563-3569.

(28) Du, X.; Roman, M.; Heinze, T.; Esker, A. R. *To be submitted.*

(29) Voinova, M. V.; Rodahl, M.; Jonson, M.; Kasemo, B. *Phys. Scr.* **1999**, *59*, 391-396.

(30) Leonard, A.; Escrive, C.; Laguerre, M.; Pebay-Peyroula, E.; Neri, W.; Pott, T.; Katsaras, J.; Dufourc, E. J. *Langmuir* **2001**, *17*, 2019-2030.

(31) Bottom, V. E. *Introduction to Quartz Crystal Unit Design*; Van Nostrand Reinhold Co.: New York, 1982.

(32) Keller, C. A.; Glasmastar, K.; Zhdanov, V. P.; Kasemo, B. *Phys. Rev. Lett.* **2000**, *84*, 5443-5446.

(33) De Feijter, J. A.; Benjamins, J.; Veer, F. A. *Biopolymers* **1978,** *17*, 1759-1772.

(34) Cho, N. J.; Wang, G.; Edvardsson, M.; Glenn, J. S.; Hook, F.; Frank, C. W. *Anal. Chem.* **2009,** *81,* 4752–4761.

CHAPTER 7

Overall Conclusions and Suggestions for Future Work

7.1 Overall Conclusions

This study focused on interactions between biomolecules and cellulose films with morphological differences at the mesoscopic scale. As the main components in plant cell walls, cellulose, hemicellulose, and lignin form a composite material via self-assembly. The study of natural materials such as the plant cell, informs future work aimed at the next generation of biomimetic nanocomposites. More importantly, nature creates this composite at the surface of plant cells, *i.e.* phospholipid bilayers. Nonetheless, the mechanism by which this occurs is poorly understood.[1] Sophisticated surface techniques such as surface plasmon resonance spectroscopy (SPR), quartz crystal microbalance with dissipation monitoring (QCM-D) and *in situ* atomic force microscopy (AFM) measurements have been employed to investigate how cellulose interacts with a synthetic mimic for a lignin-carbohydrate complex as well as phospholipid vesicles.

Pullulan cinnamate (PC) was used to mimic the lignin-carbohydrate complex. The interaction of PC with cellulose surfaces showed the cinnamate group, structurally similar to monolignols, strongly altered interactions between pullulan and cellulose. Pullulan modified with hydrophobic cinnamate groups not only covered the nanocrystalline cellulose (NC) surface but also penetrated into the porous film, which led to greater surface concentrations (Γ) relative to those observed on tightly packed regenerated cellulose (RC) films. By analyzing Γ as a function of film thickness (d), it was possible to show that Γ on NC surfaces came from two sources: an adsorbed layer on top of the NC surface that was similar to adsorption onto RC and partial penetration into the NC film (sorption) that was absent for the non-porous RC films. Even though NC films showed crystalline features, the fact that polysaccharide adsorption onto the top layer of NC and RC films was similar indicated the difference between amorphous and crystalline cellulose was not the main factor for greater adsorption. Film porosity led to apparent differences in adsorption between RC and NC films, *i.e.* accessible surface areas for NC films were greater than the corresponding RC film.

As a first step towards studying cells on cellulose surfaces, interactions of RC and NC surfaces with dioleoylphosphatidylcholine (DOPC) vesicles were probed. Large aggregates of intact vesicles adsorbed onto NC surfaces with high water contents ~ 84% by mass. Water trapped in the interstices between unruptured vesicles and inside vesicles themselves were mechanically coupled to the NC surfaces. This coupled water led to substantial mass and dissipation changes. In contrast, partial lipid layers with smooth features were found to assemble onto RC surfaces with a lower degree of hydration ~ 30% by mass. The use of a fusion agent, LysoPC, induced vesicle fusion for the DOPC/NC system. The mass, dissipation, and degree of hydration for the adsorbed DOPC vesicles after exposure to LysoPC all decreased in accord with a transformation from a vesicle to lamellar structure. The initial binding of LysoPC micelles onto vesicle membranes was observed with a maximal increase of 14% by mass prior to vesicle collapse. The destabilization of the spherical vesicle or the final rupture of membrane structure was attributed to the exchange between LysoPC monomers and phospholipid molecules. These polymer-supported phospholipid structures will serve as a starting point for studies of intact and ruptured protoplast systems.

Rafts made by cholesterol domains in liquid phase cell membranes are known to accommodate trans-membrane proteins and cell deformation. The role of cholesterol in phospholipid interactions with model cellulose surfaces was also probed in this study. Supported vesicle layers over RC surfaces were observed for vesicle membranes with cholesterol contents ≥ 6.3 mole%, whereas DOPC or DOPC with low cholesterol content formed disconnected lipid islands on RC surfaces. The intact vesicles on substrates were attributed to the ability of cholesterol to relax the stresses of membrane and accommodate vesicle deformation. Meanwhile, intact vesicles were always observed on NC surfaces for phospholipid/cholesterol blends regardless of the cholesterol content. This further confirmed that cholesterol molecules buried within the vesicle did not destabilize the vesicles. These results provide information on the influence of sterols on the interactions of phospholipid membranes with cellulose surfaces and may shed light on the role of lipid/sterol mixtures in the stability of plant cells.

7.2 Suggested Future Work

7.2.1 Immobilization of Protoplast Systems on Cellulose Surfaces

A transmembrane protein complex within plant cell membranes, cellulose synthase complex, has been noted for its capability to produce cellulose microfibrils from single glucose units.[2] However, the details of how cellulose microfibrils form through the cell membrane is still a myth. It is interesting to study the immobilization of bacterial (e.g. Gluconacetobacter xylinus) or protoplast cells onto the QCM-D substrates so that mass and dissipation changes of cellulose growth can be detected by QCM-D instrument. In our experiment, the bacterial strains ATCC 700718 were cultivated in Hestrin and Schramm (HS) medium.[3] In addition to the 20 $g \cdot L^{-1}$ carbon source (glucose), the medium contains 5 $g \cdot L^{-1}$ peptone, 5 $g \cdot L^{-1}$ yeast extract, 2.7 $g \cdot L^{-1}$ Na_2HPO_4, 1.2 $g \cdot L^{-1}$ citric acid and 5.7 $g \cdot L^{-1}$ $MgSO_4$. The final pH was adjusted to 5.0. The NC films were spincoated onto SAM-NH_2 surfaces with a spinning speed of 4000 revolutions per minute from 10 g·L^{-1} cellulose nanocrystal suspensions. After equilibrium in HS medium for more than 1 hour, G. Xylinus in HS medium was flowed over NC surface. Substantial adsorption of bacterial cells occurred immediately followed by switching back to HS medium to wash away reversibly adsorbed cells. The large scaled frequency (Δf/n) and dissipation changes (ΔD) indicated that a large amount of cells stuck to the cellulose surface (Figure 7.1). This model system including bacterial cells over supported polymeric film could provide a stable platform to study native cell wall growth on QCM-D sensors which are very sensitive to mass and dissipation changes.

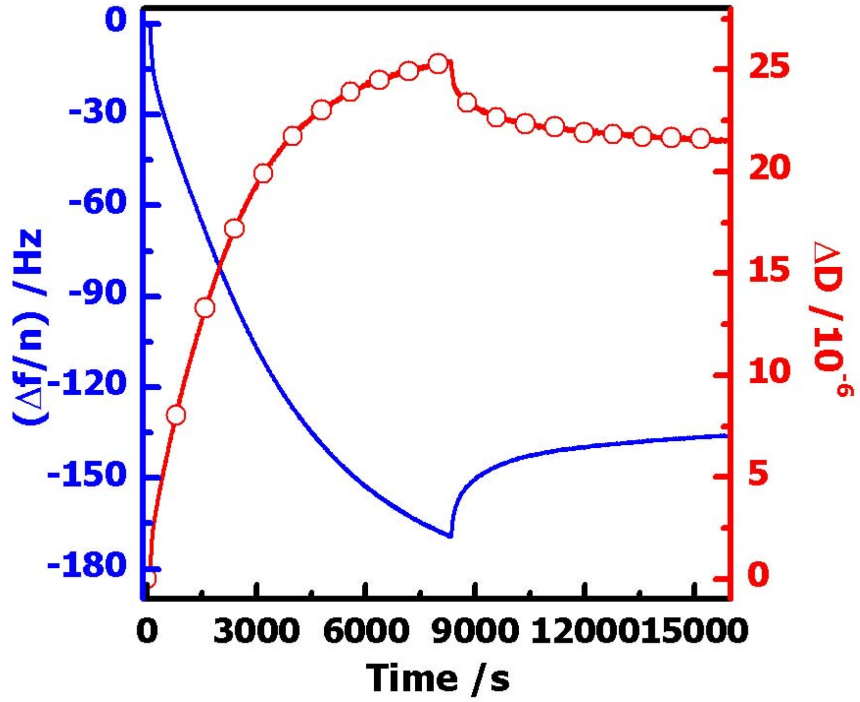

Figure 7.1. (Δf/n) (blue line) and ΔD (red line with circles) vs time for G. xylinus adsorption onto NC surfaces

7.2.2 Investigation of Vesicle Adsorption onto Pullulan Cinnamate Surfaces

Pullulan substituted with cinnamoyl groups can be used to mimic the lignin-carbohydrate complex in the secondary plant cell wall.[4,5] The interaction between phospholipid bilayer/cell membrane and lignin-carbohydrate structures can be studied by adsorption of vesicles onto PC surfaces. As the first step, PCs with different degrees of substitution (DS) by cinnamate groups were prepared as described in Chapter 3.1.1. However, PC chains cannot directly stick to the substrate. Therefore, the silylation of the pullulan backbones by trimethylsilyl (TMS) groups is indispensable. Detailed synthetic steps are shown in Figure 7.2. PC samples were first dissolved in N, N-dimethylacetamide (DMAc) at 60 °C. The TMS groups were attached to the pullulan chains by reaction with TMS-Cl and hexamethyldisilazane for 24 h. Tetrahydrofuran was added to the reaction flask with a precipitate forming at the bottom of the reaction flask. Methanol was used to precipitate and purify the product. The final TMSPC products in powder form were dried in a vacuum oven at 60 °C. PC films were prepared by spincoating TMSPC onto the substrate with a spinning speed of 4000 revolutions per minute from 10 $g \cdot L^{-1}$ TMSPC solutions in toluene. TMS groups can be removed by exposure to the vapor of 10% HCl by mass for 120 seconds.

DOPC vesicle adsorption from aqueous solution onto PC surfaces with two DS = 0.3 and 0.7 was investigated by QCM-D. Vesicles of DOPC adsorbed onto PC films with DS ~ 0.3 showed large scaled $(\Delta f/n) = -344$ Hz for the 7th overtone and $\Delta D = 56\times10^{-6}$. This significant adsorption implied that intact DOPC vesicles adsorbed onto the surface. Major contributions to the substantial acoustic mass and dissipation changes were from a large amount of trapped water in the interstices between unruptured vesicles and inside vesicles mechanically coupled to PC surfaces. On the other hand, adsorption of DOPC onto PC films with DS ~ 0.7 yielded $(\Delta f/n) = -13$ Hz for the 7th overtone with $\Delta D = 1.3\times10^{-6}$. Viscoelastic modeling gave a surface mass of

3.32 mg·m^{-2}. By taking into account of the average molecular weight of DOPC, the lipid molecular area, and a 30% degree of hydration, the surface mass of a well-ordered DOPC bilayer is 6.55 mg·m^{-2}. This would mean that PC ~ 0.7 surfaces favored the adsorption of a phospholipid monolayer. This observation was not surprising since a lipid monolayer could form on a hydrophobic surface by DOPC molecules adsorbing tails down. In the future, PC films with DS values between 0.3 and 0.7 could be prepared to study the transformation from vesicle to monolayer adsorption. *In situ* AFM would be useful to study the morphology change prior to and after phospholipid adsorption to differentiate between monolayer formation and the partial bilayers observed for RC surfaces in Chapters 5 and 6.

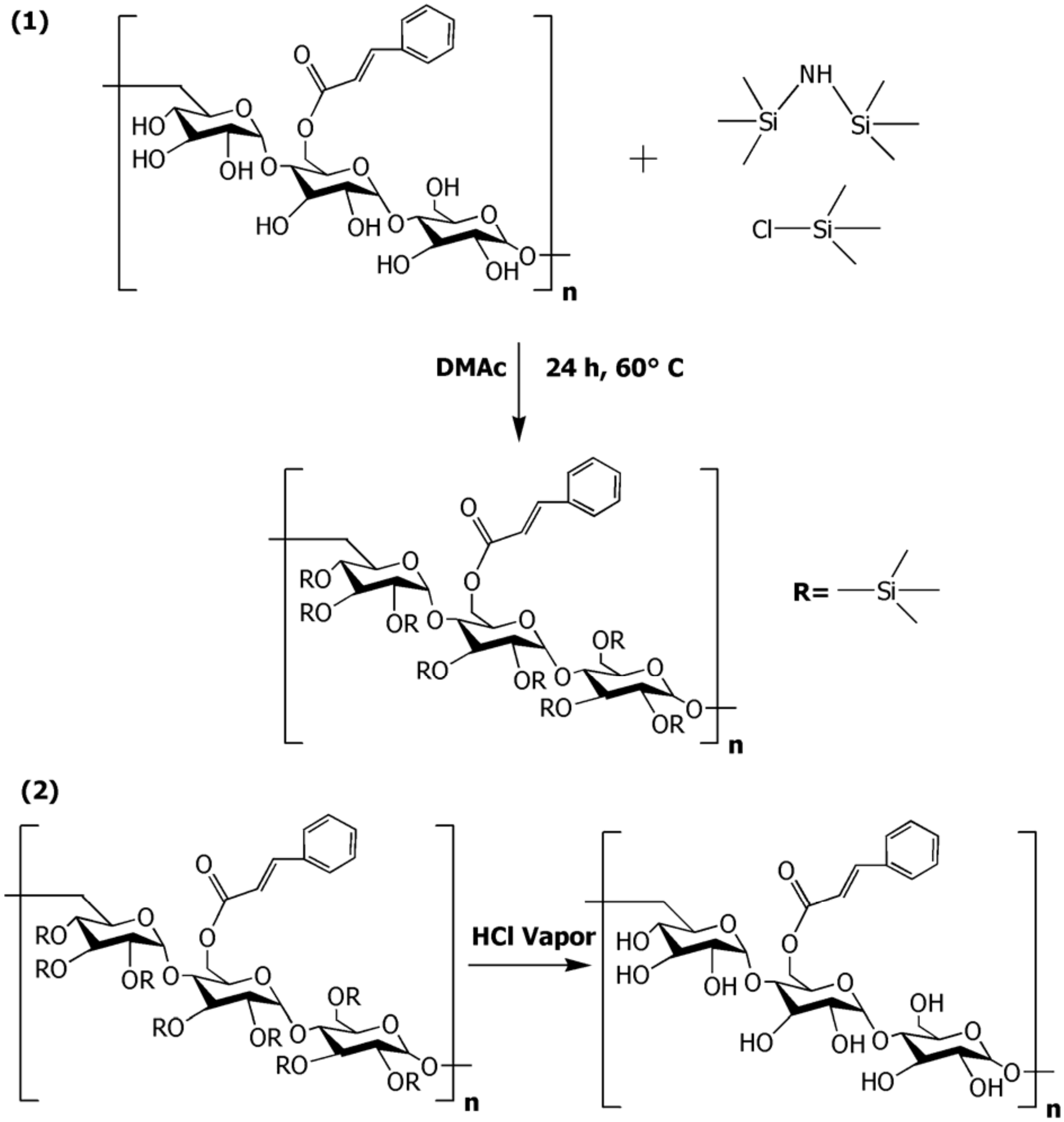

Figure 7.2. Synthetic route for (1) TMSPC and (2) hydrolysis to a PC film by HCl vapor.[6]

7.2.3 Curdlan Derivatives and Curdlan Films

Curdlan in aqueous media has a rod-like chain structure because of the β-1,3-glucosidic bonds.[7] The more rigid structures of curdlan compared to cellulose chains composed of β-(1-4) glucosidic bonds provide a good model to study the effects of anhydroglucose unit bonding on polymer conformation and interactions with other molecules. To make curdlan derivatives, such as curdlan triacid, it is important to note that curdlan only dissolves in alkaline solution and strongly polar solvents such as dimethyl sulfoxide (DMSO). As shown in Figure 7.3, dendron-like triester can be grafted onto curdlan backbones by a reaction with Weisocyanate in a 1:1 molar ratio.[8-10] DMSO was adopted as the reaction solvent due to its strongly polar character. The product was dialyzed in EtOH for at least 48 hrs. The brown colored powder was obtained by removing the ethanol by rotary evaporation. The tert-butyl groups of the curdlan triester were removed by reaction with trifluoroacetic acid at room temperature. The product was dialyzed in DI water for 3 days followed by freeze drying in a lyophilizer. The ionic triacid groups in curdlan yields a more extended chain structure in aqueous media due to electrostatic repulsive forces of neighboring negatively charged carboxyl groups.[11]

To make curdlan or curdlan triester films on substrate, TMS groups were added to the backbones of the polysaccharide. Curdlan samples were first dissolved in DMAc at 60 °C. The TMS groups were attached to the pullulan chains by reaction with TMS-Cl and hexamethyldisilazane for 24 h. Tetrahydrofuran was added to the reaction flask with precipitate at the bottom. Methanol was used to precipitate and purify the product. The final TMS-curdlan products obtained as powders were dried in a vacuum oven at 60 °C. Regenerated curdlan films were prepared by spincoating TMS-curdlan onto the substrate with a spinning speed of 4000 revolutions per minute from 10 $g{\cdot}L^{-1}$ TMS-curdlan solutions in toluene. TMS groups can be removed by exposure to the vapor of a 10% HCl by mass aqueous solution for 120 seconds.

Curdlan nanocrystals can also be prepared like cellulose nanocrystals in Chapter 3.1.3. The reaction was carried out by dissolving curdlan samples in sulfuric acid at 45 °C for 60 min. It was terminated by dilution of the reaction mixture with cold water. The sulfuric acid was removed from the curdlan suspension by three rounds of centrifugation at 4900 rpm for 15 minutes. The product was dialyzed against DI water until the pH was constant. The final suspension, was sonicated to separate curdlan aggregates and filtered through a 0.45 μm poly(vinylidene fluoride) syringe filter. Nanocrystalline curdlan films can be spincoated onto substrate with a spinning speed of 4000 rpm from 10 $g \cdot L^{-1}$ curdlan nanocrystal suspensions. The rigid backbone of curdlan chains might yield more porous films than nanocrystalline cellulose films.

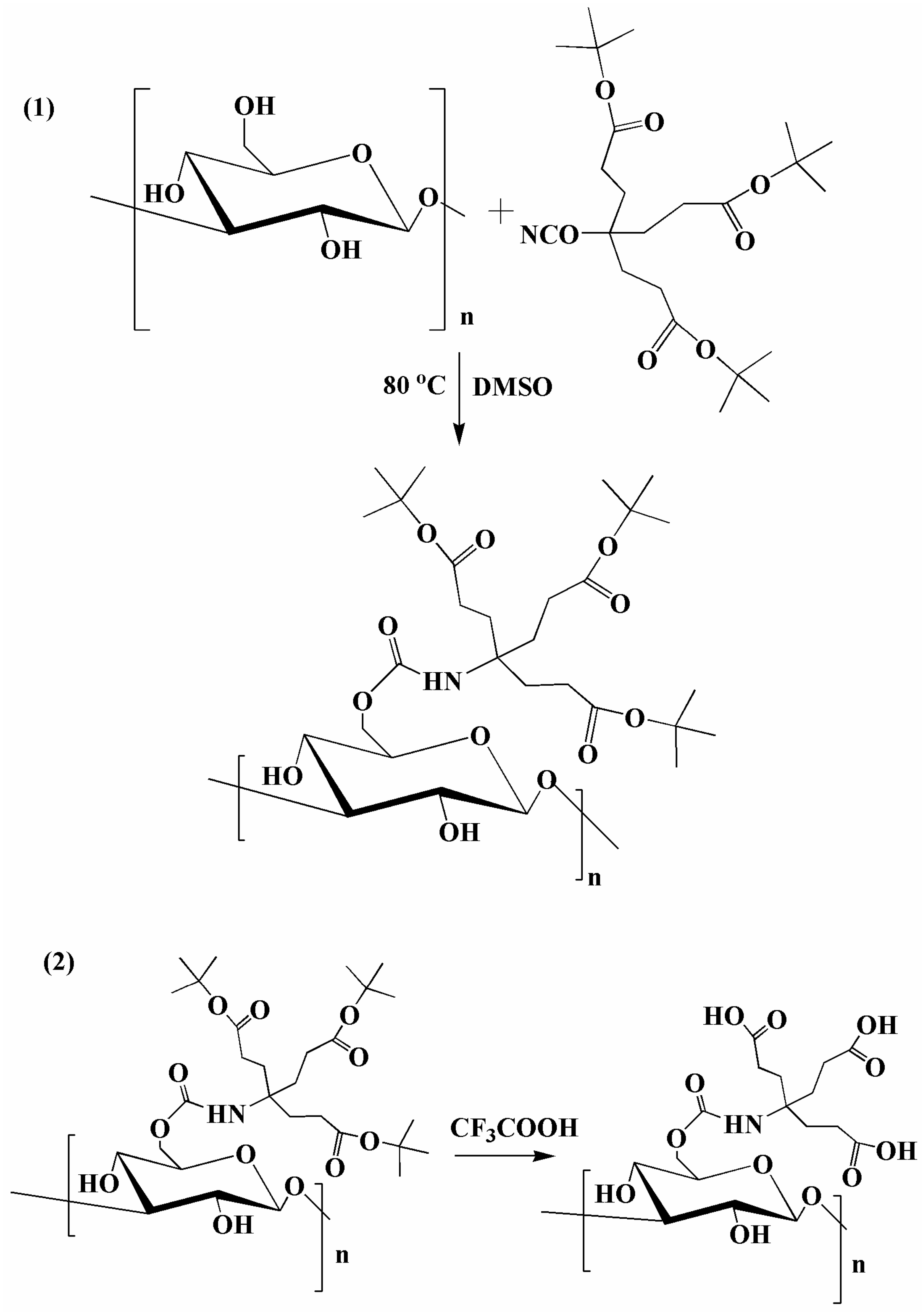

Figure 7.3. Synthetic route for (1) curdlan triester and (2) hydrolysis to a triacid.

7.2.4 Investigation of Polyelectrolyte Adsorption onto Cellulose Surfaces

2-Hydroxypropyltrimethylammonium xylan (HPMAX) was used as a polyelectrolyte to improve the biocompatibility of cellulose surfaces with thermoplastic polymers.[12,13] As one important hemicellulose, modified xylan can be employed to study the interactions of anionic/cationic hemicellulose with cellulose fibers.[14] Adsorption of HPMAX with DS ~ 10% from a 150 $mg \bullet L^{-1}$ aqueous solution onto regenerated cellulose (RC) surfaces yielded a frequency decrease of ($\Delta f/n$) -26 Hz for the 7th overtone. and a dissipation change ~ 4.5×10^{-6} for the 7th overtone (see Figure 7.4). This indicated that HPMAX adsorbed onto RC surfaces and formed aggregates. On the other hand, adsorption of HPMAX onto NC surfaces showed much greater frequency decreases, ($\Delta f/n$) = -144 Hz for the 7th overtone and dissipation increases $\Delta D = 21\times10^{-6}$. This significant adsorption implied thicker HPMAX layers formed on NC surfaces or HPMAX penetrated into the porous NC films. *In situ* AFM studies confirmed this conclusion where spherical aggregates were observed over NC substrates in Figure 7.5. In the future, HPMAX with DS ~ 6, 14 , 19 , and 34% could be used to study their interactions with cellulose surfaces. Some preliminary results showed that maximal adsorption happened at an intermediate DS value whereas charged groups in highly substituted xylan chains favored uniform coverage of the underlying substrates.[15] This provides the possibility of layer-by-layer self-assembly of polyelectrolytes films onto NC.

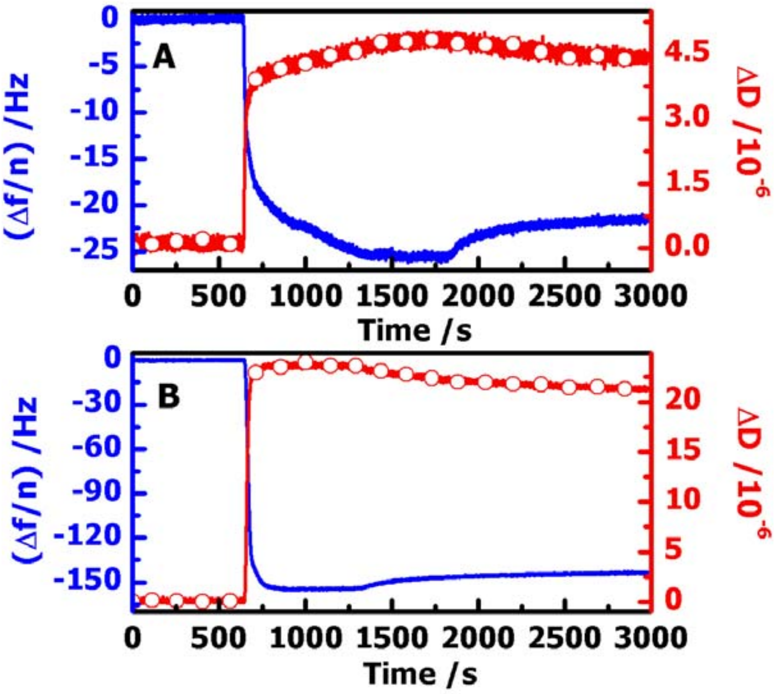

Figure 7.4. (Δf/n) (blue line) and ΔD (red line with circles) vs. time for HPMAX with DS ~ 10% (150 mg•L^{-1}) adsorption onto (A) RC and (B) NC surfaces.

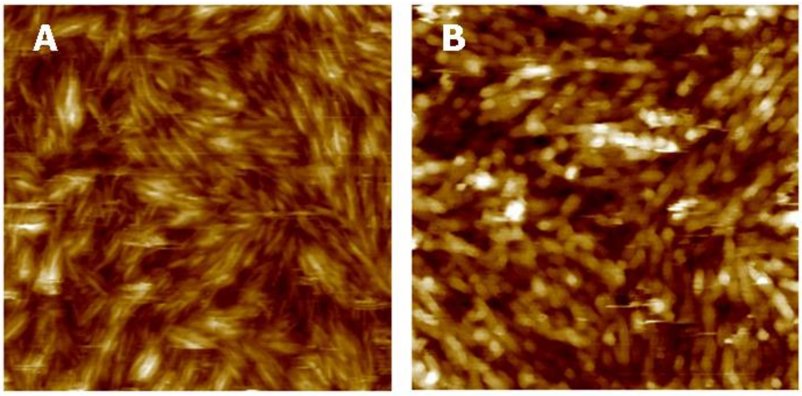

Figure 7.5. Height images of the solid/liquid interface for NC (A) prior to adsorption (B) after the adsorption of HPMAX with DS ~ 10% from a bulk solution (150 mg•L^{-1}). The AFM images are 2 × 2 μm^2 with z scales of 0 to 40 nm.

7.3 References:

(1) Dupuy, A. D.; Engelman, D. M. *Proc. Natl. Acad. Sci. U. S. A.* **2008**, *105*, 2848–2852.

(2) Yennawar, N. H.; Li, L.; Dudzinski, D. M.; Tabuchi, A. ; Cosgrove, D. J. *Proc. Natl. Acad. Sci. U. S. A.* **2006**, *103*, 14664-14671.

(3) Schramm, M.; Hestrin, S. *J. Gen. Microbiol.* **1954**, *11*, 123-129.

(4) Gradwell, S. E.; Renneckar, S.; Esker, A. R.; Heinze, T.; Gatenholm, P.; Vaca-Garcia, C.; Glasser, W. *C. R. Biol.* **2004**, *327*, 945-953.

(5) Kaya, A.; Du, X.; Liu, Z.; Lu, J. W.; Morris, J. R.; Glasser, W. G.; Heinze, T.; Esker, A. R. *Biomacromolecules* **2009,** *10*, 2451-2459.

(6) Liu, Z. "Studies of biomacromolecule adsorption and activity at solid surfaces by surface plasmon resonance and quartz crystal microbalance with dissipation monitoring" Dissertation, Virginia Polytechnic Institute and State University, Blacksburg, VA, 2010.

(7) Zhang, L.; Wang, C.; Cui, S.; Wang, Z.; Zhang, X. *Nano Letters* **2003**, *3*, 1119–1124.

(8) Sugandhi, E. W.; Macri, R. V.; Williams, A. A.; Kite, B. L.; Slebodnick, C.; Falkinham, J. O., III; Esker, A. R.; Gandour, R. D. *J. Med. Chem.* **2007**, *50*, 1645-1650.

(9) Williams, A. A.; Day, B. S.; Kite, B. L.; McPherson, M. K.; Slebodnick, C.; Morris, J. R.; Gandour, R. D. *Chem. Commun.* **2005**, *40*, 5053-5055.

(10) Williams, A. A.; Sugandhi, E. W.; Macri, R. V.; Falkinham, J. O., III; Gandour, R. D. J. *Antimicrob. Chemother.* **2007**, *59*, 451-458.

(11) Jin, Y.; Zhang, H.; Yin, Y.; Nishinari K. *Carbohydrate Research* **2006**, *341*, 90-99.

(12) Mohanty, A. K.; Misra, M.; Drzal, L. T. *Composite Interfaces* **2001**, *8*, 313-343.

(13) Samir, M. A. S. A.; Alloin, F.; Dufresne, A. *Biomacromolecules* **2005**, *6*, 612-626.

(14) Ebringerová, A.; Heinze, T. *Macromolecular Rapid Communications* **2000**, *21*, 542-556.

(15) Kaya, A. "Studies of polysaccharide adsorption onto model cellulose surfaces and self-assembled monolayers by surface plasmon resonance spectroscopy" Dissertation, Virginia Polytechnic Institute and State University, Blacksburg, VA, 2009.